3D mechanical and thermal analysis of an Aluminium piston for a high-speed Diesel laboratory engine

Master thesis in Energy Technology
Thermal Engines

Steinar Haugland

University of Bergen
Geophysical Institute

Western Norway University of Applied Sciences
Department of Mechanical and Marine Engineering

Bergen, 01.06.18

3D mechanical and thermal analysis of an Aluminium piston for a high-speed Diesel laboratory engine

Steinar Haugland

University of Bergen (UiB)
Faculty of Mathematics and Natural Sciences
Geophysical Institute
Postboks 7803
5020 Bergen, Norway

In cooperation with:
Western Norway University of Applied Sciences (HVL)
Faculty of Engineering and Science
Department of Mechanical and Marine Engineering
Postboks 7030
5020 Bergen, Norway

Norwegian title:	3D mekanisk og termisk analyse av et Aluminium-stempel til en hurtigløpende Diesel laboratoriemotor
Author, student number:	Steinar Haugland, 200553
Study programme:	Energy technology, Thermal engines
Date:	01.06.18
Main supervisor (HVL/UIB):	Richard J. Grant
Co-supervisor (HVL):	Lars Magne Nerheim
Client:	HVL

Preface

The master's programme in Energy Technology is a co-operation between the Western Norway University of Applied Sciences (HVL) and the University of Bergen (UiB). The specialization for this work is Thermal Engines.

I would like to thank my supervisor, Prof. Richard J. Grant for his guidance from start to finish and his advice in regards to the finite element method, and my co-supervisor Lars Magne Nerheim for his valuable input about the engine, and earlier works on piston strength analysis.

I would also like to thank Harald Moen for his help with providing experimental data from the engine, and the necessary instruments for doing measurements of the piston.

I would also like to thank everyone at room D425. Their friendship, moral support and productive discussions was a great help and source of motivation while writing this masters thesis.

Finally I want to thank my family and friends, for supporting and motivating me during my time as a student.

Abstract

A cast aluminium piston of a single cylinder Petter Diesel engine is modelled using the finite element method. The engine is intended to be supercharged, which will increase the thermal loading on the piston, and so the purpose of this work is to investigate the piston behaviour and strength when subjected to the current level of thermomechanical load. The dimensions of the piston and piston pin is measured, and the materials and boundary conditions are measured, calculated or assumed.

Areas of particular interest were the combustion bowl rim and the piston pin boss. The latter was modelled using a contact interaction between the pin and boss, in order to accurately represent its behaviour.

The final model is used to investigate the behaviour of the piston, locate the most critically stressed areas and the cyclical stress variations which may lead to fatigue. Local fatigue strength of the material is compared with local stress variations, and it is found that the piston is not exceeding its fatigue strength at any point and its expected lifetime should be quite high for the current loading of the engine.

Sammendrag

Et støpt aluminiumsstempel til en en-sylindret Petter Diesel motor er modellert ved bruk av elementmetoden. Det er planlagt at motoren skal superlades, noe som vil øke den termiske belastningen på stempelet. Formålet med dette arbeidet er å undersøke stempelets oppførsel og styrke under den nåværende termomekaniske belastningen. Dimensjonene på stempelet er målt, og materialer og grensebetingelser er målt, beregnet eller antatt.

Spesielt interessante områder er kanten på forbrenningsskålen, og navet til krysspinnen. Sistenevnte ble modellert ved bruk at en kontakt-interaksjon mellom navet og krysspinnen, for å få en nøyaktig fremstilling av oppførselen til navet.

Den endelige modellen er brukt for å undersøke oppførselen til stempelet, finne de mest utsatte områdene, og de sykliske stressendringene som kan føre til utmatting. Den lokale utmattingsfastheten til materialet er sammenlignet med de lokale stressendringene, og det er funnet ut at stempelet ikke overskrider utmattingsfastheten sin på noe punkt, noe som antyder en relativt høy levetid for stempelet under den nåværende belastningen.

Contents

1 Introduction

1.1 Background

The piston is often referred to as the heart of the reciprocating combustion engine. It is subjected to both thermal and mechanical loading, and plays a central role in converting thermal energy from the combustion into mechanical energy and transferring it to the crankshaft. Due to the high compression ratios, compared with other engine types, Diesel engines in particular subject the piston to very high stress levels.

The Thermal Machines Laboratory at HVL is equipped with a Petter Diesel lab engine in the PH range to be used for educational purposes. The Petter Diesel PH range consist of the air-cooled engines PH1 and PH2, and the water-cooled models PH1W and PH2W. Known to be robust and simple in design, the PH range of engines can be trusted to operate for very long periods of time. [1]

The engine at the HVL Thermal Machines Laboratory is of the type PH1W, and was built around 1960. It is a four-stroke, water-cooled, naturally aspirated (NA), single-cylinder diesel engine producing 6.4 kW of power when running at 2000 rpm. Because it was built to run on lower quality fuels than what is available today, it is very robust and suitable for experiments. Recently it was modified with a common rail (CR) injection system, and there are plans supercharge the engine in the future, which would further increase the loading on the engine.[2] In order to proceed safely, it is necessary to know how the piston is handling the current thermal and mechanical loading.

Historically component strength has been investigated using measurements, but it is now commonplace to use numerical methods, in particular the finite element method (FEM). The idea behind FEM is to divide the body into a finite set of elements connected by nodes, apply loads and boundary conditions, and solve the equations for the resulting system to obtain approximations for quantities of interest. FEM may be used for problems involving, but not limited to, stress and heat transfer. Normally the accuracy increases with the number of nodes used. [3]

1.2 Aim

To investigate the effects of thermal and mechanical loading of an aluminium Diesel engine piston using the finite element method. The analysis will be conducted based on the assumption of a steady working state of the engine.

1.3 Objectives

- Conduct a literature search for relevant and related supporting knowledge to become familiar with the topic of this research and to assess the current knowledge in this field.

- Become familiar with the finite element software package ABAQUS along with the modelling techniques required to build a representative model of the part.
- Acquire realistic boundary conditions, dimensions and material properties to be used as input for the model, and explain the validity and accuracy of these quantities.
- Produce a FEM model of the Petter Diesel engine piston and pin, and perform a convergence study and verification test in order to confirm that the model is representative of the real system.
- Use the model to investigate the behaviour of the piston, find the critically stressed areas and conduct a fatigue analysis for these areas.

1.4 Novelty

While using finite element analysis to verify the strength of a piston has been done numerous times before, this work attempts to give a description of the overall behaviour of the piston, and to describe the results in greater depth.

In particular the stress distribution in the pin boss is looked into, including the differences between thermal loading and combined thermal and mechanical loading. The literature on this seem to be quite sparse and almost no FEM analysis has been done to look at this important area in a great level of detail.

2 Supporting literature

2.1 The diesel engine piston system

The diesel engine piston interacts directly with multiple other components in the engine. In order to get a more complete understanding of the piston, it is important to be familiar with the full piston assembly.

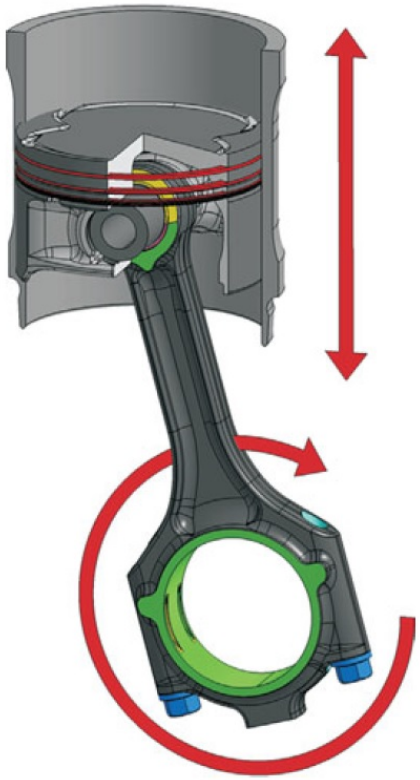

Figure 1: The engine piston assembly.[4]

As shown in Figure 1, the piston is interacting with the cylinder liner, the piston rings and the piston pin. The piston pin connects the connecting rod to the piston. All these components are introduced and explained in some detail in this chapter.

2.1.1 Piston

The piston plays an important role in any reciprocating engine. It converts the thermal energy from the fuel into mechanical energy and transfers it to the crankshaft. Together with the piston rings it must seal the combustion chamber against the passage of gas and the inflow of lubrication oil, and it needs to achieve all these goals under a varied set of operating conditions.

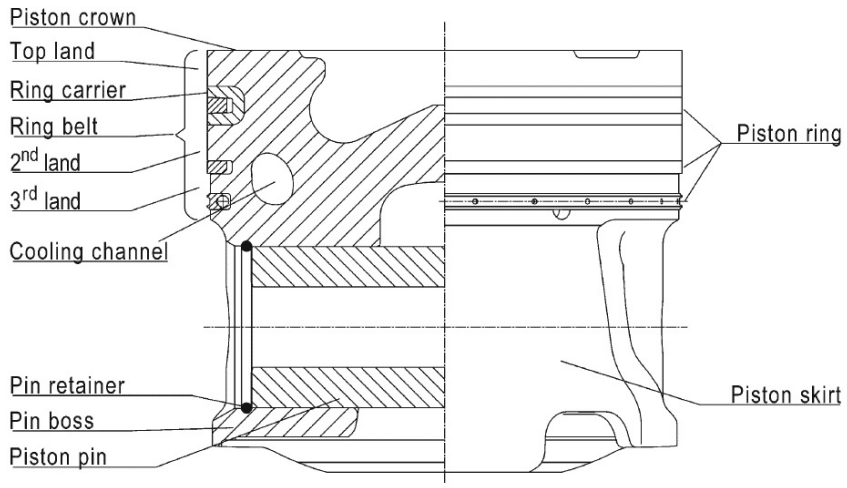

Figure 2: Example of a diesel engine piston.[5]

A typical piston is shown in Figure 2. The top area of the piston is called the piston crown. For a diesel engine piston, the combustion bowl is typically located in the piston crown, and it is often the most thermally stressed part of the piston. The shape of the combustion bowl is used to control the flow pattern of the injected fuel in order to increase the efficiency of the combustion. The shape may vary depending on the configuration of the fuel injector and air/exhaust valves.

The ring belt surrounds the top part of the piston and contains grooves for the piston rings. The parts of the ring belt between two ring grooves are called lands. The top of the piston crown is called the top land, followed by the top piston ring groove, and then followed by the 2^{nd} land, etc. Sometimes a new material, such as cast iron, is inserted around the piston groove (usually only the top piston groove) in order to provide reinforcement.

The lower part of the piston is called the piston skirt, and its role is to guide the piston through the cylinder. The skirt needs to bear the stresses between the piston and cylinder walls, and it also needs to elastically adapt to the deformations of the cylinder. In some pistons the skirt surface is made a significantly thinner in order to decrease the mass of the piston.

The piston pin boss contains the piston pin (also known as a gudgeon pin or wrist pin), which connects the connecting rod to the piston. There are two options for connecting the piston pin in the boss. Either a shrink fit (used to be common) or a floating design where the pin may be inserted at room temperature (most common today). This is where the piston force is transmitted to the connecting rod, and is one of the highly stressed zones of the piston.[6, 7, 5]

2.1.2 Piston pin

The piston pin is the connection between the piston and the connecting rod. The piston pin and pin boss is usually the starting point for calculating piston strength, particularly for aluminium pistons. Under load, ovalisation may occur, which changes the stress distribution between the pin and the pin boss.[8]

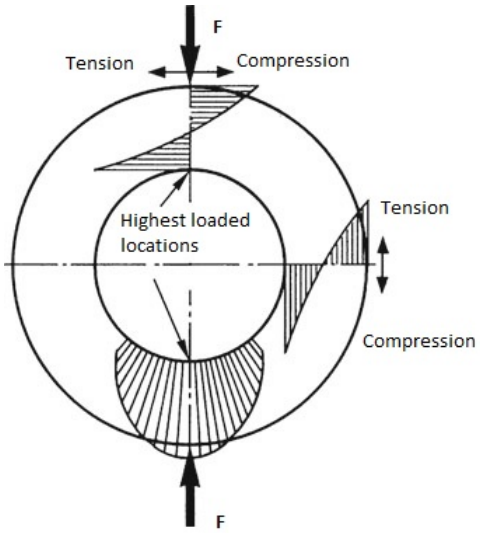

Figure 3: Stress distribution in an ovalised pin.[4]

The piston pin needs to be as light and stiff as possible to reduce ovalisation, bending and shearing. A typical stress distribution for an ovalised pin is shown in Figure 3. Because of the small relative motion of the piston pin, lubrication conditions in the pin boss are poor. In order to improve the lubrication properties and increase the wear resistance, piston pins are usually made of case hardened or nitrated steel. [4]

2.1.3 Cylinder

The cylinder houses the piston and the piston rings. Because of the reciprocating motion of the piston, good lubricity and wear resistance are important. For low cost high-speed engines, the cylinders may be machined directly in the cylinder block ("parent-bore"); however, most engines use cylinder-liners that are fitted into the cylinder block. This is advantageous because the liners may be made of different materials than the cylinder block, and may be optimised to achieve longer lifetimes.

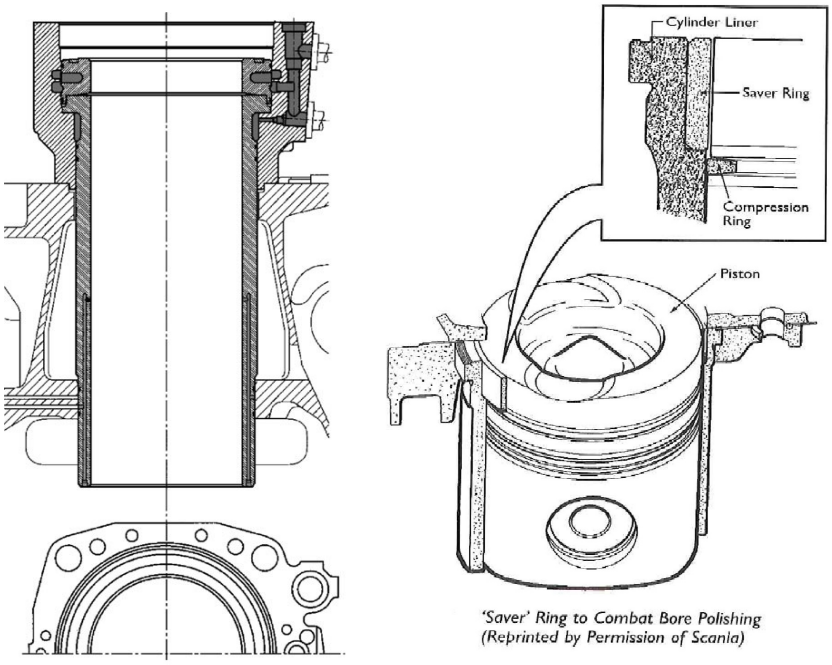

Figure 4: Cylinder liners.[6, 9]

Cylinder liners (illustrated in Figure 4) are usually made from some type of grey cast iron, due to the lubricating properties of graphite. It has been shown that A-type graphite has the best properties for scuff resistance and machinability. In order to improve the scuff resistance, the surface finish is important. Cylinder liners are honed with a cross-hatched pattern in order to get rid of surface peaks and achieve the *plateau condition*, i.e plateaus and valleys, but no peaks.

Cylinder liners are often divided into two categories: "wet liners" and "dry liners". The wet liners are in contact with the coolant, and thus plays an important role for cooling. Dry liners are not in contact with the coolant. Typically wet liners are used for large-bore engines, and dry liners for bore sizes below 150 mm.

One problem occurring in cylinder liners today is bore polish. As the engine runs, carbon deposits may build up on the top *land* of the piston. Eventually this will rub against the cylinder and remove the honing pattern, usually at the non-thrust side. As a result, the piston rings will have problems controlling the oil in this region (with their function as a seal being compromised) and the overall oil consumption will increase. Sometimes a steel or cast iron ring is mounted at the top of the bore, protecting it from polish. This is shown to the right in Figure 4. Another typical solution is the "Laystall-process" where ceramic particles are pressed into the bore surface, to create a resistant layer near the surface.[10]

2.1.4 Piston rings

The piston rings fit into the ring grooves on the piston, and perform three important duties; sealing, cooling and oil management. Piston rings are typically made of cast iron due to its high resistance to wear; but newer piston rings may sometimes be made out of steel. In order to further increase resistance to wear, piston rings are often coated. Electroplated chromium is the most common and widely used form of coating. Scuffing (local welding/adhesive wear) is one of the main problems in piston ring design. Scuffing is mainly influenced by factors that influence the state of the oil film, e.g. temperature.[10]

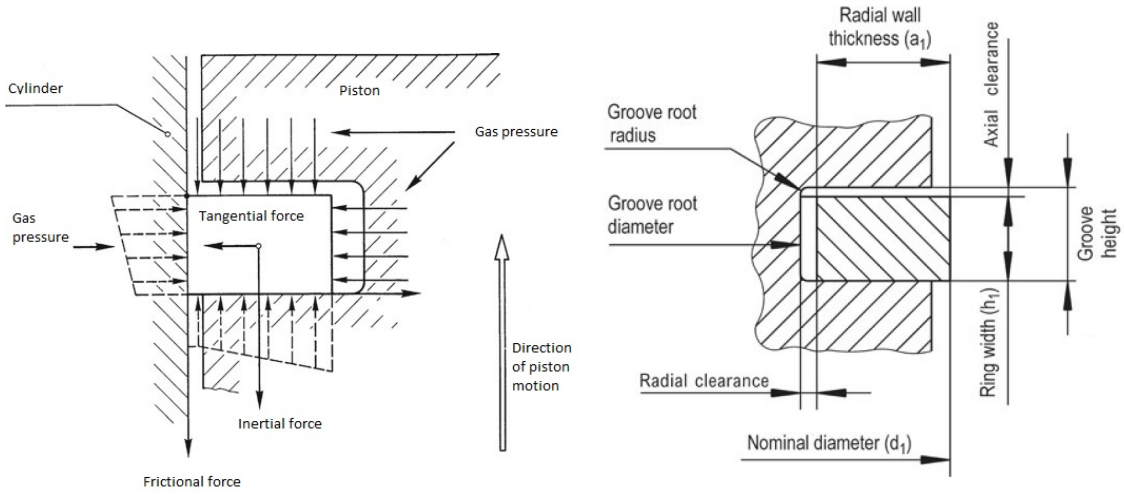

Figure 5: Forces and naming conventions for rectangular piston rings. [6, 4]

- Sealing. As shown in Figure 5, the piston rings are held in place by various forces to form a seal between the piston and the cylinder wall. The piston rings are usually divided into compression rings and oil control rings. The main role of the compression ring is to seal the combustion chamber at all times, while the oil control rings specialise in oil management. Leakage of hot combustion gases is known as 'blow-by' and is usually a bigger concern in high-speed engines. [7, 10]
- Cooling. The piston rings also serve as heat conductors for heat to be transferred from the piston to the cylinder walls. For pistons without a cooling gallery most of the heat transfer happens through the piston rings and the associated ring *land* surfaces.[5]
- Oil management. As the crankshaft turns, it splashes oil towards the cylinder walls, lubricating them. In order to control the amount of oil on the cylinder walls, and to prevent oil from getting into the combustion chamber, the piston rings scrape away the excess oil. This is mainly the job of the oil control ring.

2.1.5 Connecting rod

The role of the connecting rod is to change the axial force from the piston into rotational force for the crankshaft. The connecting rod is typically made of high-grade steel.

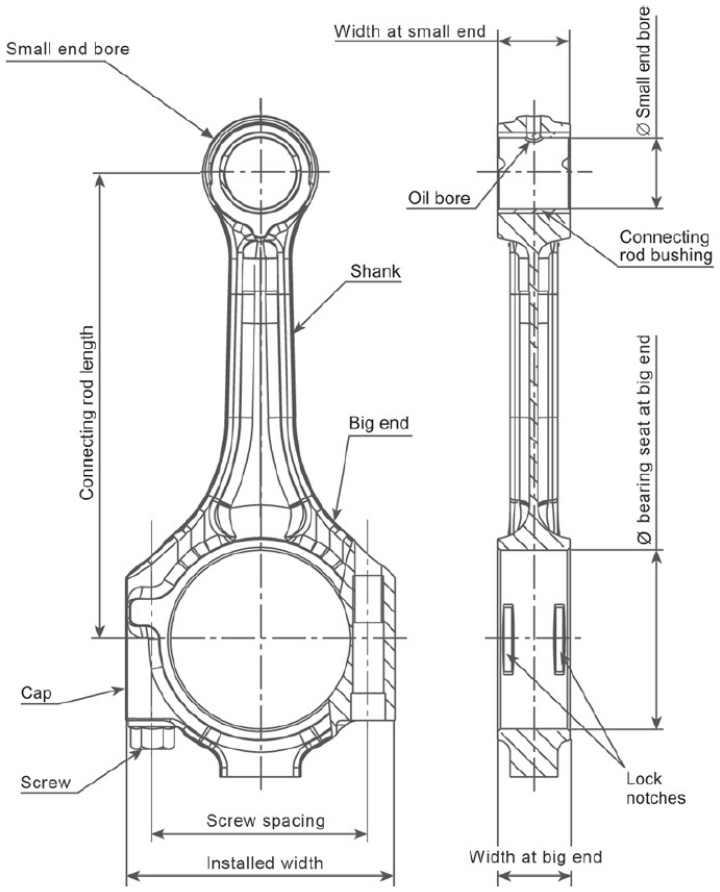

Figure 6: Connecting rod with terminology and major dimensions.[4]

As shown in Figure 6, the connecting rod mainly consists of the small end, the big end and the shank. The big end bore is designed to come apart, while the small end bore is always closed.

The weight of a connecting rod contributes to both the oscillating forces and the rotating forces in the engine. For this reason connecting rods are typically weighed horizontally on two scales, with the centres of the big and small end bores on each scale. This determines the oscillating mass and the rotating mass of the connecting rod.

2.1.6 Piston lubrication

A useful rule-of-thumb is that two-thirds of friction in an engine occurs in the piston and rings, and two-thirds of this friction is due to the piston rings. Frictional losses increase with engine speed and becomes more significant at part loads. In order to understand the frictional losses in an engine, the behaviour of the oil films between the working surfaces must be understood.

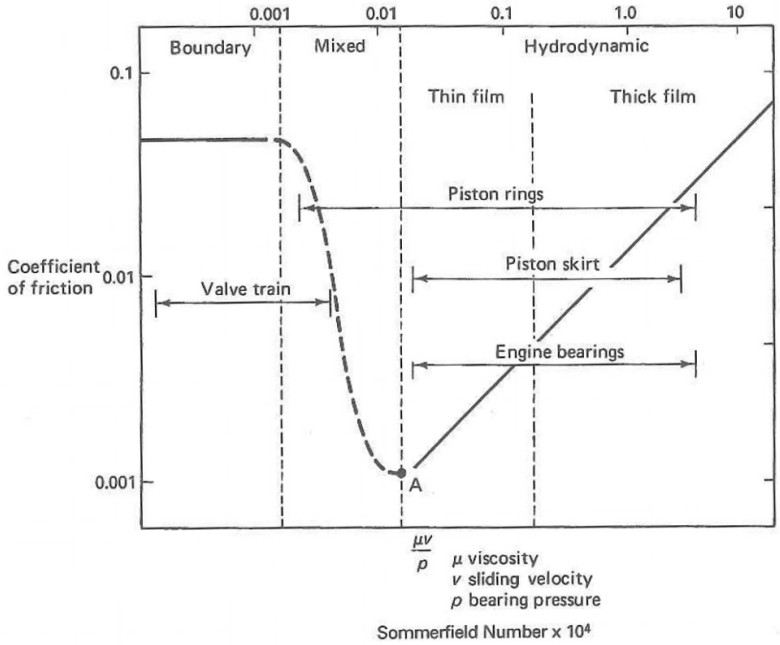

Figure 7: Engine lubrication regimes on the Stribeck diagram.[7]

Figure 7 shows the coefficient of friction plotted as a function of the Sommerfield number, creating a Stribeck diagram. Some typical lubrication regimes for a few engine parts is illustrated. The three regimes are boundary lubrication, mixed lubrication and hydrodynamic lubrication.

Boundary lubrication occurs when the surfaces are in contact, with small gaps filled with lubrication fluid trapped between them due to the roughness of the surfaces.
As the viscosity or sliding velocity increases and the bearing pressure is reduced, the surfaces begin to move out of contact, being separated by lubrication oil. This is called the mixed lubrication regime.
Eventually a full film of lubrication oil separates the two surfaces to a point where there is no metal-to-metal contact and the friction is significantly reduced. This is called the hydrodynamic lubrication regime, and is often further divided into a thin film and thick film regime.[7]

Engine parts are often subjected to varying pressure, sliding velocity and temperature (which affects viscosity). As a result, the various engine parts often span a wide range in the Stribeck diagram. Pistons and piston rings have large variations in pressure and sliding velocity because of the reciprocating motion, and the pressure differences for each of the strokes.

2.2 Finite element analysis and Abaqus

The finite element method is a common way of modelling the behaviour of solids. Abaqus is a program used for finite element simulations.

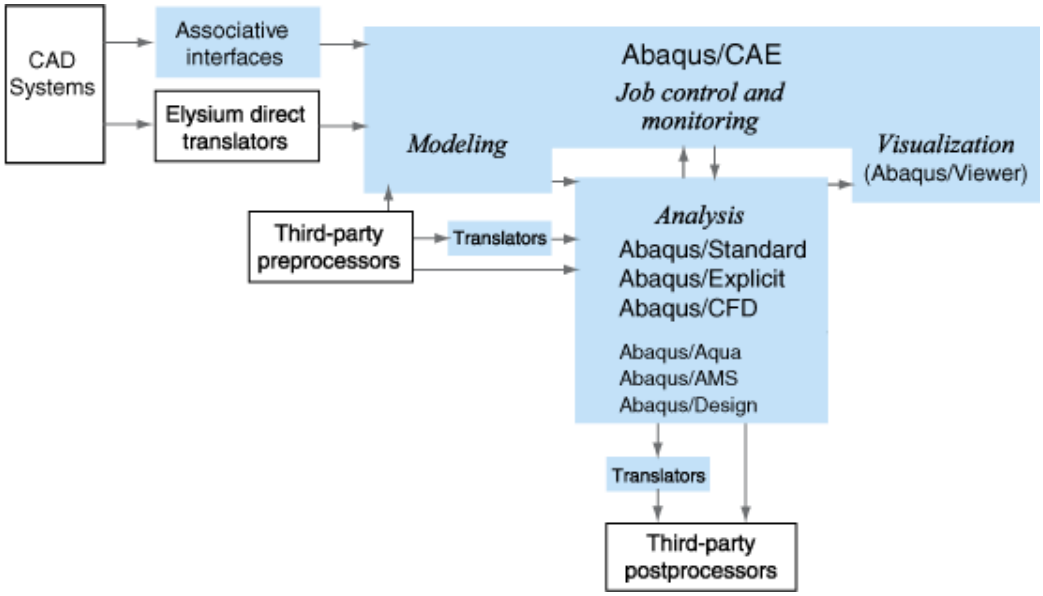

Figure 8: Overview of Abaqus products.[11]

Figure 8 shows the relationship between the various Abaqus products. The Complete Abaqus Environment, or Abaqus/CAE is a graphical environment used to generate models (pre-processing), mesh them and apply boundary conditions. Abaqus/CAE is also used to communicate with the analysis-software, and to view the results returned from the analysis job (post-processing).

The Abaqus/standard 'solver' is a general-purpose product for solving a wide range of linear and non-linear problems using the finite element method. Abaqus/explicit is more suited for transient, dynamic events, and Abaqus/CFD is a Computational Fluid Dynamics product.[11]

2.2.1 Element types

Abaqus offers a wide variety of elements, ranging from 2D to 3D, solid elements, shell elements and analytical surfaces. Appropriate elements must be chosen appropriately in order to accurately model the behaviour of the system.

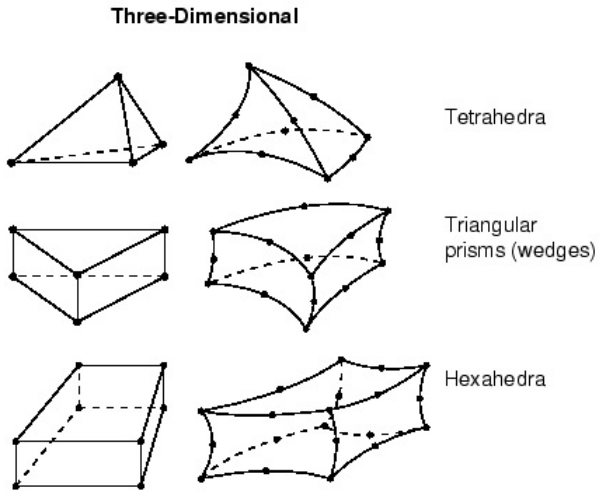

Figure 9: The various three-dimensional element types in Abaqus.[11]

Figure 9 shows the different kinds of 3D elements that Abaqus uses. They are grouped by how many faces they have. There is the four-sided tetrahedral elements, the five-sided wedge elements, and the six-sided hexahedral elements. The elements are made up of a set of nodes which are mathematically connected and shown by lines.

The element types may be further divided into linear and quadratic elements depending on how the nodes are configured, i.e how they are formulated. The linear elements (to the left on Figure 9) only have one node at each corner, resulting in the edges being linear.

The quadratic elements (to the right on Figure 9) have an additional node at the mid-point between two corners, making it possible to have edges corresponding to quadratic functions connecting the corners. In theory switching from linear to quadratic elements makes it easier to model rounded shapes, but at a cost of increased computation time.[11]

2.2.2 Contact modelling in Abaqus

Abaqus offers three algorithms for contact modelling: general contact, contact pairs and contact elements. Contact pairs tend to produce more robust results, while general contact is more convenient to use. Contact elements are used for special cases.

A contact pair consists of a master and a slave, and the surface being deformed must be chosen to be the slave surface. Once the surfaces have been chosen, the contact properties between them are specified.

2.3 Thermomechanical loading

A piston for a diesel engine is subjected to both thermal and mechanical loading.

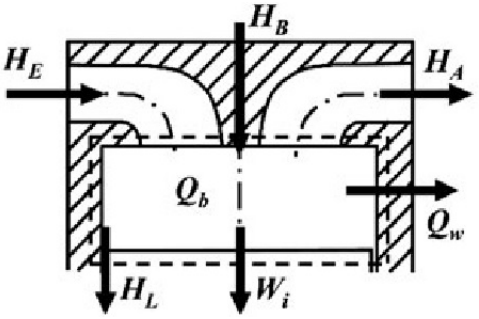

H_E	Intake air enthalpy
H_B	Fuel enthalpy
H_A	Exhaust gas enthalpy
H_L	Leakage enthalpy
Q_b	Released fuel energy
Q_w	Wall heat loss
W_i	Internal work

Figure 10: Energy balance for a combustion chamber.[6]

Figure 10 shows the energy balance for the combustion chamber of a diesel engine. Air and fuel are transported into the combustion chamber, and a chemical reaction occurs to release the fuel energy as heat. Some of this energy are converted into mechanical energy to move the piston, while a portion is lost due to leakage past the piston rings ("blow-by") and heat transfer into the surrounding walls. The rest of the energy is transported out as exhaust gas. The energy balance is given by:

$$H_E + H_B + H_A + H_L + Q_b + Q_w + W_i = 0 \tag{1}$$

For a diesel engine piston, the mechanical load originates from the internal work W_i, while the thermal loading originates from the wall heat loss Q_w. Mechanical and thermal loading will be discussed in greater depth in subsequent chapters of this thesis.

2.3.1 Thermomechanical analysis

When both thermal and mechanical loading is present in a system, their combined effects must be taken into account. This is referred to as thermomechanical analysis. Thermomechanical analysis can be done either experimentally or by the use of simulation software. A common approach is to use the finite element method.

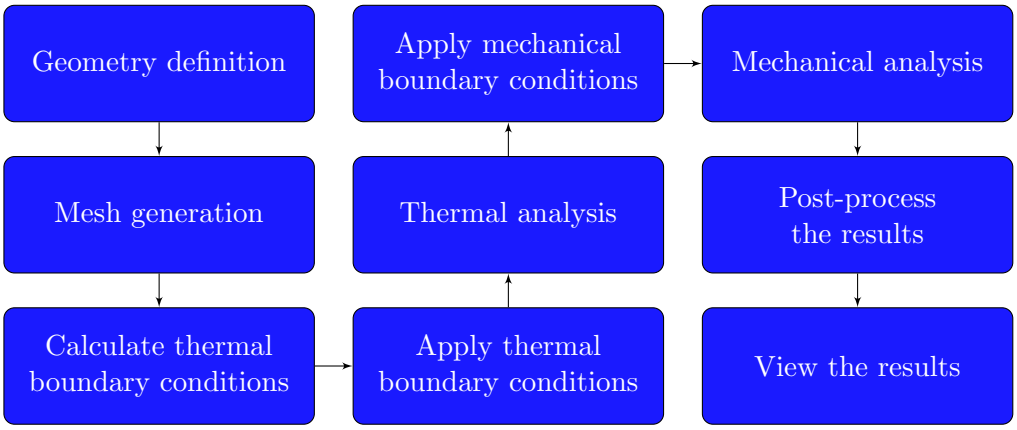

Figure 11: Flow chart of a thermo-mechanical analysis procedure.[10]

A simple breakdown of a typical thermomechanical analysis is shown in a flowchart format in Figure 11. It starts with the definition and meshing of the part, and then the thermal boundary conditions are found and applied. After the thermal analysis is complete, the mechanical boundary conditions and found and added to the simulation. The results are then post-processed and viewed.[10]

P. Reipert and H. Moebus of Kolbenschmidt performed a calculation of the strength of piston pin bosses using thermomechanical finite element analysis. While calculation of piston pin bosses using 3D FEM can be quite accurate, it tends to produce higher stresses in the pin bosses than has been observed experimentally. In their work, the oil film in the boss boundary was included in the analysis, as it was judged to have a cushioning effect on the stress in the boss and was perceived to increase the accuracy of the analysis.

A total of 2070 continuum elements and 3009 nodes were used to model the 320mm AlSi piston. Only a quarter of it was modelled due to symmetry reasons. The thermal and mechanical boundary conditions were calculated and included in the model. The combined thermal and mechanical stress in the piston was given by

$$\sigma_m = \sigma_{ther} + \frac{1}{2}\sigma_{mech} \tag{2}$$

and alternating stress amplitude of

$$\sigma_a = \pm\sigma_{mech} \tag{3}$$

Using the thermal and mechanical analyses, the changing lubrication clearance in the pin boss was found, and the effects of a hydrodynamic lubrication film of varying thickness was included in the analysis. It was shown that the oil was moderating the Hertzian bearing stress by distributing the load over a greater area. The results of the analyses showed that the models without lubrication exceeded the fatigue strength limit, while the lubrication-model did not.[12]

M. Tahar Abbes et al. analysed a DI diesel engine (F8L413 Deutz) piston using a 3D finite element model. Only one quarter of the piston was analysed due to symmetry. A mesh consisting of 92 506 tetrahedral elements was used in the analysis. The thermo-mechanical modelling was done using two methods: a model using separate thermal and mechanical loads, and a global model using coupled thermal and mechanical loads.

They found that the thermomechanical behaviour of the piston was principally influenced by the effect of the thermal loads, the effect of mechanical loads (inertia and pressure) being greatly reduced. The mechanical action mainly influences the piston axis where the mechanical stresses are the most important. The inertial force somewhat reduces the overall mechanical load during transmission. The highest temperatures were obtained on the head of the chamber chamfer of the piston.[13]

2.4 Thermal loading

Thermal loading has always been a crucial element in the development of higher performing diesel engines. Because of the complexity of the engine, the heat transfer in the piston assembly is still not systematically clear to researchers.[14] Thermal analysis of pistons mainly began in the 1940s with the development of the electrical analogy method and the simple analytical method. In the 1960s rheological models were developed, and in the mid 1980s the finite element method was used to perform a numerical simulation of the piston thermal loading.[13]

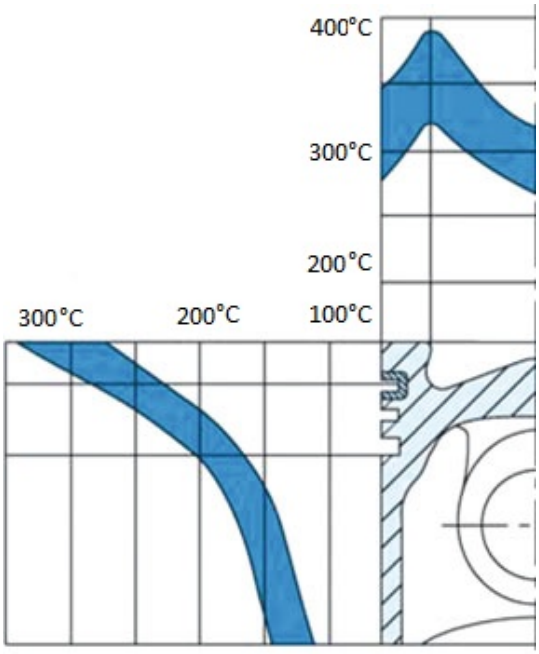

Figure 12: Temperature distribution in diesel engine piston.[6]

As illustrated in Figure 12, a diesel engine piston has a temperature gradient in two directions. It has a vertical temperature distribution, as it is hotter near the top and colder near the bottom of the piston. It also has a horizontal temperature gradient because of the cooling heat transfer between the piston and the cylinder liner wall.

The main effects of thermal loading may be listed as:

- **Thermal expansion.** As a material is heated, it expands. Accounting for thermal expansion is a key problem in piston design. Pistons usually have a greater thermal expansion coefficient than the cylinder, and the asymmetric shape of the piston leads to non-uniform temperature distributions and asymmetrical expansions. Clearances must be chosen carefully, to avoid piston seizure at the highest operating temperatures.[7] In a typical engine with an aluminium piston and a cast iron cylinder, the thermal expansion coefficient of the piston may be 80% greater than that of the cylinder.[15]

- **Thermal stress.** The heat being transferred away from the combustion chamber and through the cylinder walls form a temperature gradient. Since thermal expansion is related to the temperature, a temperature gradient will cause varying levels of expansion to different areas, resulting in internal stresses in the piston. Because the thermal load may be treated as a quasistatic load, the thermal stress is often factored into the mean mechanical stress for simplicity.[6]

- **Material weakening.** A lot of materials tend to lose strength when heated to high temperatures. Aluminium in particular, loses most of its strength when heated. In other words, the local material strength of the piston will vary depending on the temperature in that area.[16]

2.4.1 Fundamental heat transfer concepts

By definition, heat is a form of energy that is transferred from one system to another as a result of a temperature difference. Heat transfer problems are often classified as steady-state or transient. In steady-state there is no change with time, whereas transient problems are time dependent.

$$\dot{Q}_{in} - \dot{Q}_{out} = \frac{dE_{sys}}{dt} \tag{4}$$

Equation 4 is an energy balance for a thermodynamic system. $\dot{Q}_{in}$ is the rate of heat transfer into the system, $\dot{Q}_{out}$ is the rate of heat transfer out of the system and dE_{sys}/dt is the rate of change in the energy contained within the system. For a steady-state problem, dE_{sys}/dt will approach zero and the energy in the system will remain relatively constant. For a transient problem, dE_{sys}/dt will be non-zero and the energy in the system will vary with time. There are three modes of heat transfer: conduction, convection and radiation.

Conduction. Heat conduction is the transfer of energy from energetic particles to adjacent, less energetic particles in a substance as a result of temperature differences. It can happen in solids, liquid and gases. A general description of heat conduction through a plane layer ("a wall") is given by Fourier's law:

$$\dot{Q}_{cond} = -kA\frac{dT}{dx} \tag{5}$$

Here A is the surface area of the wall, k is the thermal conductivity and the term $\frac{dT}{dx}$ refers to temperature difference relative to the thickness of the wall. Because heat moves from a high temperature to a lower temperature, the term dT is always negative if dx is the positive direction, and hence there has to be a negative sign in front of the equation. In general, solids tend to have the highest thermal conductivity, followed by liquids, and gases tend to have the lowest thermal conductivities.

In its non-differential form, Equation 5 may be written as:

$$\dot{Q}_{cond} = kA\frac{T_1 - T_2}{x_1 - x_2} = \frac{T_1 - T_2}{\frac{\Delta x}{kA}} = \frac{\Delta T}{R_{cond}} \tag{6}$$

Where R_{cond} is the thermal resistance of conduction, for a wall it is equal to $\frac{\Delta x}{kA}$. Rewriting the equation in the form of a temperature difference divided by a thermal resistance is quite useful, which will be shown later.

Convection. This mode of heat transfer applies when there is bulk fluid motion in addition to heat conductivity. It can be used to describe the heat transfer between a moving fluid and a still surface (solid, or a quiescent fluid). Because convection involves fluid motion and in some cases phase changes such as boiling, it is an extremely complex form of heat transfer. Despite this, it can be described using a simple formula known as Newton's law of cooling:

$$\dot{Q}_{conv} = hA_s(T_s - T_\infty) \tag{7}$$

Where A_s is the area of the surface that is in contact with the fluid. T_s is the temperature of the surface, and T_∞ is the temperature of the fluid at a distance where it is not affected by the heat transfer between the fluid and surface. The factor h is the convection heat transfer coefficient, often called the "film coefficient" of the surface. The film coefficient is not a property of the fluid by itself, but depends on the surface geometry, fluid motion and velocity, and properties of the fluid.

This equation may also be rewritten as a temperature difference divided by a thermal resistance.

$$\dot{Q}_{conv} = \frac{T_s - T_\infty}{\frac{1}{hA_s}} = \frac{T_s - T_\infty}{R_{conv}} = \frac{\Delta T}{R_{conv}} \tag{8}$$

Radiation. Matter may also give off energy in the form of electromagnetic radiation. All matter whose temperature is above absolute zero emit radiation in the form of thermal radiation. Only this type of radiation is considered in heat transfer problems. The maximal rate of radiation that can be emitted by a surface is described by Stefan-Boltzmann's law:

$$\dot{Q}_{emit,max} = \sigma_{sb} A_s T_s^4 \tag{9}$$

Where A_s is the surface area, T_s is the surface temperature and $\sigma_{sb} = 5.670\text{x}10^{-8}$ W/m^{2}K is the Stefan-Boltzmann constant. Equation 9 describes a surface with maximum emissivity, called a black-body. Realistic surfaces are not blackbodies however, and this is accounted for by introducing the emissivity which lies in the range $0 \leq \epsilon \leq 1$; where a black-body equals 1 by definition.

A surface will also be affected by incoming radiation from its surroundings. The ability of the surface to absorb incoming energy is given by the absorptivity α, which also lies

in the range $0 \leq \alpha \leq 1$ and a black-body has $\alpha = 1$. Kirchhoff's law states that for a given temperature and wavelength $\epsilon = \alpha$. In order to determine the net heat transfer, the radiation from the surroundings must be subtracted from the radiation emitted by the surface. The resulting equation for net heat transfer by radiation for a surface is then given by:

$$\dot{Q}_{rad} = \epsilon \sigma A_s (T_s^4 - T_{surr}^4) \tag{10}$$

Where T_{surr} is the temperature of the surroundings and ϵ is the emissivity of the surface. Equation 10 may be rewritten into the same form as Equation 7:

$$\dot{Q}_{rad} = h_{rad} A_s (T_s - T_{surr}) \tag{11}$$

$$h_{rad} = \epsilon \sigma (T_s + T_{surr})(T_s^2 - T_{surr}^2) \tag{12}$$

Where h_{rad} is the radiation heat transfer coefficient. Using this, Equation 10 may be represented using a thermal resistance:

$$\dot{Q}_{rad} = \frac{T_s - T_{surr}}{\frac{1}{h_{rad} A_s}} = \frac{T_s - T_{surr}}{R_{rad}} = \frac{\Delta T}{R_{rad}} \tag{13}$$

Thermal resistance networks. Because all three modes of heat transfer may be written using the concept of a thermal resistance, a heat transfer problem may be represented as a network of thermal resistances, analogous to electric circuits.

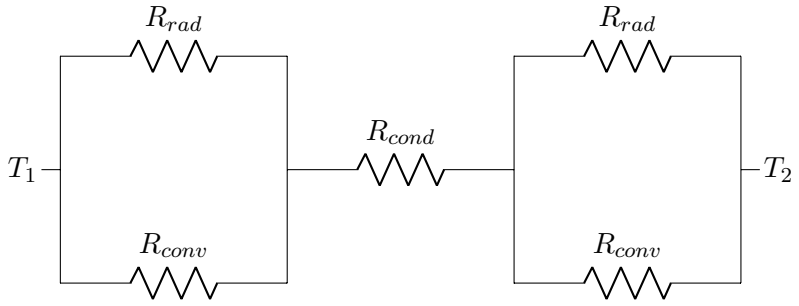

Figure 13: Thermal resistors representing the heat transfer through a wall.

Figure 13 shows how heat transfer through a wall surrounded by fluid can be represented by a thermal circuit, with temperature T_1 and T_2 in this case being both T_{surr} and T_∞ on each side of the wall. In this case the wall is affected by both convective and radiation heat transfer from the fluid on both sides, whereas the heat transfer through the wall itself happens by conduction. The system may be solved by finding a total resistance for the overall heat transfer. The formulae for this follows the electric circuit analogy perfectly.

Series:

$$R_{tot} = \sum_{i=1}^{n} R_i \tag{14}$$

Parallel:

$$\frac{1}{R_{tot}} = \sum_{i=1}^{n} \frac{1}{R_i} \tag{15}$$

Once R_{tot} is known, it may be used to find the total heat transfer in the system. This is often done by introducing the overall heat transfer coefficient U.

$$\dot{Q} = \frac{\Delta T}{R_{tot}} = UA\Delta T \tag{16}$$

$$U = \frac{1}{AR_{tot}} \tag{17}$$

Here, the area A represents the effective area of heat transfer. For a plane surface, it is simply the area for the surface. The temperature difference $\Delta T = T_2 - T_1$ is analogous to voltage. This way a large complex system of heat transfer may be reduced down to a single thermal resistor with just the total temperature difference. Thermal networks are a powerful tool for modelling heat transfer problems.[17]

Thermal contact resistance. When dealing with thermal contact between two solids it is important to remember that every surface has a certain roughness which causes small gaps at the interface, and as a consequence real solids cannot be in "perfect contact". The heat transfer between two real solids is the sum of the heat transfer by contact, and the heat transfer by convection and radiation through the gaps. Thermal contact resistance may be expressed as:

$$R_c = \frac{1}{h_c} = \frac{\Delta T_{interface}}{\dot{Q}/A} \tag{18}$$

Where R_c is the thermal contact resistance, h_c is the thermal contact conductance, $\Delta T_{interface}$, $\dot{Q}$ and A is the temperature difference, heat flow and area of the interface, respectively. Note that R_c is defined for a unit area [m^2K/W] as opposed to R_{cond}, R_{conv} and R_{rad} whose units are [K/W]. In order to obtain the thermal resistance for the entire interface, R_c must be divided by A.

The value of R_c depends on the surface roughness and material properties of the solid and the temperature, pressure and type of fluid trapped within the gaps at the interface. Thermal resistance between two solids may be minimized by using a thermal grease (e.g silicon oil) or a soft material (e.g copper or aluminium) at the interface. Generally speaking, the thermal contact resistance is lowest for soft metals with smooth surfaces at high pressures. It is important to decide if the thermal contact resistance high enough to influence the overall heat transfer, or if it can be neglected.

2.4.2 Heat transfer analysis

A. Torregrosa et al. developed a concise wall temperature model for DI diesel engines. They considered the piston, the cylinder liner and the fire deck (the top of the combustion chamber, containing the fuel injector and the inlet- and exhaust valves) as the system for the model. It was assumed that the piston and the liner have a uniform temperature, and that the inlet and exhaust valves only exchange heat with their seats.

The film coefficient between the combustion gases and the wall was obtained using Woschni's equation (an empirical equatial for calculating the film coefficient for the combustion process of a diesel engine[7]). The model was optimised by reducing the RMS error between the predicted and measured wall temperatures. The model gave good estimates for wall temperature, also for tests not included in the optimisation and tests performed on another engine. The conductance between the cylinder liner and coolant, as well as the conductance between the piston and liner were both constant, while the conductance between the piston and cooling oil was dependent on piston speed.[18]

E. Buyukkaya et al. used 3D FE simulation in order to do a thermal analysis of a ceramic coated diesel engine AlSi piston. Eight noded linear thermal elements were used, and surface elements were defined between the piston rings and the ring grooves. The piston pin was not included. For the analysis, certain assumptions were made: The effect of piston motion on the heat transfer was neglected, the rings were not permitted to twist, and the rings and skirt were fully engulfed in oil where the heat transfer in the oil film was neglected. It was also assumed that the inside ambient temperature could be estimated as the average temperature of the intake, compression, combustion and exhaust temperatures. The study showed that using a ceramic coating may improve maximum surface temperature of an AlSi piston by 48%. Reduction in the cooling load should also be obtainable.[15]

In another article, E. Buyukkaya again used a 3D FE model in order to do a thermal analysis of a functionally graded coating on both AlSi and steel pistons. Funtionally graded coatings are used to reduce the mismatch effect. Functionally graded materials (FGM) are materials whose properties vary along the thickness of the coat. The coating system uses three composite interlayers between the bond and top coat in the FGM coating. Contact elements were used between the piston rings and ring grooves. The same assumptions as in the previously mentioned paper by Buyukkaya were used.

A comparison between uncoated and FGM coated pistons was made. The surface temperature was increased by 28% in the FGM coated AlSi piston and 17% in the FGM coated steel piston. It was concluded that using an FGM coating increases the temperature in the combustion chamber of the engine, and the thermal strength of the base material. The temperature values of a FGM coated piston surface was lower than a traditional surface coating of similar thickness. The reason for this was that because the number of layers increased, the thickness of the top coat was decreased. This resulted in an increase of thermal diffusivity, and thus the heat insulation capability also increased.[19]

2.5 Mechanical loading

2.5.1 Fundamental mechanical concepts

Stress concentration. A machine part is often described using nominal normal and shear stresses σ_{nom} and τ_{nom}; however for changes in geometry, the stress may increase at certain regions. These areas are often referred to as "stress-raisers", and the nominal stresses and maximum local stresses are related using geometric stress-concentration factors (SCFs).

$$\sigma_{max} = K_t \sigma_{nom} \tag{19}$$

$$\tau_{max} = K_{ts} \tau_{nom} \tag{20}$$

where K_t and K_{ts} are the SCFs for normal stress and shear stress, respectively (the subscript t is an abbreviation for theoretical). These take the geometry of part geometry into account, but does not account for how a material will behave under the increased stress. In the case of a ductile material, it will yield locally if the yield strength is exceeded at a given point, but will remain elastic at regions at sufficient distance from this point where the stress is below the yield limit. Brittle materials do not have an elastic range, and will begin to form cracks leading to fast fracture once the stress-raiser exceeds the fracture strength. However, most engineering materials show some ductility.

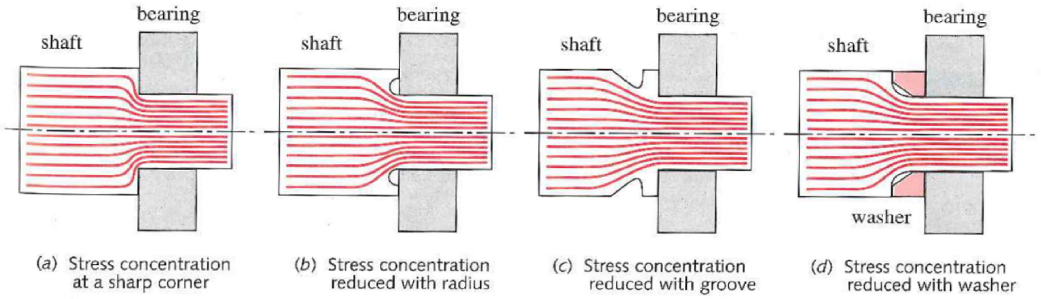

Figure 14: Illustrating stress concentrations using force-flow. [16]

Under dynamic loading, ductile materials behave and fail as if they were brittle. Because of this, SCFs are very important when working on parts that are dynamically loaded. [16]

Force flow. A common way to visualize the effects of stress concentrations is the "force-flow" analogy as shown in Figure 14. Imagining the force-lines as a flow through the material, it can be seen that certain geometric shapes "concentrate" these force-lines, increasing the force in a given area and hence the stress there.

Notch. A generic term used when dealing with stress concentrations is "notch". A notch can be anything that disrupts the force flow through a part. It can be a hole, a groove, a fillet, an abrupt change in cross section, or any disruption of the smooth contours of a part. A notch will create a stress-concentration, which will increase the local stress and maybe even lead to yielding or fracture.[16]

Designing to avoid stress concentrations. Completely avoiding stress-raisers is often impossible due to practical constraints of the part (e.g needing a keyway or piston ring grooves). Even so, trying to avoid stress-raisers whenever possible and knowing where they may show up is important. Some guidelines for avoiding stress concentration when designing a part is listed below.

- Try to avoid large or sudden changes in the cross section of a part.
- Try to avoid sharp corners and make transitions between different surfaces as smooth (large radii) as possible.

An SCF can be assessed through the use of tables or formulae, whereby common geometric forms are represented.[20, 21, 22] As many engineering components are too complex to calculate SCFs accurately, finite element models must be used. Such models can be used in conjunction with SCF formulae or tables to assess potensially problematic geometry. It should be noted that such derivations can contain errors as in many instances their derivation used photoelastic models with high Poissons Ratio.[23]

Saint-Venant's principle. This principle states that elastic stresses and strains sufficiently removed from a loaded region will behave identically for any statically equivalent load. As the distance between the load source increases, the stress will spread more uniformly throughout the material. For instance, a point load and a pressure load may produce the same behaviour, given that they are statically equivalent, the deformation is elastic, and the points of interest is sufficiently removed from the source. In general, this distance should be at least equal to the largest dimension of the loaded cross-section.[24]

2.5.2 Mechanical analysis

Forces in the piston system. The piston is subjected to a force from the gas pressure, and an oscillating force from the reciprocating motion. The resultant piston force is transferred through the piston pin to the connecting rod, and from the connecting rod to the crankshaft as a rotational force.

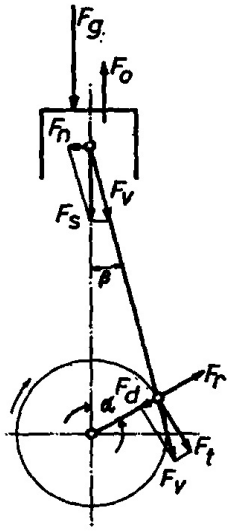

F_g	Gas force
F_o	Oscillating force
F_n	Normal force
F_s	Force on piston
F_V	Crank force
F_r	Rotational force
F_t	Tangential force
F_d	Radial force
α	Crank angle
β	Connecting rod angle

Figure 15: The mechanical forces working on a piston. [25]

Figure 15 shows the forces acting on the piston. Note that the gas force and oscillating force tend to behave in opposite directions. The gas force is dependant on the cylinder pressure and the piston area and may be calculated from:

$$F_g = P(\alpha)\frac{\pi}{4}D^2 \tag{21}$$

Where D is the piston diameter and P is the cylinder pressure plotted against α, the crank angle. The oscillating force may be calculated from:

$$F_o = m_o a(\alpha) = (m_s + m_{vo})R\omega^2(cos(\alpha) + \frac{R}{L}cos(2\alpha)) \tag{22}$$

Here m_o is the oscillating mass, m_s is the mass of the complete piston (pin included) and m_{vo} is the oscillating mass fraction of the connecting rod. R is the crank radius, L is the connecting rod length and ω is the angular velocity of the crankshaft.

The value of m_{vo} may be measured by placing the centres of the small end and the big end of the connecting rod on two separate weights at the same time. The weight at the small end is the oscillating mass fraction and the weight at the big end is the rotating mass fraction. A typical assumption is that the oscillating mass is one third of the total connecting rod mass ($m_{vo} \approx \frac{1}{3}m_v$). [4]

Added together, these form the piston force, which is the force acting from the piston to the piston pin.

$$F_s = F_g + F_o \tag{23}$$

The connecting rod forms an angle β with the piston. With the exception of BDC and TDC (Top- and Bottom-Dead-Centre) this angle will be non-zero and a lateral force called the normal force will be created. This force acts between the piston and the piston wall. The piston skirt must be carefully designed to withstand this force.

$$F_n = F_s tan(\beta) \tag{24}$$

In general, the gas force F_g tends to be the most important, while the oscillating force F_o tends to become increasingly important in high speed engines. The normal force F_n is rather small, but plays an important role in the interplay between the piston and the cylinder wall.

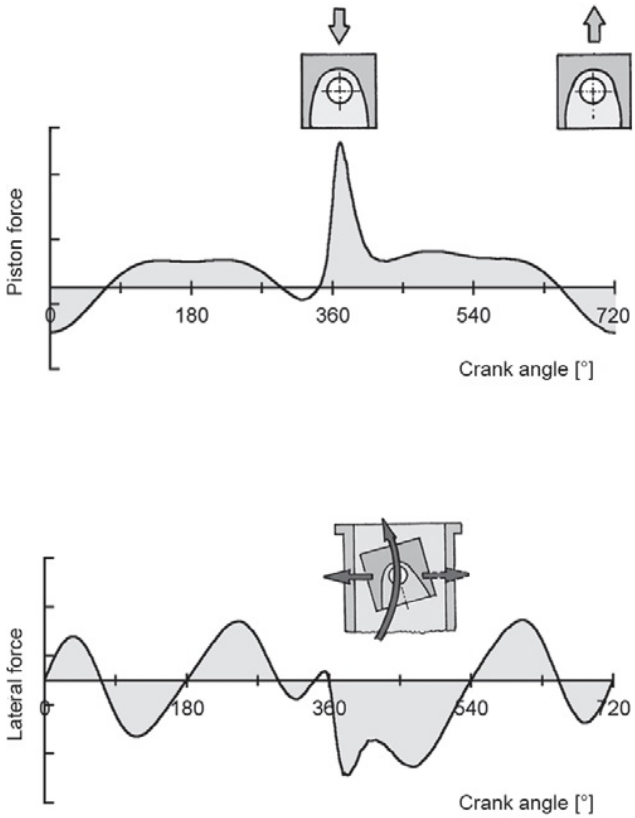

Figure 16: Fs and Fn behaviour[5]

The normal force is asymmetric in nature as shown in Figure 16. The angle β will be positive or negative depending on whether the piston is moving up or down, causing the direction of the normal force to alternate. Because the normal force is dependant on the piston force, if will be much greater during the expansion stroke, when the piston is moving down.

The direction the normal force is pointing during the expansion stroke is referred to as the thrust-side and the opposite side is referred to as the antithrust-side. The behaviour of the piston force mostly depends on the cylinder pressure. [25]

Mechanical behaviour of the piston. For aluminium pistons, the deformation of the system is mostly caused by the rigid piston pin. The piston body tend to have lower stiffness because of its highly temperature-dependant material properties. The deformation around the piston pin generates stresses created by the gas force in addition to temperature stresses. This causes a "saddle-shaped" curve in the piston ring grooves.[5]

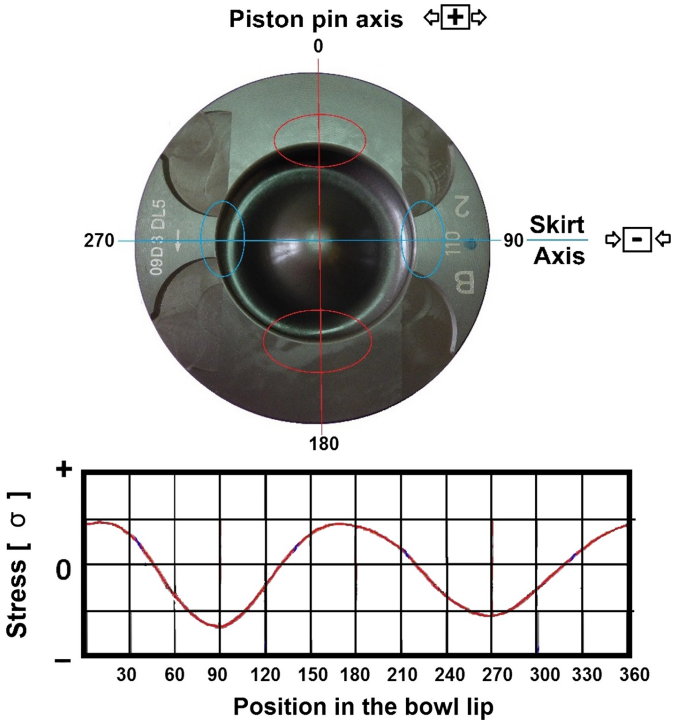

Figure 17: Sketch of the classic stress distribution at the piston surface.[26]

For all pistons, the gas force will cause compressive stresses in the boss and support area, and the transition from the support area to the piston crown. The load limit of the bosses are at risk of being exceeded because of high local stresses and temperatures. Aluminium pistons are particularly vulnerable to this because of their relatively low strength at high temperatures. At the TDC during the power stroke, the inertial force relieves some of the contact load at the piston pin boss.[5]

Figure 17 illustrates a classic stress distribution in a piston, showing that tensile stress occurs on an axis above the piston pin, and compressive stress occurs at an axis perpendicular to the piston pin axis. [26]

Mechanical behaviour of pin-loaded lugs. R.J. Grant and B.C.D. Flipo did a parametric study of the elastic stress distribution in pin-loaded lugs modelled in two and three dimensions and loaded in tension using FEA. Stress distributions for clearance-fit, snug-fit and interference-fit pins were investigated and two and three dimensional effects were compared. An important difference between the two and three dimensional models is the variation of stress throughout the bore, and in particular, the "edge effects" near the ends of the bore.[27]

Mechanical behaviour of pin-loaded tubes. R.J. Grant and J. Smart did a parametric study of the elastic stress distribution in pin-loaded tubes using FEA. Stress distributions for clearance-fit, snug-fit and interference-fit pins in tubes of various geometries were studied. In particular the point of maximum circumferential stress was found, as it is commonly assumed that cracks will initiate from this point, and the maximum circumferential stress value determine whether cracks do initiate.[28]

2.6 Types of wear

Fatigue. This type of damage occurs in three stages; crack initiation, crack propagation and fracture. During the crack initiation phase, high stress concentration in areas with varying stress levels may lead to plastic deformation. The plastic deformation eventually leads to a crack. As the load cycles increase, cracks will continue to grow until the material is weakened enough for a fracture to occur.

Fatigue is often divided into two regimes, high-cycle fatigue (HCF) and low-cycle fatigue (LCF), depending on how many cycles a part is expected to undergo during its lifetime. There is no sharp divide between the regimes.

There are three main models for describing fatigue. The stress-life (S-N) method, the strain-life (ϵ-N) method and linear-elastic fracture mechanics (LEFM). For most rotating machinery, the S-N method is used. Practically all engines work in the HCF regime, and cyclic loads are reasonably predictable and consistent, increasing the accuracy of the S-N method.[16]

The S-N approach seeks to determine the relationship between the maximum loading stress and the fatigue life. It is the most common model for HCF cases, but is the least accurate of the three models, particularly for LCF. It's also the most empirical of the three models and relies heavily on empirical fatigue data.

For some materials, a minimum alternating stress is needed to cause fatigue. This is called the fatigue limit and theoretically, fatigue cannot occur at alternating stresses below this limit. Other materials like aluminium, does not have a fatigue limit. Their behaviour is described by the fatigue strength, which is the alternating stress required to cause failure at a certain number of load cycles. For aluminium alloys, this value is typically $5x10^8$ unless otherwise stated.[16]

Cyclic loading is described using a mean stress component σ_m and the alternating stress component σ_a.

$$\sigma = \sigma_m \pm \sigma_a \tag{25}$$

$$\Delta\sigma = \sigma_{max} - \sigma_{min} \tag{26}$$

$$\sigma_m = \frac{\sigma_{max} + \sigma_{min}}{2} \tag{27}$$

$$\sigma_a = \frac{\sigma_{max} - \sigma_{min}}{2} \tag{28}$$

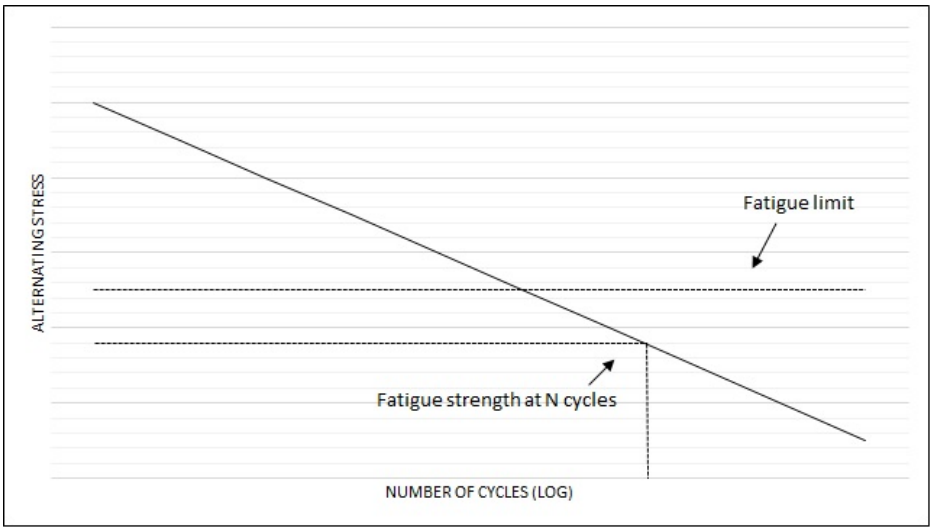

Figure 18: Wöhler diagram illustrating the fatigue strength and the fatigue limit.

Figure 18 shows an SN-curve for an aluminium alloy. If it were a ferrous alloy like steel the curve would form an asymptote towards the fatigue limit of the material, and below this point it would have an infinite fatigue life. However for an aluminium alloy cracks may be formed even at very low levels of stress, and there is no fatigue limit. Instead its fatigue resistance is measured as the stress which will allow it a life of N = 5x10^8 cycles, and this stress is called the fatigue strength.

Most fatigue data is generated from 'reverse bending stress' σ_{bw}, in which case $\sigma_m = 0$, and σ_a alternates between tensile and compressive stresses of the same magnitude. In reality there are often cases where the mean stress $\sigma_m \neq 0$. In these cases it is possible to use one of several failure lines.

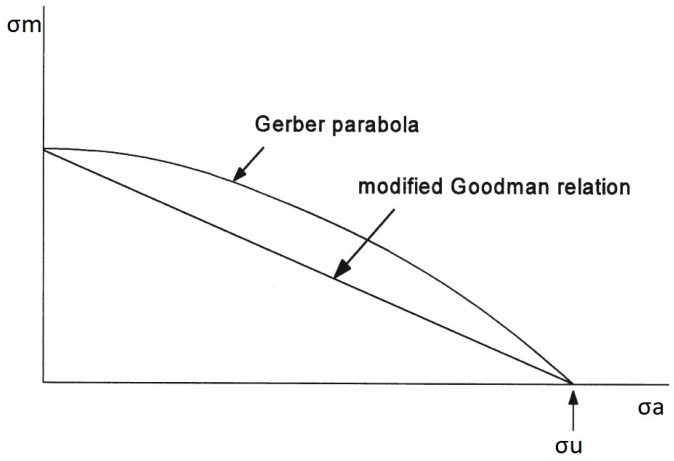

Figure 19: The modified-Goodman-relation and the Gerber-parabola.[29]

Two of the most common failure lines is the modified-Goodman-relation and the Gerber parabola, as shown in Figure 19. They both assume a failure line between the point of reverse bending stress (σ_m=0 , σ_a=σ_{bw}) and the ultimate tensile strength (σ_m=σ_u , σ_a=0). The modified-Goodman-relation assumes a linear failure line, while the Gerber-parabola assumes a parabolic failure line.

$$\sigma_a = \sigma_{bw}(1 - \frac{\sigma_m}{\sigma_u}) \tag{29}$$

$$\sigma_a = \sigma_{bw}(1 - \frac{\sigma_m^2}{\sigma_u^2}) \tag{30}$$

The way to generate the Modified-Goodman line and the Gerber line is shown in equations 29 and 30 respectively. Generally speaking the Modified-Goodman line is more accurate for high-strength materials of low ductility, while the Gerber-parabola is more accurate for low-strength, high ductility materials, particularly for high amounts of load cycles.[16, 29]

Creep. This is a form of wear where the material slowly deforms (creeps) over time, even at stress levels well below the yield limit. It is influenced by three factors; temperature, stress and time. Creep tends to increase as the temperature approaches the melting point of the material, but significant deformation due to creep may occur even at room temperature. Creep is a quite complicated wear mechanism, and experimental data on creep behaviour of engineering materials are very sparse.[16]

2.7 Piston wear

Pistons are subjected to a wide variety of conditions that may cause wear. Because of this, the root cause of failure is not always easy to point out. The tribology handbook groups diesel engine piston wear into three types.

- Wear resulting from improper rubbing conditions between the piston and the cylinder. This usually stems from problems with the lubrication.
- Overheating. This is related to the cooling arrangements and combustion conditions. Issues with either one, or a poor compromise between thermal loading and cooling may lead to overheating.
- Mechanical overload. This may happen if the strength or stiffness of the piston assembly does not match the load conditions of the engine.

Skirt seizure is an example of piston failure that may be caused by overheating. The piston typically has a greater thermal expansion coefficient than the cylinder, which means that is may expand beyond the size of the cylinder during excessive temperatures. This issue may also be caused by improper cooling arrangements, or a poor piston profile.

Cracking inside the piston is usually caused by inadequate strength or stiffness, and typically occurs near the piston pin boss or inside the piston rings. According to the tribology handbook, 69MN/m^2 is a typical limit for maximum bearing pressure for the pin boss of an aluminium piston.

Rings sticking in their grooves is a problem caused by the ring groove temperatures being too high, causing the piston rings to behave sluggishly or be completely fixed in their grooves.[8]

Fatigue damage in pistons. Piston failure is usually attributed to wear and lubrication issues, however fatigue cracks are often present in damaged pistons, implying that fatigue is often the root cause of failure. [30]

In the work of F.S. Silva fatigue damage on engine pistons was studied in detail; with a focus on damage initiating on the piston crown, ring grooves, pin boss and skirt of aluminium pistons. Silva groups fatigue into two categories:

- Mechanical fatigue. Caused by high local stresses in critical areas which leads to a crack forming and propagating. Mechanical fatigue is often aided by high temperatures, which decreases the local fatigue resistance, even though the material remains the same. High temperatures also includes some creep.
- Thermal/thermal-mechanical fatigue. Because of temperature gradients in the piston, thermal stresses are formed. These stresses are often difficult to predict, since the piston has both a vertical and a horizontal thermal gradient.

A notable difference between mechanical and thermal/thermal-mechanical fatigue is that thermal/thermal-mechanical fatigue tends to form multiple cracks, while mechanical fatigue tends to produce only one prevailing crack.

Piston crown and piston boss fatigue damage was found to be the most common form of fatigue damage in pistons. The gas force induces stresses mainly in two areas; the piston crown and around the pin boss.

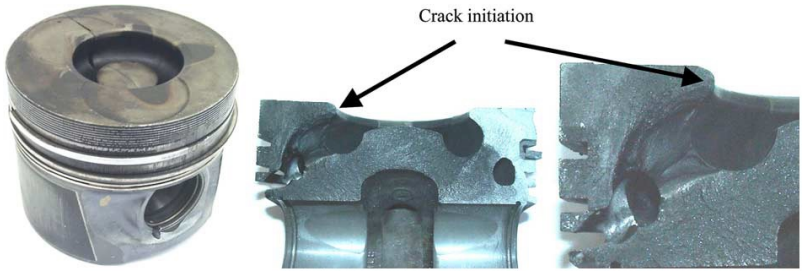

Figure 20: Engine piston with cracks formed at the combustion bowl rim. [30]

Considering that the combustion bowl rim has the highest temperature, it is the weakest part of the crown, and most vulnerable to fatigue. The maximum tensile stress occurs in the plane containing the piston pin. Silva assumed that this is why cracks formed by mechanical fatigue on the crown mainly occurs at the combustion bowl rim, at a point right above the pin boss as shown in Figure 20.

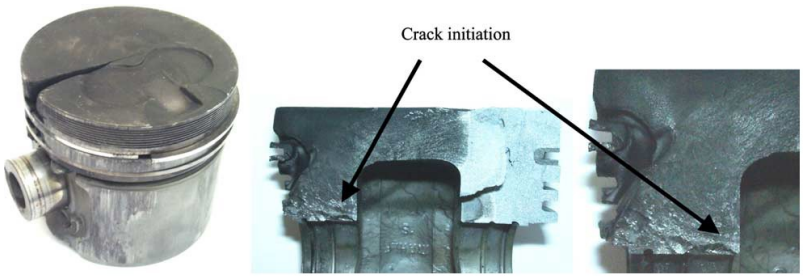

Figure 21: Engine piston with cracks formed at the piston pin boss. [30]

Static stresses concentrate mainly on the piston pin boss. This is true for practically all pistons, and explains why cracks may be initiated at the pin boss, as shown in an example in Figure 21. The reason why most cracks tend to form on the combustion

bowl rim even though the pin boss has the highest stress concentration is not answered in the paper; but it is assumed to be related to the temperature difference, as the bowl rim has a much higher temperature than the boss.

The piston ring grooves is another typical initiation site for cracks. It was shown that there is a stress concentration on a stress radius of the groove mainly when the piston ring is not inside the groove, and that there is an exponential increase of stress when the piston ring moves away from the piston, out of the groove. A typical example is shown below.

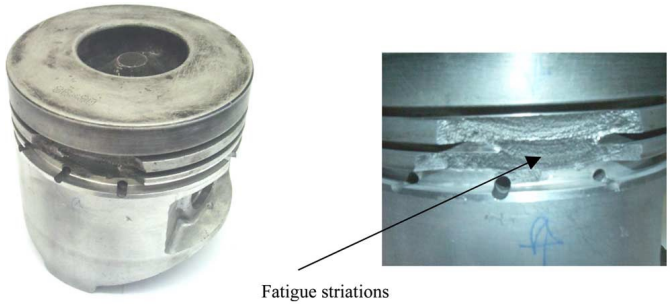

Figure 22: Engine piston with damaged grooves. [30]

As shown in Figure 22 it is clear the piston ring grooves were damaged by fatigue. This type of fatigue is mainly dependant on the clearance between the piston ring and the cylinder wall, rather than on the piston itself.[30]

M.Caldera et al. conducted a failure analysis of a damaged piston for a direct injection (DI) diesel engine.[26] The analysis was performed on a cast aluminium piston with a cooling gallery and a cast iron insert on the top ring groove. The piston was from a turbocharged light truck engine running at 3600 rpm with a mean effective pressure in the range of 20 bar and peak pressure in the 180-200 bar range. Temperature in the piston crown was about 400 °C.

The mode of failure was a fracture in the combustion bowl going through the cooling gallery and the ring zone. The damage occurred right above the piston pin, in the pin-plane. The damage was a form of thermomechanical fatigue, aided by material degradation and pitting. The pitting of the surface was assumed to be caused by erosive wear, and connected by a network of micro-cracks from thermal fatigue. It was surmised by the authors that this could explain the initiation of the fatigue fracture.[26]

The limits of a piston. A piston is typically limited by some thermal and mechanical limits. In a paper by D. Fletcher-Jones, W.J. Griffiths and Dr. R. Munro, some typical temperature limits for a cast aluminium piston with no cooling is listed.[31]

- Maximum temperature at the combustion bowl rim: 320°C
- Maximum temperature at the boss and support strut region: 200°C
- Maximum temperature at the top ring groove: 250°C

The tribology handbook lists the maximum bearing pressure in the pin boss as 69N/mm^2[8], while a paper from KS recommends a maximum bearing pressure of 65N/mm^2.[12]

3 Methodology

Before creating the model of the piston, two things were needed: the dimensions and the mechanical and thermal boundary conditions.

3.1 Geometry of the piston

The dimensions of the piston and the piston pin were not known on beforehand and had to be measured. The piston pin and the piston exterior was measured using vernier callipers. However the piston interior was more complex and difficult to reach using callipers, so a microscribe digitizer had to be used.

Figure 23: The microscribe and vernier callipers.

Figure 23 shows the microscribe and the callipers used to measure the dimensions of the piston and the piston pin. The measurements were done on a granite table. The piston and piston pin were also weighed, and the weight of the piston (including the piston rings) was found to be $m_s = 0.802\,\text{kg}$ and the weight of the piston pin was found to be $m_{pin} = 0.296\,\text{kg}$.

Microscribe: The microscribe shown in Figure 23 works by mapping the exact position of the tip of the stylus at all times. A brief explanation of how it was used is given below.

- The microscribe transfers data to a pc using an RS-232 to USB cable, so first a driver for RS-232 must be installed.
- It is also necessary to install some software that works with the microscribe. A lot of options are available, and a common program to use for this is Rhinocerus, since it works directly with the microscribe and does not require additional software.
- The microscribe must be connected. It has one power cable, one RS-232 to USB for data transfer to pc, and one accessory input, where a pedal is plugged in. The pedal is used to signal the microscribe for it to take a measurement.
- Once the microscribe is plugged in, it should show up in "device manager". If not, the driver installed in the first step does not work.
- After entering Rhinoceros and connecting the microscribe through the "Tools" menu, the instrument needs to be calibrated.
- First the microscribe needs to be "homed". The stylus is placed in its holder, and the microscribe is rotated counterclockwise until it stops.
- Now a coordinate system must be defined. This is done by measuring three points, corresponding to the origin, one point at the x-axis and one at the y-axis. From this a coordinate system will be created, and this coordinate system in the real world is mapped to the coordinate system in rhinoceros.
- Now the microscribe is ready to measure points and map them to rhinoceros. A few points at a flat surface should be measured and compared to check the accuracy of the calibration done previously. The microscribe may be re-calibrated as many times as needed.
- The microscribe has two options, it may measure "multiple points" or be used to "sketch a curve". The latter is not an actual curve, but points being generated continously as the stylus is moved while the pedal is held down, while the multiple points option only measures when the pedal is pressed.
- Using the points as a basis, a model may be generated though connecting the dots, either directly or using approximation functions in order to generate curves and surfaces from the measured points. This is then reduced back into dimensions like length and radius, and is used to create a complete drawing of the piston.

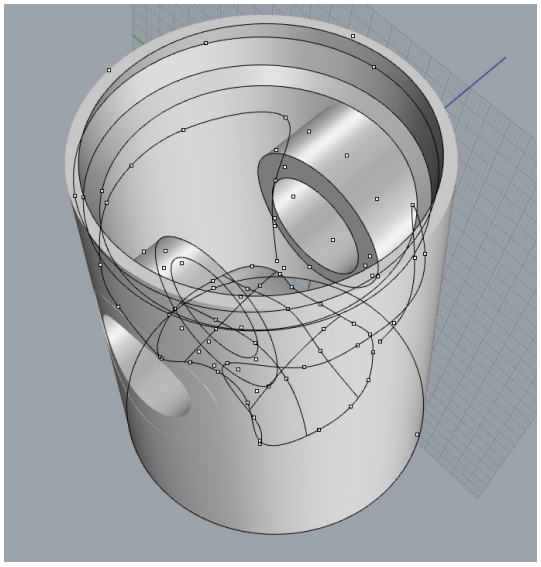

Figure 24: The interior of the piston drawn in Rhinoceros 5.

The microscribe measures a set of points in space and maps them to a virtual coordinate system in Rhinocerus. The points may be used to approximate lines and surfaces of the complex interior of the piston. The results from Rhinocerus is shown in Figure 24 and were used to find the dimensions of the piston interior so that they could be added to the complete drawing of the model.

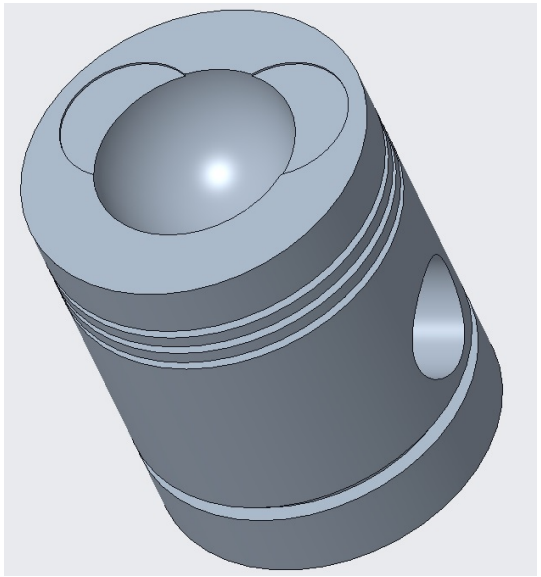

Figure 25: The 3D piston model drawn in Creo parametric.

The complete drawing of the model was done in Creo, and is shown in Figure 25. The 2D drawings with the dimensions are shown in Appendix B. This will be used as a starting point for creating the final model in Abaqus.

The drawings contain a lot of sharp edges. This is partly because the chamfers and rounded corners could not be measured accurately, and partly because these types of features tend to complicate the meshing process. For this reason, chamfers and rounded corners will be added in Abaqus, but are not included in the drawings. This simplification will make it easier to find a good compromise between a good mesh and an accurately dimensioned model.

3.2 The boundary conditions

3.2.1 Mechanical boundary conditions

Both the gas force and the oscillating force is acting on the piston as a mechanical load. The oscillating force is calculated from Equation 22, but from the perspective of the piston, only the piston mass counts as an oscillating mass. The R/L ratio is known from earlier measurements done on the engine, and the stroke and the bore is known from the engine data. The piston was weighed in order to find the oscillating mass.

The gas force is calculated from experimental data for a given state of the engine. In addition to the cylinder pressure curve, several other quantities of interest are known about the reference state of the engine.[2, 1]

- D = 87mm
- λ = R/L = 0.3521
- m_p = 0.802kg
- N = 1500 rpm
- BMEP = 6.8bar
- T_{water} = 72.5°C
- T_{intake} = 303K

The oscillating force is calculated from Equation 22 and the gas force is calculated from Equation 21. They are plotted against the crank angle to give an idea of the mechanical load of the engine throughout the four strokes.

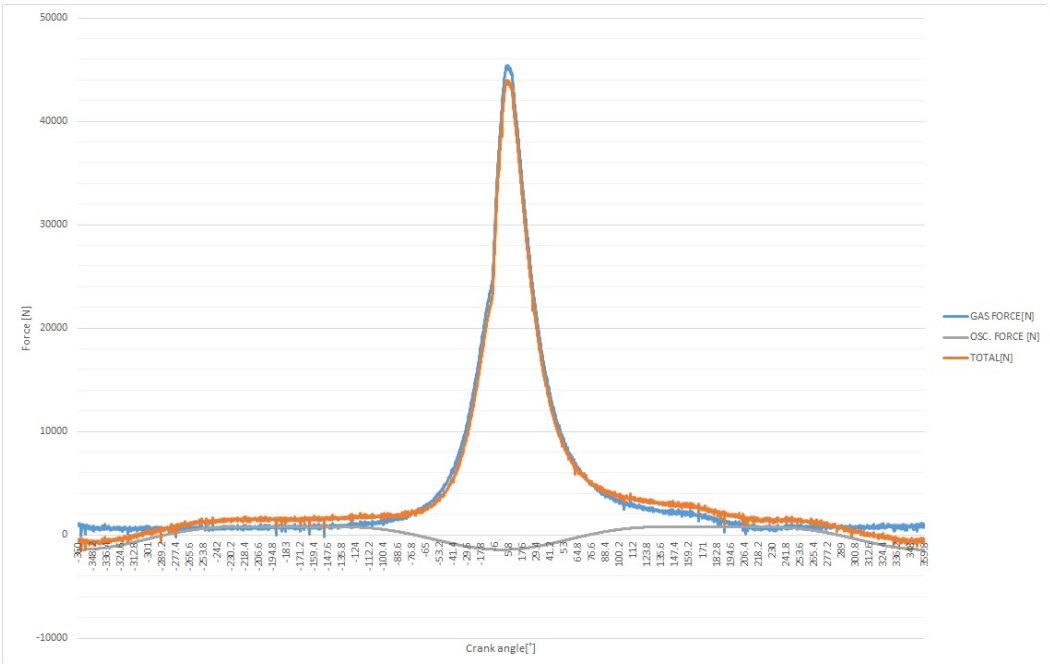

Figure 26: The mechanical forces acting on the piston.

As shown in Figure 26, the piston is mainly influenced by the gas force as expected, with a maximum value of about 45kN during the power stroke. The oscillating force is slightly reducing the maximum force on the piston, while creating a force in the negative upwards direction during the exhaust stroke. This corresponds well with the expected behaviour for the piston force shown in Figure 16.

The maximum negative force created by the oscillating force is roughly equal to -500N, which is quite small compared to the maximum gas force. Including both cases of the maximum gas force and the maximum oscillating force in the downwards direction in Abaqus would mean to create two different models; one where the piston is pressed downwards on the piston pin due to the gas force and one where the piston is pushed upwards on the piston pin due to the oscillating force.

Considering the oscillating force is marginal compared to the gas force, it is rounded off to zero as a simplification. This means that the mechanical loading varies between no load and a maximum load of roughly 45kN, and the issue of having to built multiple different models is avoided.

3.2.2 Thermal boundary conditions

The temperature field is assumed to be quasi-stationary for a constant engine speed and load, so a steady-state analysis is sufficient. Y. Lu et al. performed a transient

analysis of a diesel engine piston, and the results showed that the transient temperature fluctuation does not exceed 5% of the steady-state value, making steady-state thermal analysis a valid assumption.[32] While heat transfer due to radiation is present, it is usually neglected due to being quite small compared to the convective heat transfer.[6]

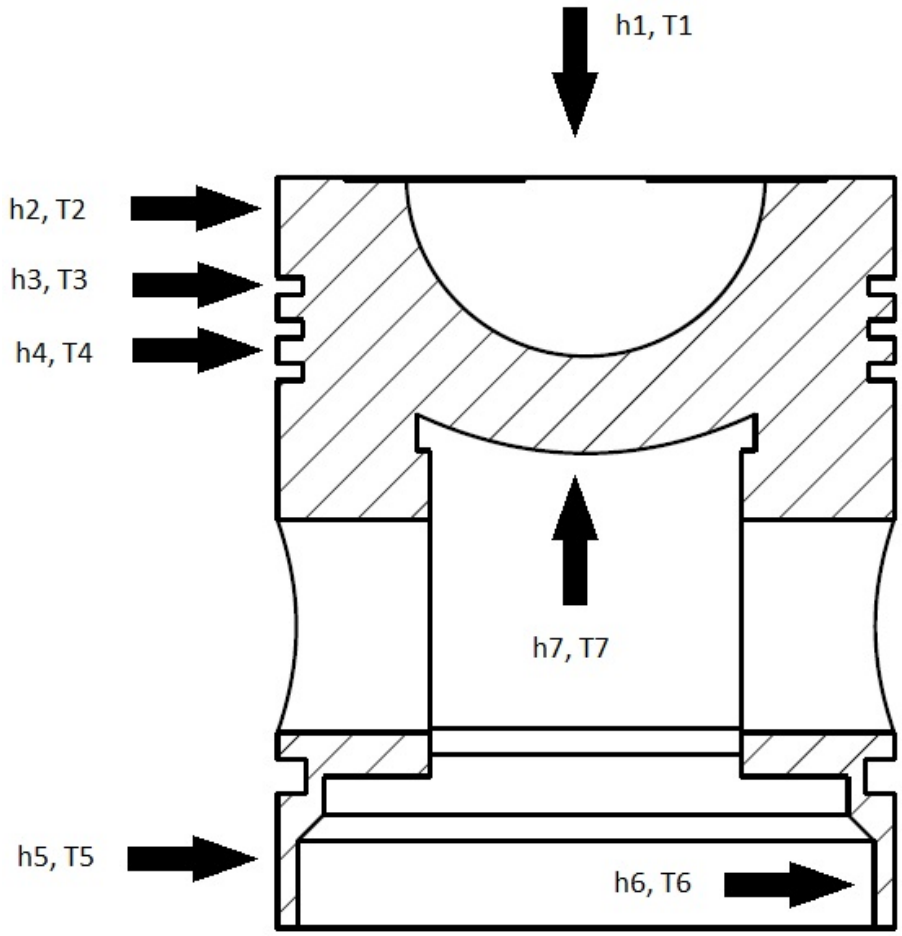

Figure 27: The different heat transfer zones of the piston.

In Abaqus, heat transfer is specified as a film condition, requiring an external temperature source/sink and the film coefficient, h which is equivalent to the overall coefficient of heat transfer (COHT) if multiple thermal resistances are involved as shown in Equations 7 and 16. The film condition is applied to the various surfaces of the piston, with the corresponding values for temperature and COHT. The piston is divided into seven areas for heat transfer, in addition to the heat transfer between the piston and the piston pin,

as shown in Figure 27. These areas are (in order) the combustion zone, the top land, the piston rings, the second and third land, the piston skirt exterior, the piston skirt interior and the combustion bowl underside.

In order to achieve an accurate simulation of the temperature field, experimental data is needed. Firstly, measurements of the temperatures in certain areas must be measured for a given working state of the engine. Then the variables in the FEM-simulation must be calibrated so that the simulated temperature field matches these known values. Unfortunately the temperature field is dependant on more than 14 variables, making it very difficult to optimize and reduce the error. For this reason more data about the engine must be known, including the temperatures of the cooling arrangements and the dimensions of the cylinder liner.

This information is not currently available, and doing a proper thermal analysis for the engine is recommended as further work. For this reason, this work will be aiming to find a representative temperature field for the piston rather than an accurate one. Estimations and simplifications will be done to find cycle-averaged temperatures and their corresponding COHT, and the resulting field will be calibrated towards some older measurements on a similar piston under similar working conditions.

Combustion chamber. Getting the instantaneous gas temperatures in the combustion chamber and the corresponding COHT is a difficult task, both theoretically and experimentally. In this work, crude simplifications will be done to get an estimate. In order to calculate the temperature, it is assumed that the combustion process can be described by the ideal gas law, and that the trapped gas can be approximated to have the properties of air. This is not an accurate method by any means, but it is sometimes used for crude estimations.[14]

$$T_{gas} = \frac{V_x P_{gas}}{m R_i} = \frac{V_x P_{gas} M}{m R_u} \tag{31}$$

Where T_{gas}, V_x, P_{gas} is the instantaneous cylinder temperature, volume and pressure respectively. The molar mass M is approximated to that of air, namely M = 0.029 kg/mol. R is the universal gas constant, R = 8.314 m^3Pa/K mol, and m is the trapped mass in the cylinder. P_{gas} is known from the cylinder pressure curve, but V_x and the trapped mass m needs to be calculated.

The instantaneous cylinder volume ay be calculated from known engine data. It is calculated by the equation:

$$V_x = V_c + \frac{B^2}{4}\pi S(\alpha) \tag{32}$$

The size of the bore is known from the engine data, B = 87.3 mm. The position of the stroke S and the clearance volume at TDC (V_c) needs to be calculated. The clearance volume can be calculated from:

$$V_c = \frac{V_H}{\epsilon - 1} \tag{33}$$

Where ϵ the compression ratio, and is known to be 16.5. The displacement volume V_H may be calculated from the bore and stroke of the engine, which are also known.

$$V_H = \frac{B^2}{4}\pi\, s = \frac{87.3^2}{4}110\pi = 658432.2mm^3 \tag{34}$$

Giving a clearance volume of $V_c = 42479.5mm^3$. Now, only the piston position $S(\alpha)$ is required to calculate V_x, and this may be found by the formula:

$$S(\alpha) = \frac{s}{2}(1 - cos(\alpha) + \frac{\lambda}{2}sin^2(\alpha)) \tag{35}$$

Plugging all this into Equation 32, V_x may be calculated. Now, only the trapped mass is needed to calculate the instantaneous gas temperature.

The trapped mass may be estimated as the entrapped air when the intake valve closes. According to the engine data, this happens at 144.5° aTDC. In general, the exhaust valve opens at 144.5° bTDC, so that the gas exchange lasts from 144.5° bTDC to 144.5° aTDC. The fuel injection starts at 24° bTDC.

The cylinder volume V_x at 144.5° is equal to $657310.3mm^3$. Given that the intake air temperature is known to be 303K and the pressure in the cylinder at the end of the intake is assumed to be 1.01bar, the trapped mass may be calculated from the ideal gas equation. For air, the molar mass M is equal to 0.029 kg/mol.

$$m = \frac{MPV}{TR_u} \tag{36}$$

This gives a trapped mass of m = 764.253x10^{-6} kg for each cycle of the engine. This is then plugged into Equation 31 together with V_x and is used to calculate the instantaneous gas temperature for the engine.

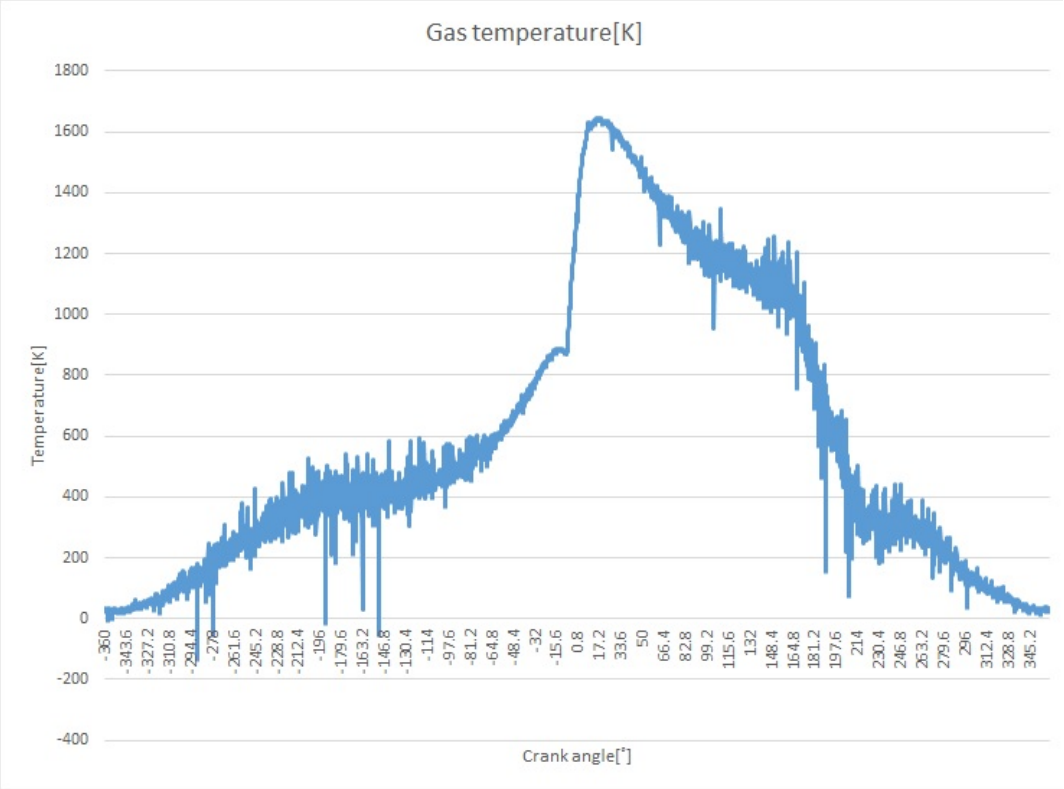

Figure 28: Instantaneous gas temperature plotted for crank angles.

Figure 28 shows the results from the calculation. The cycle averaged temperature is found to be 583K. Note that the temperature goes towards absolute zero at TDC during the gas exchange. This is because the trapped cylinder mass is constant, while in reality it changes during the gas exchange. A crude way to correct for this is to constrain the gas temperature so that it never goes below 303K, which is the temperature at the intake stroke.

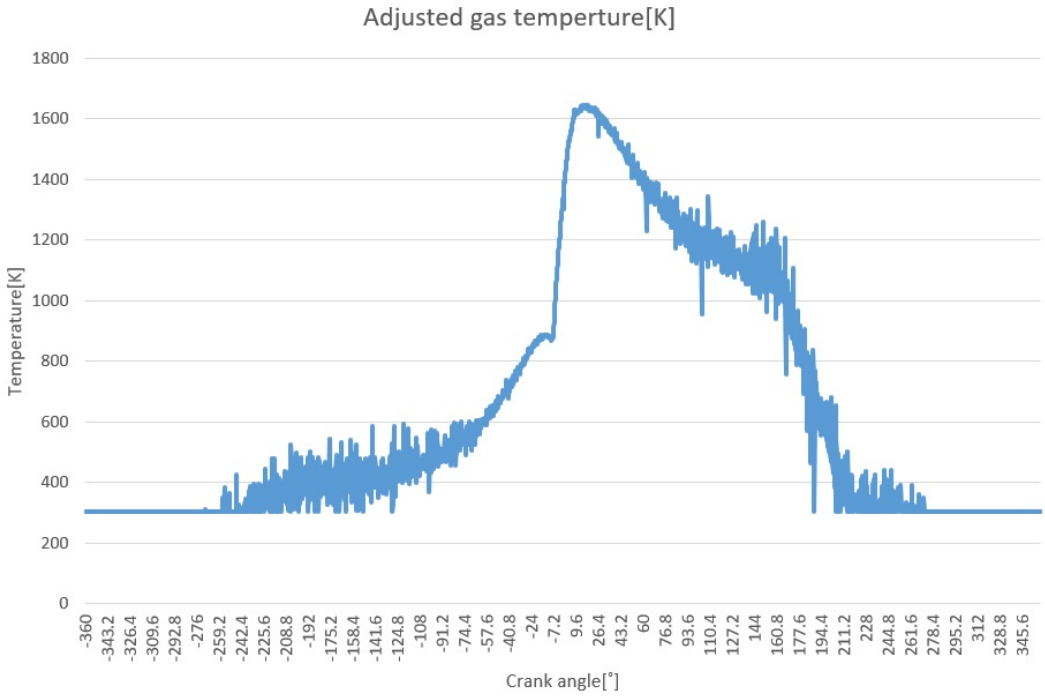

Figure 29: Adjusted instantaneous gas temperature plotted for crank angles.

Figure 29 shows the adjusted values for the gas instantaneous gas temperature. This gives a cycle average temperature of 638.3K. In reality the average temperature should be a higher, as the exhaust temperature is not known or accounted for. For this work, the initial value of the cycle averaged instantaneous as temperature will be $T_1 = 365.3°C$.

Now that the instantaneous gas temperature is calculated, the COHT may be calculated from a variant of the Woschni equation.

$$h_1 = 129.8P(\alpha)^{0.8}B^{-0.2}T(\alpha)^{-0.55}(c_1c_m + c_2\frac{V_HT_r}{P_rV_r}(P(\alpha) - P_m(\alpha)))^{0.8} \tag{37}$$

The constants c_1 and c_2 are empirical constants. For a DI engine, $c_1 = 6.18$ for the gas exchange and $c_1 = 2.28$ otherwise, while the combustion constant $c_2 = 0.00324$ during the combustion and expansion, and $c_2 = 0$ elsewhere. The values T_r, P_r and V_r are the state of the trapped gas at a reference state. In this case, the state at the closing of the intake value may be used, so that $P_r = 1.01$bar, $T_r = 303$K and $V_r = V(144.5°) = 657310.3mm^3$. The values that need to be calculated are the mean piston speed c_m and the motoring pressure P_m. Note that the cylinder pressure P must be expressed in bar.[7]

The mean piston speed can be calculated from the engine speed and stroke length.

$$c_m = \frac{2\,s\,N}{60} = 5.51 m/s \tag{38}$$

The piston motoring pressure is the portion of the pressure that would occur without combustion, simply from the piston compressing the trapped gas. A simple way of evaluating this is to assume it is a polytropic process. The polytropic constant is given as k = 1.3.

$$P_m = P_r(\frac{V_r}{V})^k \tag{39}$$

Where P_r and V_r are the same reference state as for Equation 37. Plugging all the variables into the Woshni equation, and using the previously mentioned crank angles to make c_1 and c_2 have the correct values for the different crank angles, the COHT for the heat transfer between the piston and the trapped gas can be calculated.

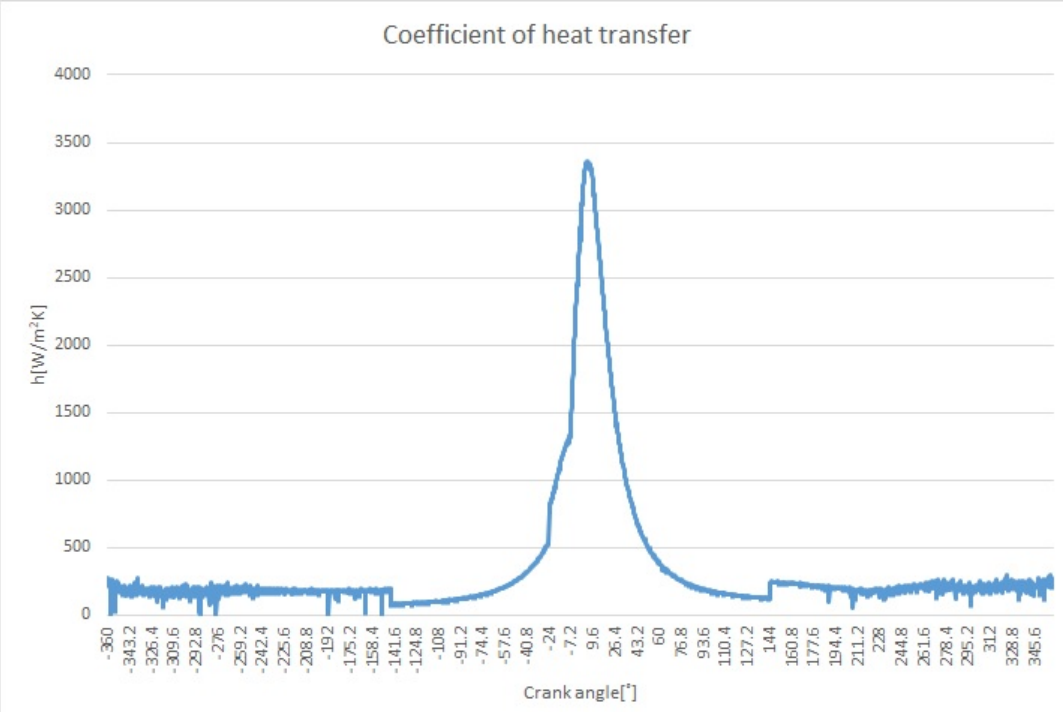

Figure 30: Calculated COHT plotted for crank angles.

Figure 30 shows the COHT for the entire cycle, and the cycle averaged COHT is equal to $h_1 = 350.6$ W/m^2 K.

Top land. For the top land th heat transfer is a bit different than for the other lands, as this land is technically part of the combustion chamber and is exposed to the hot combustion gases. Because the clearance between the land and wall is very small, the captured gas temperature is the mean temperature of the two surfaces. A common way to calculate the heat transfer in this area is by using the formula below.

$$k\frac{T_{piston} - T_{wall}}{\Delta x} = h(T_{piston} - T_{wall}) \tag{40}$$

$$h = \frac{k}{\Delta x} \tag{41}$$

Here Δx is the clearance, and k is the conductivity of the gas at its thermodynamical state at the given temperature and mean pressure. The heat transfer is represented by the film coefficient calculated by the equation above and the cylinder wall temperature. The cylinder wall temperature and the conductive properties of the combustion gases at the given temperatures and pressures is not known, and so some representative values are borrowed. This gives $h_2 = 230\text{W/m}^2\text{K}$ and $T_2 = 300°\text{C}$.[19] Note that in this case the temperature T_2 is the temperature of the cylinder wall, not the cooling water.

Piston rings. The heat transfer between the piston rings and the cooling water may be represented as a series of thermal resistances, including the piston rings, the oil film, the cylinder liner and the cooling water.

$$R_{total} = R_{ring} + R_{oil} + R_{liner} + R_{water} \tag{42}$$

By knowing the dimensions of the piston, the piston rings and the cylinder liner, it is possible to calculate the COHT of the piston-to-coolant system. Doing this is beyond the scope of this work. A representative value of $U_3 = 625\text{W/m}^2\text{K}$ is borrowed for the piston rings,[19] and the cooling water temperature is known to be $T_3 = 72.5°\text{C}$.

Ring lands. Through the same argument used for the piston rings, the COHT of the ring lands is $U_4 = 115\text{W/m}^2\text{K}$ is used[19], and the cooling water temperature is known to be $T_4 = 72.5°\text{C}$.

Outside of piston skirt. The temperature of the outside of the piston skirt may be calculated using the same method as for the piston rings. For this work, a representative value of $U_5 = 60\text{W/m}^2\text{K}$ is used[19], and the cooling water temperature is known to be $T_5 = 72.5°\text{C}$.

Inside of the piston skirt. The inside of the piston skirt is mainly cooled by the oil mist. The COHT is given by the empirical formula:

$$h_6 = 240\frac{N}{4600}^{0.35} = 240\frac{1500}{4600}^{0.35} = 162W/m^2K \tag{43}$$

Where N is the engine speed in rpm. The temperature of the oil in the crank case is assumed to be $T_6 = 110°C$.[19]

Underside of the combustion chamber. The underside of the combustion chamber is subjected to oil splash from the oil sump, increasing the heat transfer rate. A simple empirical formula dependant on only engine speed may be used to calculate the COHT:

$$h_7 = 900\frac{N}{4600}^{0.35} = 900\frac{1500}{4600}^{0.35} = 608W/m^2K \tag{44}$$

Where N is the engine speed in rpm. The temperature of the oil in the crank case is assumed to be $T_7 = 110°C$.[19]

	COHT[W/m^{2}K]		T[°C]	
(1) Combustion zone	350.6	Calculated	365.3	Calculated
(2) Top land	230	Borrowed[19]	300	Borrowed[19]
(3) Rings	625	Borrowed[19]	72.5	Measured
(4) 2^{nd} and 3^{rd} lands	115	Borrowed[19]	72.5	Measured
(5) Skirt outside	60	Borrowed[19]	72.5	Measured
(6) Skirt inside	162	Calculated	110	Borrowed[19]
(7) Combustion underside	608	Calculated	110	Borrowed[19]

Figure 31: Initial thermal boundary conditions.

The thermal boundary conditions to be used as a starting point for the thermal analysis is shown in Figure 31.

The piston-pin thermal interaction. The piston and the piston pin are thermally in contact at the piston boss. The contact resistance is regarded as negligible due to both surfaces being smooth, the presence of oil and the piston boss being softer than the pin which makes it conform to its shape and increase the surface contact area.

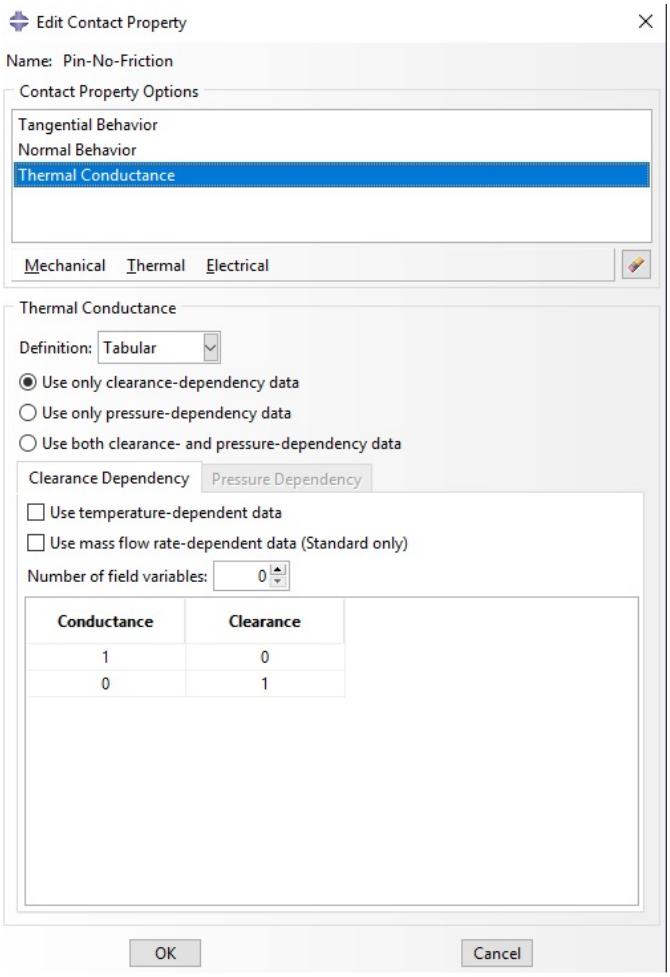

Figure 32: The thermal contact interaction menu from Abaqus.

In Abaqus the thermal contact condition may be given by a relationship between thermal contact conductance and contact clearance, as shown in Figure 32. At 0mm clearance, a thermal contact conductance of 1 W/mm^{2}K is given, which should make the thermal resistance negligible compared to the conductive resistance. Over a distance of 1mm the thermal contact conductance slowly drops to zero. This is to account for the heat transfer through the oil film between the pin and the boss.

3.3 Test models

The diesel engine piston is a very complex construction with a lot of variation in the physics and overall behaviour. In order to test and investigate this, several simple models were made in Abaqus and used as testing grounds throughout the development of the final model. Some of these models are listed and briefly explained in this chapter.

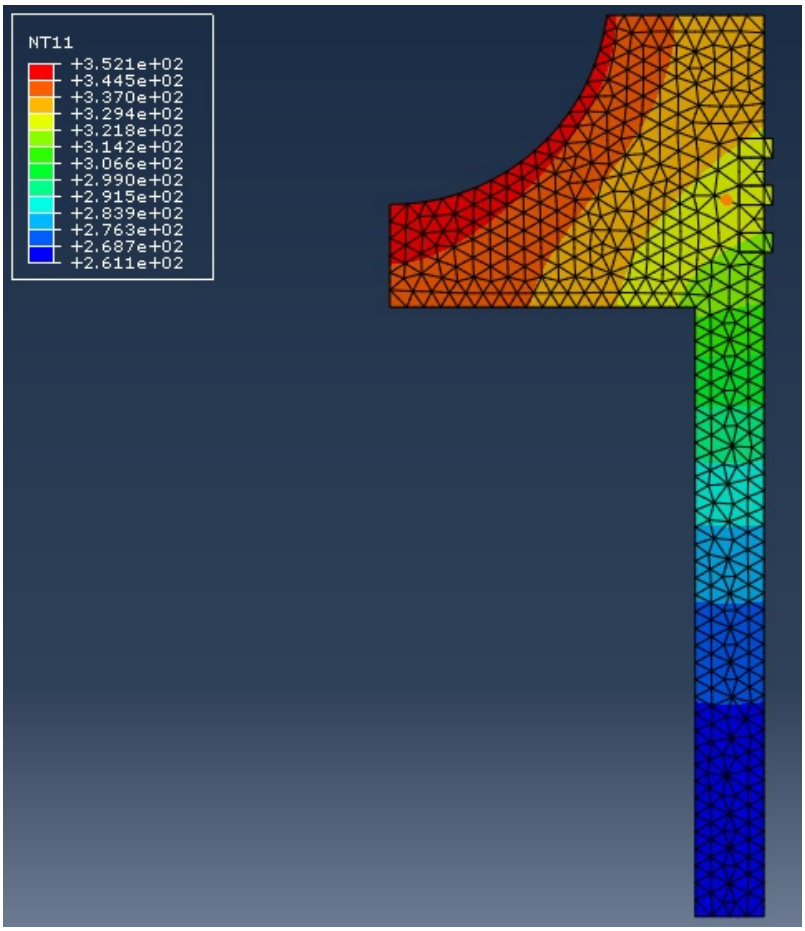

Figure 33: Early 2D model for thermal loading only. NT11 is referring to the nodal temperature [°C].

Figure 33 shows a very early 2D model used to investigate the thermal loading of the piston. This model is very incomplete by the standards of the final model, but was quite useful early on for testing how different thermal boundary conditions changed the temperature field of the piston.

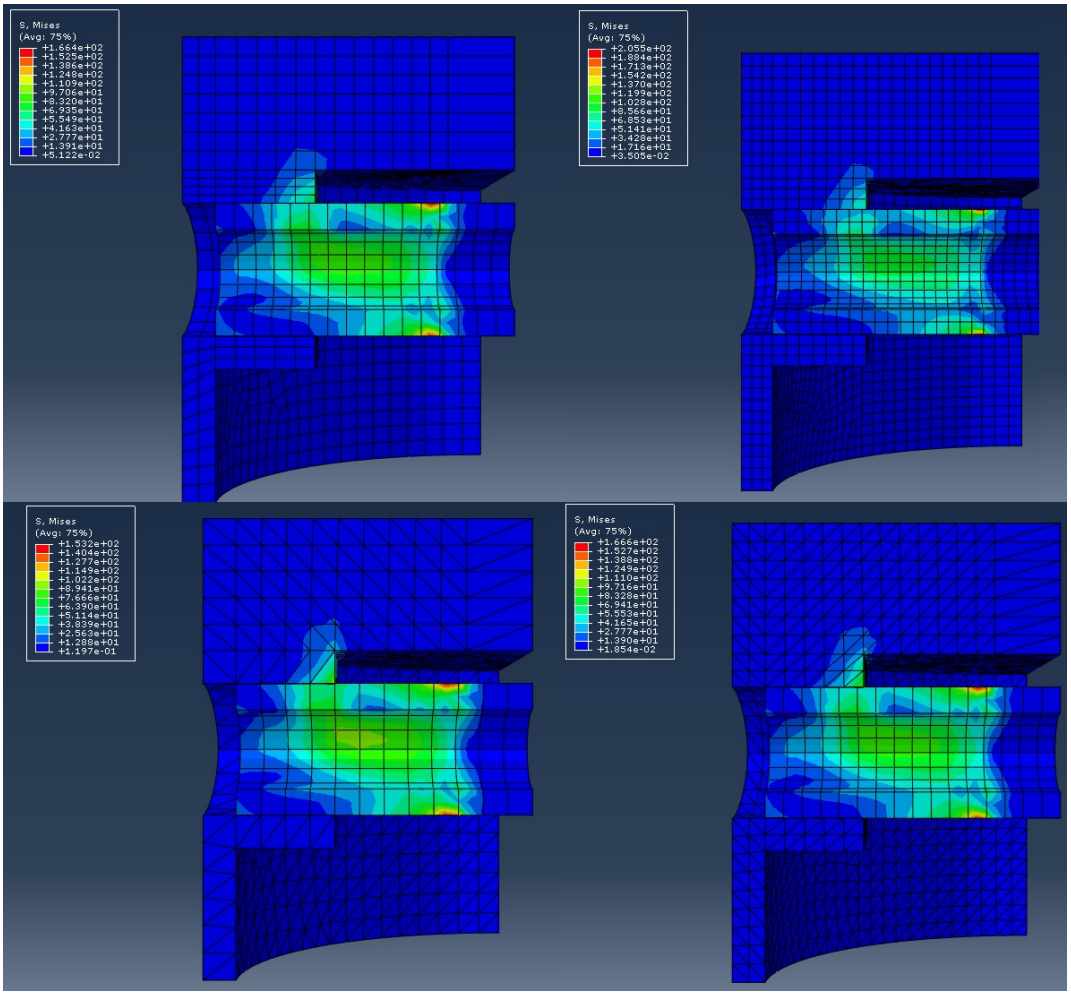

Figure 34: Comparison of hex- and tet-elements, showing the Mises stress [MPa]

Figure 34 shows a comparison of the piston being meshed using hexahedral elements compared to tetrahedral elements, in order to verify that the behaviour would be the same. The final piston model was too complex to achieve an acceptable hexmesh, so tetrahedral elements had to be used.

In order to verify that the hexahedral elements would not produce nonsense, a simple piston model was made and used to verify that hexahedral elements could be used. It was found that a hex-meshed pin and a tet-meshed piston gave the best results.

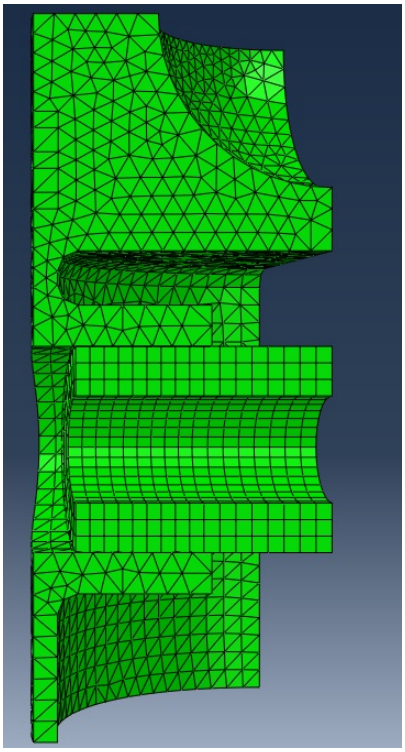

Figure 35: A model of the piston before the interior support was added.

Figure 35 shows a model of the piston before the interior dimensions were known. Because of this the mechanical behaviour around the pin boss is not accurate, but the model was very useful in trying to get the contact interaction to work, how and where to add the mechanical and thermal boundary conditions, and generally to get a rough idea of how the final model would act.

3.4 The final model

Once the dimensions and boundary conditions were known, a final model could be made in Abaqus.

Unit	**Meterbasis**	**Millimeterbasis**
Length	10^{-3}m	1mm
Pressure/Youngs modulus	1MPa	1Pa = 1N/mm^2
Temperature	1K	1K
Thermal conductivity	1000W/mK	1W/mmK
Thermal flux	10^6W/m^2	1W/mm^2
Thermal expansion coefficient	1/K	1/K

Figure 36: Unit system on a millimeterbasis.

Abaqus does not feature a unit system by default, and will simply return dimensionless numbers. These numbers will correspond to any consistent unit system used to give model input, and the system used for this work is the SI-system on a millimeter scale, as shown in Figure 36.

3.4.1 Creating the mesh

Once the dimensions of the piston were used to draw the final model in Abaqus, the edges in the most critical zones had to be rounded or chamfered to match closer to the actual piston, or the sharp angles would work as stress raisers and generate unrealistically high stresses.

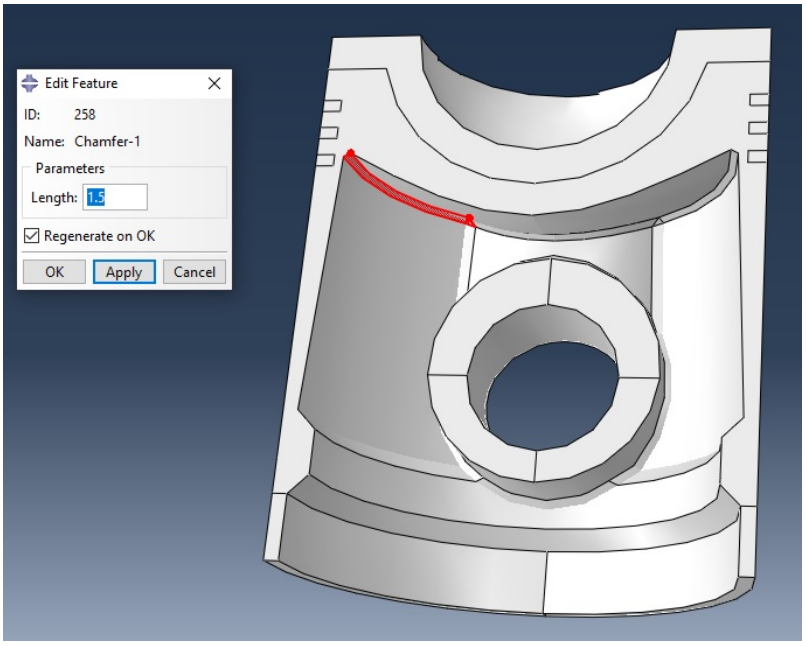

Figure 37: The final model with chamfers and virtual topology.

As shown in Figure 37, chamfers were added around these areas. This is not exactly accurate to the real piston, but rounded edges produced very poor meshing in those areas, so chamfers were chosen as a compromise. Certain surfaces around the boss were also combined using virtual topology in order to generate a proper mesh.

The piston rings are not studied in detail in this work, and so they were simplified as being part of the piston. The borders created by the oil control ring resulted in very poor meshing around the pin boss. Because of this the oil ring was omitted - it does not play a major structural role in the axial stresses studied in this work, nor does it

provide any significant heat transfer due to being placed so far down. If the purpose was to study the lateral forces acting on the piston (as is suggested for further work), the oil ring would have to be included, since it most likely plays an important role in the structural strength of the piston skirt.

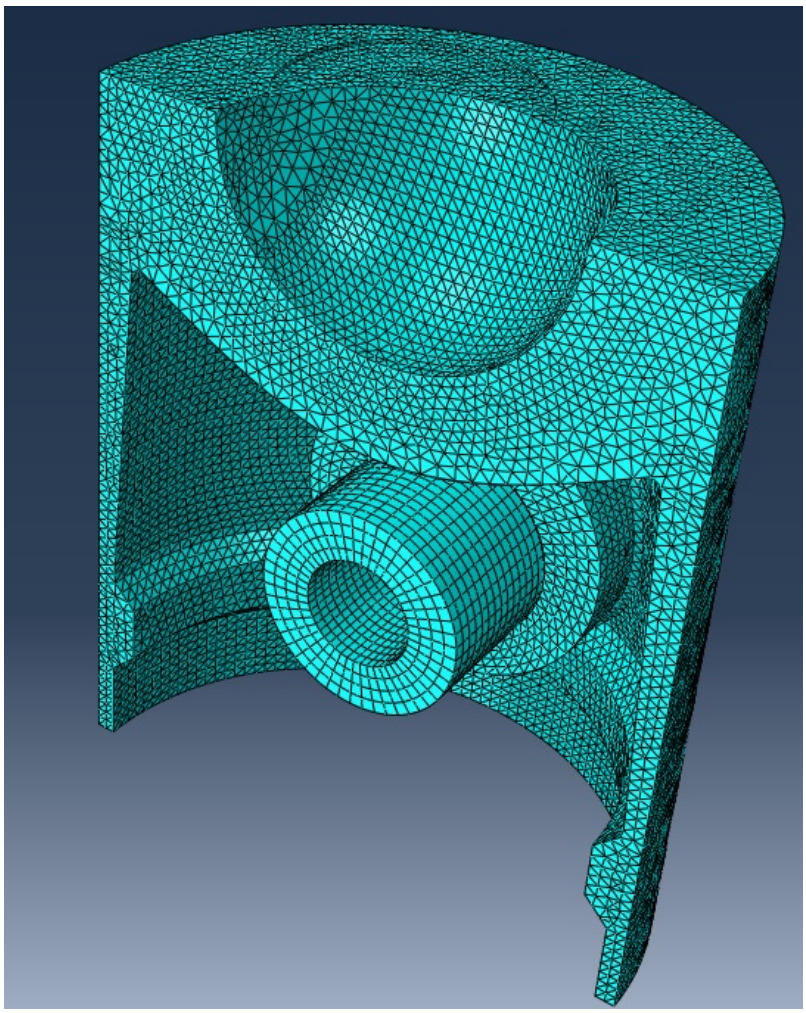

Figure 38: The mesh of the final model.

Figure 38 shows the mesh of the final model, including the piston, piston rings and piston pin. The piston and piston rings are part of the same model, while the piston pin is a separate model. The piston and rings are meshed using C3D4T elements, that is standard, linear, tetrahedral elements for coupled temperature-displacement analysis. The piston pin is modelled using C3D20T elements, that is standard, quadratic, hexa-

hedral elements for coupled temperature-displacement analysis. Theoretically quadratic elements would generate better results, but it was found that for the piston and ring part, it did not increase the accuracy by much, however the computation time increased dramatically.

3.4.2 Adding material properties

The exact materials of the piston is unknown, but it is seen that the piston is cast and made of some type of aluminium. The piston rings seem to be made of cast iron and the piston pin is made of steel. These are very typical materials to use for these purposes, which is discussed in Chapter 1.

The piston material is assumed to be the "classical" AlSi piston alloy M124, whose full table of properties is given in Appendix A. Poissons ratio is unknown, so it is assumed that $\gamma = 0.3$. The requirements for a eutectic AlSi alloy used for diesel engine pistons are quite restrictive, and most other variants of this alloy encountered seem to have very similar properties.[19, 15, 33]

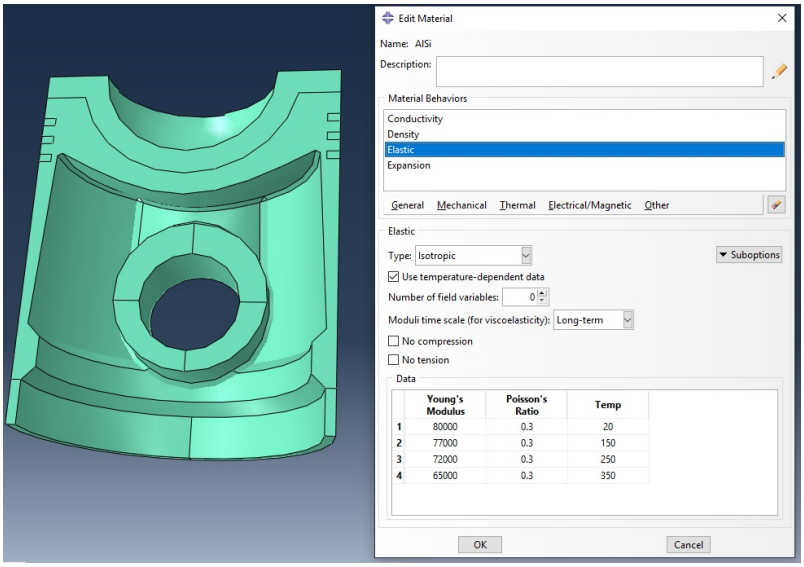

Figure 39: Adding material properties to the piston.

As shown in Figure 39 the temperature dependant properties may be added by enabling temperature dependant data in the materials menu.

The material of the piston pin is assumed to be 16MnCr5, which is a typical form of steel used for this purpose.[6] A list of properties is given in Appendix A. However

in order to make the simulation run more smoothly, the thermal expansion coefficient of the piston pin had to be set to zero. Possibly the greatest challenge in making this model run was to account for the contact surface between the piston and the piston pin constantly changing due to thermal expansion and mechanical deformation. To combat this, the expanding behaviour of the piston pin had to be neglected. This could be justified, as the expanding behaviour of the piston pin is relatively small, and should not greatly affect the behaviour of the piston pin boss, which is the area of interest for this study.

The piston rings are assumed to be made of cast iron. Recall from earlier that the piston ring behaviour were neglected in this work, and the piston rings were assumed to be a part of the piston, just to serve as thermal conductors for the heat transfer. This could be justified if the thermal contact resistance between the piston and the piston rings are assumed to be negligible. Due to this the rings are given a thermal conductivity of 50W/m°C[19, 15], and in order to avoid unrealistic thermal stresses, they are given the same thermal expansion data as the rest of the piston.

This makes sense with respect to thermal loading, but not structurally. This configuration means that the piston rings will contribute to the strength of the piston skirt and resist the bending caused by the gas force. In order to avoid this, the piston rings are given a very low Youngs modulus of $E = 50\,N/mm^2$, to mimic their lack of structural contribution.

3.4.3 Adding steps

The final simulation consists of three steps of the type "coupled temperature-displacement" in order to account for both the thermal and the mechanical behaviour of the piston.

- The initial step.
- Applying the thermal boundary conditions.
- Applying the mechanical boundary conditions.

The thermal behaviour is applied first. A side effect of this is that the snug fit pin and boss will instantly turn into a clearance fit. A very small mechanical force is applied to keep the pin in contact with the top part of the pin boss during the expansion process. Then the mechanical force is applied and the mechanical stresses and deformations develops.

Because of this setup, the purely thermal stresses may be found by looking at the end of the thermal step, while the combined thermal and mechanical loading may be found by looking at the end of the mechanical step.

3.4.4 Adding the thermal boundary conditions

Very crude estimates have been done to find some initial thermal boundary conditions. They will have to be adjusted, but first they will be applied to the model. In order to apply the thermal load to the model, the "film condition" from the interaction menu is used. It requires both a COHT and a temperature source/sink to be applied to a carefully chosen surface.

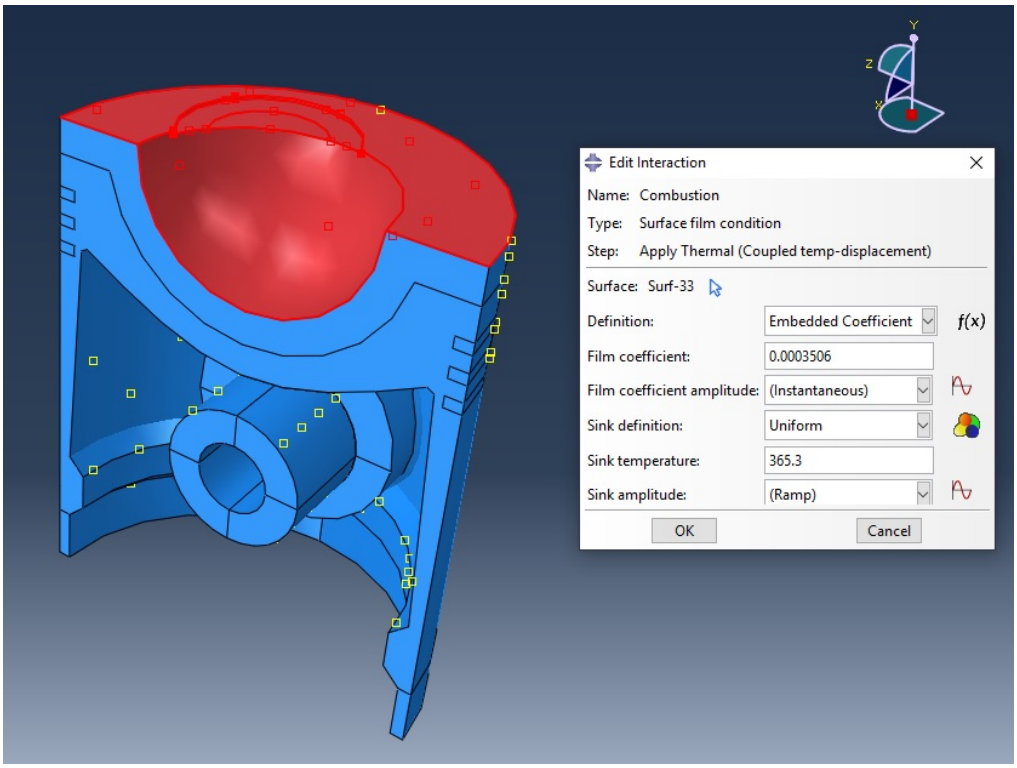

Figure 40: Adding the thermal load to the combustion zone.

As shown in Figure 40, the thermal load for the combustion zone is applied to the entire top surface of the piston. In similar fashion, thermal interactions are applied to the top land, the rings the other lands, the outside and inside of the piston skirt and the combustion bowl underside.

The heating or cooling conditions of the piston pin are unknown, and so it will simply be in equilibrium with the pin boss through its thermal contact, as previously defined in Section 3.2.2.

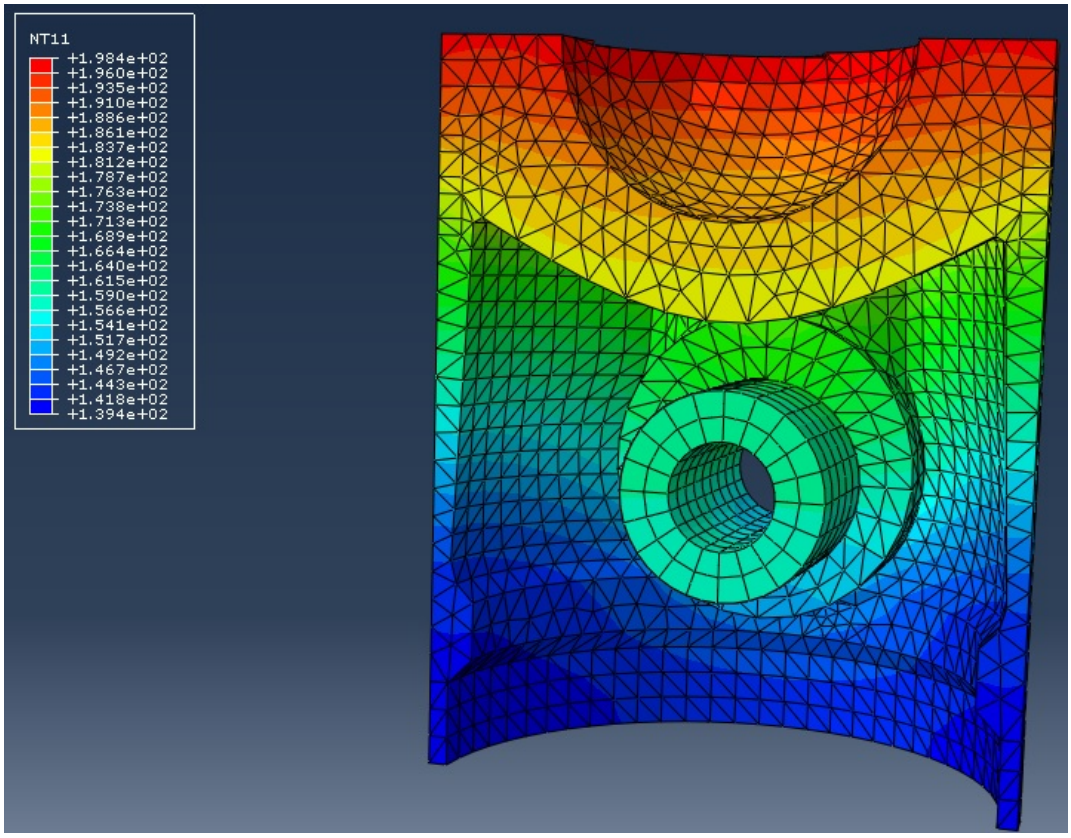

Figure 41: Temperature field with initial thermal loading conditions.

Figure 41 shows the temperature field for the initial thermal boundary conditions. It does not look too bad except that the lateral temperature distribution at the top of the piston seem to increase further away from the combustion bowl which is not typical. This could be explained by the high temperature of the top land heat sink. This value was borrowed from a paper describing a larger engine, and is most likely too high for this case.

3.4.5 Calibration of the thermal boundary conditions

After using some crude boundary conditions to find an initial temperature field, the model must be calibrated towards a more realistic temperature field. Unfortunately this is not available, and so measurements done on a similar piston under similar conditions are used for reference.

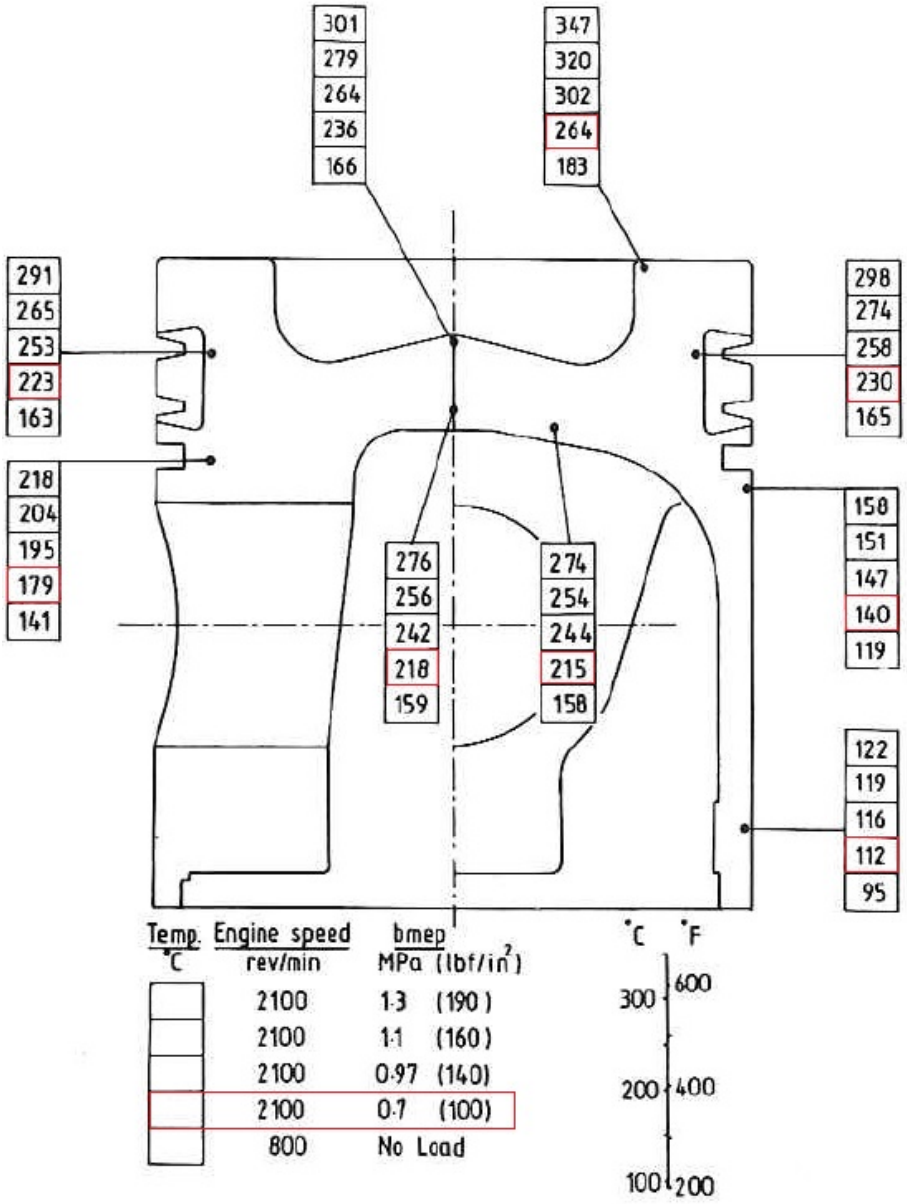

Figure 42: Reference data for piston temperature calibration.[31]

In order to calibrate towards a given temperature field, a selection of points on the piston are chosen for measurement and are then compared with the temperatures of the model in those areas. In this case, the reference data, as shown in Figure 42, is taken from a similar piston running at roughly the same BMEP.

Reference [°C]	**Simulated [°C]**	**Relative difference [%]**
264	198.4	28.37
230	188.1	20.04
140	167	-17.58
112	139.4	-21.79
215	181	17.17
218	181.3	18.32
223	186.3	17.93
179	178.2	0.004

Figure 43: Comparison of initial temperature field and reference.

The initial temperature field is compared with the reference data in Figure 43. With the exception of the temperature at the lower part of the piston skirt, all values have a relatively large error.

Note that the temperature at the "divet" in the middle of the combustion bowl is not chosen for comparison, because the piston modelled in this work has a differently shaped combustion bowl. A divet often reaches very high temperatures, whereas a combustion bowl without this feature might act differently. Another difference is the cast iron inserts for the first two piston rings, which may affect the heat transfer and the temperature gradient over the piston rings.

Lastly it should be noted that the reference engine is running at a higher rpm, which should lead to an increase of the thermal loading.

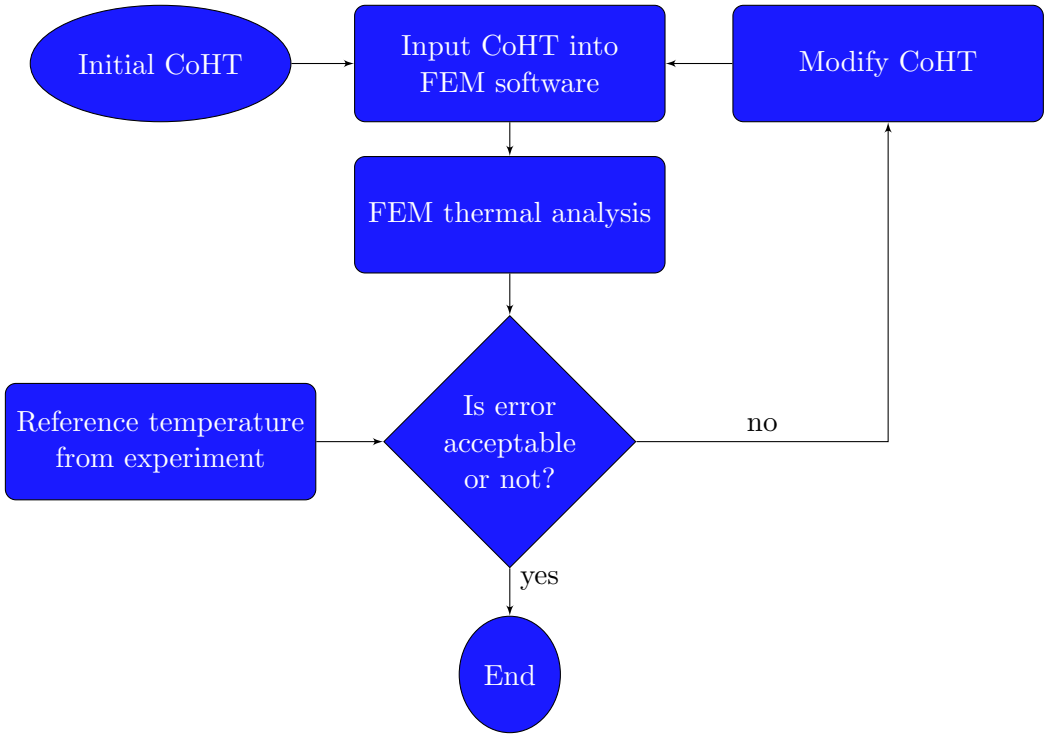

Figure 44: Flow chart for determining the final heat transfer coefficient. [14, 32]

A typical way to calibrate a mode is shown in Figure 44. This approach assumes that the temperature sources and sinks are known, and most of the COHT for the various heat sinks are reasonably estimated and measured. The temperature field is adjusted by changing the values of COHT, mainly the COHT from the combustion. In this case, most of the temperatures are unknown and only a few of the COHT can be said to be reasonable. This leaves things very open, and he temperature field is adjusted mostly by intuition, trial and error.

	COHT[W/m^{2}K]		T[°C]	
(1) Combustion zone	800	Adjusted	365.3	Unchanged
(2) Top land	230	Unchanged	200	Adjusted
(3) Rings	625	Unchanged	72.5	Unchanged
(4) 2^{nd} and 3^{rd} lands	115	Unchanged	72.5	Unchanged
(5) Skirt outside	60	Unchanged	72.5	Unchanged
(6) Skirt inside	162	Unchanged	90	Adjusted
(7) Combustion underside	608	Unchanged	90	Adjusted

Figure 45: Adjusted thermal boundary conditions.

Figure 45 shows the thermal boundary conditions after they have been adjusted. The COHT for the combustion has been significantly increased in order to increase the temperature at the top of the piston. Most likely both the COHT and temperature for the combustion should have been increased, but since neither is known, only one was increased to create a higher temperature. The cylinder wall is the heat sink for the top land. This temperature has been lowered in order to create a more realistic lateral temperature distribution. The underside of the combustion bowl and the piston inside is cooled by splash oil and oil mist. The temperature of the oil sump has been lowered in order to increase the cooling of these parts.

Reference [°C]	**Simulated [°C]**	**Relative difference [%]**
264	235.1	11.58
230	218	5.35
140	183	-26.6
112	145.5	-26
215	209.5	2.6
218	208.8	4.31
223	215.5	3.42
179	209.6	-15.75

Figure 46: Comparison of adjusted temperature field and reference.

A comparison of the new results (Figure 46) show that there is still a significant amount of error involved, in particular at the lower part of the piston skirt and right below the third piston ring. Some of this may be explained by the differences in the pistons, including the higher operating speed and the cast iron insert. However in this work, the aim is to get a representative temperature field rather than an accurate one. The adjusted values are kept in the model.

3.4.6 Adding the mechanical boundary conditions

It is a lot more difficult to find the thermal boundary conditions than it is to simulate them. For the mechanical boundary conditions, the opposite is the case, in particular with respect to the contact interaction. As mentioned in Section 3.2, the mechanical boundary conditions consist of the pressure from the combustion gases and the oscillating forces from the inertia. It was found that the contribution from the oscillating force was small enough to neglect, while the maximum gas force corresponded to a pressure of 75.2 bar. This pressure of 75.2 bar was applied to the piston as a pressure load. The surface chosen for the load was the area subjected to the combustion. This includes the entire lateral area at the top of the piston, and the top land.

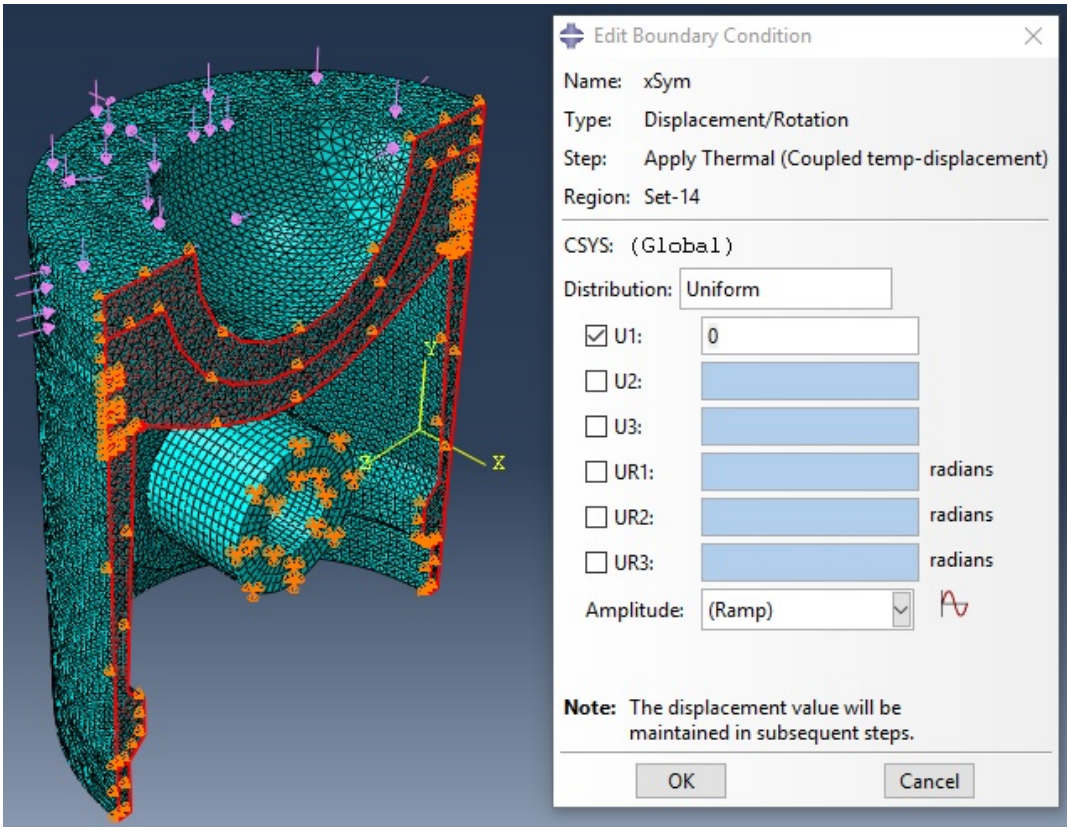

Figure 47: The mechanical boundary conditions.

For reasons of symmetry, only one half of the piston was simulated. If it wasn't for the valve pocket at the top of the piston, a quarter model would've been sufficient. In order to make sure it behaves as if it was a complete piston, a symmetry boundary condition is added. As shown in Figure 47, the piston displacement in the x-direction is locked for the plane of symmetry. This allows the piston to be moved in the y-and z-direction, but it cannot move into the space where the other half of the piston would be.

Figure 47 also shows the piston pin has a boundary condition applied at the plane of symmetry. In reality the piston pin is being held by the small end bearing of the connecting rod, however the size and dimensions of the small end bearing is unknown. In order to get around this issue the piston pin was simply fixed at the plane of symmetry (U1 = U2 = U3 = 0), and due to Saint-Venant's principle, its behaviour at the pin boss area should be equivalent to the real case. If the goal of this work was to study the piston pin, this would not work, however we are only interested in the piston rather than the piston pin.

In order to make the piston pin and the piston pin boss interact properly, a contact boundary condition is applied. The outer surface of the pin and the surface of the pin boss is chosen as a contact pair and has both normal and tangential behaviour is assigned. For the normal behaviour the default "Hard" contact is used, and the contact surfaces are allowed to separate after contact. For the tangential behaviour, the "Penalty" friction formulation is chosen, and the interaction is given a small friction coefficient of 0.1 in order to stabilize the interaction. Comparing with the friction coefficients for other cases, this seems like a reasonable value.[16]

The interaction itself uses the Surface-to-Surface algorithm, and Single-state-tracking is used. The piston pin was chosen to be the master surface and the piston boss was chosen to be the slave surface. Generally speaking the master surface will deform the slave surface, so the more rigid steel pin is chosen for this, while the softer aluminium piston boss is chosen as the slave.

3.4.7 Adding stabilisation

Because the piston boss and the piston pin experiences both thermal expansion and structural deformation, the contact interface between them changes quite significantly, making it difficult for the simulation to converge. In order to stabilize the simulation, automatic stabilization is added to the thermal and mechanical step.

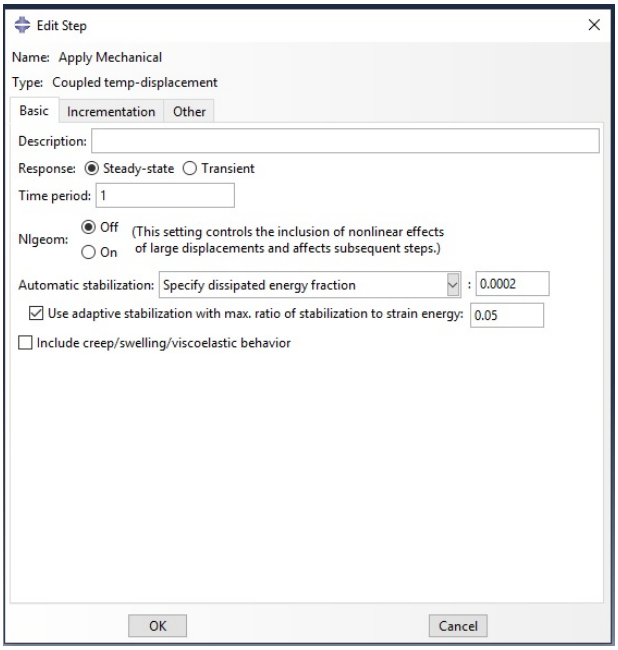

Figure 48: Automatic stabilization.

The default values were kept for the stabilization parameters, as shown in Figure 48. This feature adds a viscous force to the model, creating a damping effect, which stabilized the model. However this may also lead to inaccuracies. In order to verify that the automatic stabilization feature does not affect the outcome, the variables ALLIE and ALLSD must be compared. ALLIE is the total internal energy of the model, and ALLSD is the static dissipation energy used for stabilization for the whole model. If ALLIE is significantly larger than ALLSD, then we may assume that the stabilization does not change the end result of the simulation.[11]

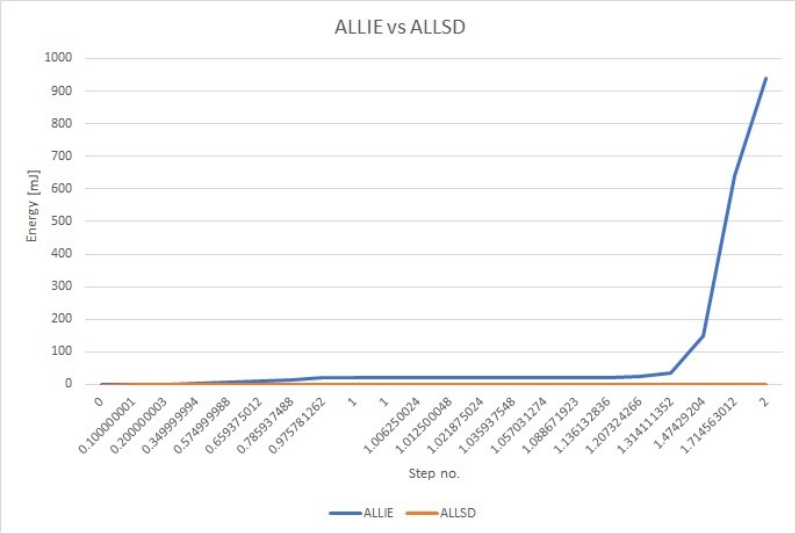

Figure 49: A comparison of ALLIE and ALLSD for the final model.

Looking at Figure 49, it is seen that ALLIE is much greater than ALLSD. Using automatic stabilization to make the simulation run smoother does not interfere noticeably with the end results.

3.4.8 Convergence

The finite element method does not solve a problem exactly, but attempts to approximate the solution. A finer mesh tends to produce a solution closer to the answer - that is, if the model is converging at all. A mesh convergence study looks to answer two things:

- Does the behaviour of the model converge as the mesh is refined?
- If the model converges, which mesh density provides the best compromise between accuracy and computation time?

In order to do a convergence study, the von Mises stress at a chosen node was found for multiple mesh densities. The node was chosen such that its position would be the same for any given mesh density.

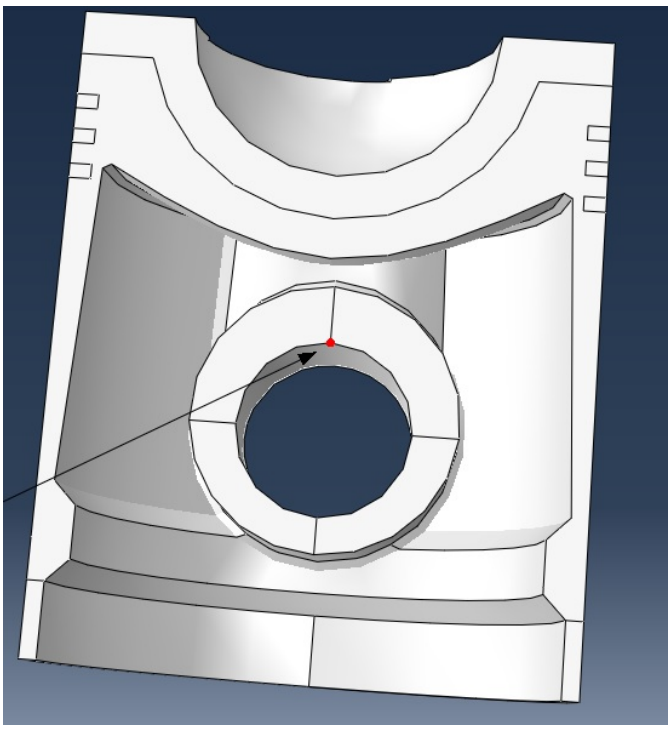

Figure 50: The node chosen to represent the model.

No. elements	**von Mises[MPa]**	**Rel. change[%]**	**Slope[ΔMPa/Δel.]**
8430	120.8		
19581	133.9	10.28	0.00118
42209	156.3	15.43	0.00099
124731	172.3	9.73	0.000194
223780	182.4	5.69	0.000102

Figure 51: Convergence test results from the final model.

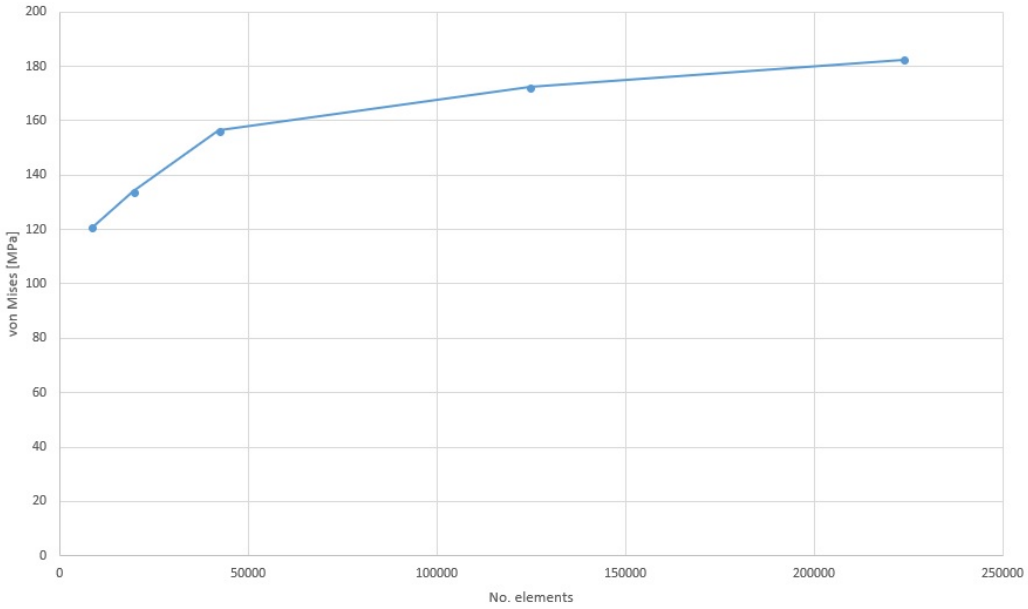

Figure 52: Convergence curve for the final model.

As shown in Figures 50, 51 and 52, the node chosen is converging towards a maximum von Mises stress of just above 180 MPa, with a change of about 5.7% for the last mesh refinement. The model running 223 780 elements takes about 3 hours to run, and offers the highest level of accuracy within the licence limit of about 250 000 elements. Since this study has a relatively low amount of load cases, the mesh with 223 780 elements are chosen, in order to give the most accurate results.

3.4.9 Verifying the final model

In order to verify the final model, the total radial bearing force and the gas force were calculated and compared. The gas force was calculated from Equation 21 and divided by half, since only half of the piston is modelled. The bearing force was calculated from the radial stress distribution in the pin boss.

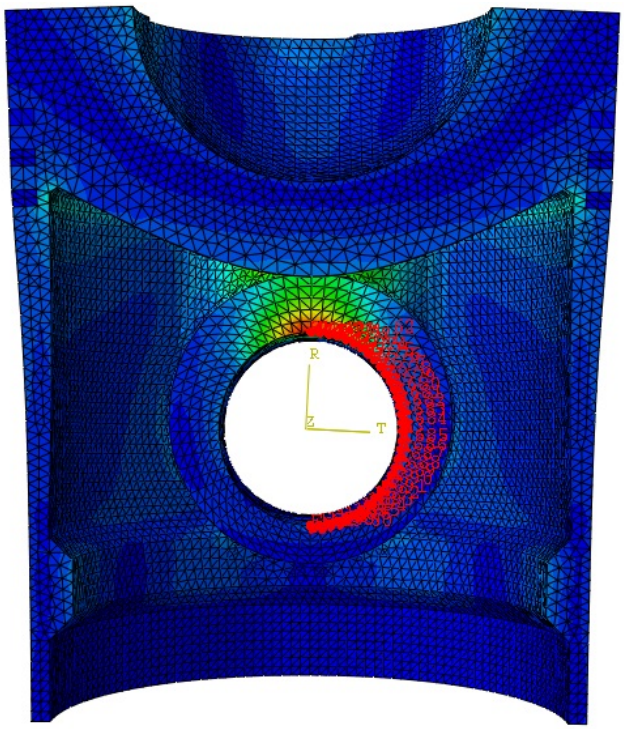

Figure 53: A path around one half of the pin boss.

The bearing force was calculated by creating paths alone one half of the pin boss, as shown in Figure 53, where 0° is the top of the boss. Because the bearing force changes throughout the length of the boss, multiple paths had to be created, starting at the inside of the piston and moving outwards.

Radial stresses may be found from the principal stresses, but to make things easier to keep track of, each path was given its own cylindrical coordinate system with the axial direction pointing away from the centre of the piston. By changing to a cylindrical coordinate system, the stresses S11, S22 and S33 converts to σ_r, σ_θ, and σ_z respectively. The data-pairs for each path was then exported to excel using the plug-ins→Tools→Excel Utilities function.

Once the stresses were stored in excel, they were exported again, this time into matlab. In matlab the stresses were plotted against degrees and boss axial length, as shown in Chapter 4.

In order to calculate the bearing stress in matlab, the trapz() function was used. The trapz() function numerically integrates a function using the trapezoidal method. By default, it numerically integrates in units of 1. In order to adjust the units of integration, the results were multiplied with the length and diagonal of the deformed elements.

These dimensions were found using the Tools→Query→Distance function in Abaqus. The result was a length of 1.578mm in the axial direction, and a diagonal of 1.39mm (the mesh around the pin boss use these diagonals to make a "circle").

```
>> matZrad = [BossNumbersFull{:,2} BossNumbersFull{:,8} BossNumbersFull{:
>> axialAndZ = 1.5478*trapz(matZrad)

axialAndZ =

   1.0e+03 *

  Columns 1 through 14

   -1.4949   -1.2248   -1.0464   -0.8873   -0.8029   -0.7329   -0.6673

  Column 15

   -0.0028

>> Integratedfully = 1.39*trapz(axialAndZ)

Integratedfully =

  -1.1006e+04

>> Bossforce = 2 * Integratedfully

Bossforce =

  -2.2012e+04

>> GasForce = 0.5 * (87^2)*pi*0.25 *7.52

GasForce =

   2.2352e+04

>> RelativeDifference = (GasForce+Bossforce)/(0.5*(GasForce-Bossforce))

RelativeDifference =

    0.0153
```

Figure 54: Matlab code used to verify the model.

Figure 54 shows the code used to calculate the total bearing force. The bearing force is doubled due to the dataset only including half of one piston boss. The gas force is halved due to the model containing only half of a piston. The relative difference between the calculated gas force and the simulated bearing force is roughly 1.53%.

4 Results

4.1 General behaviour of the model

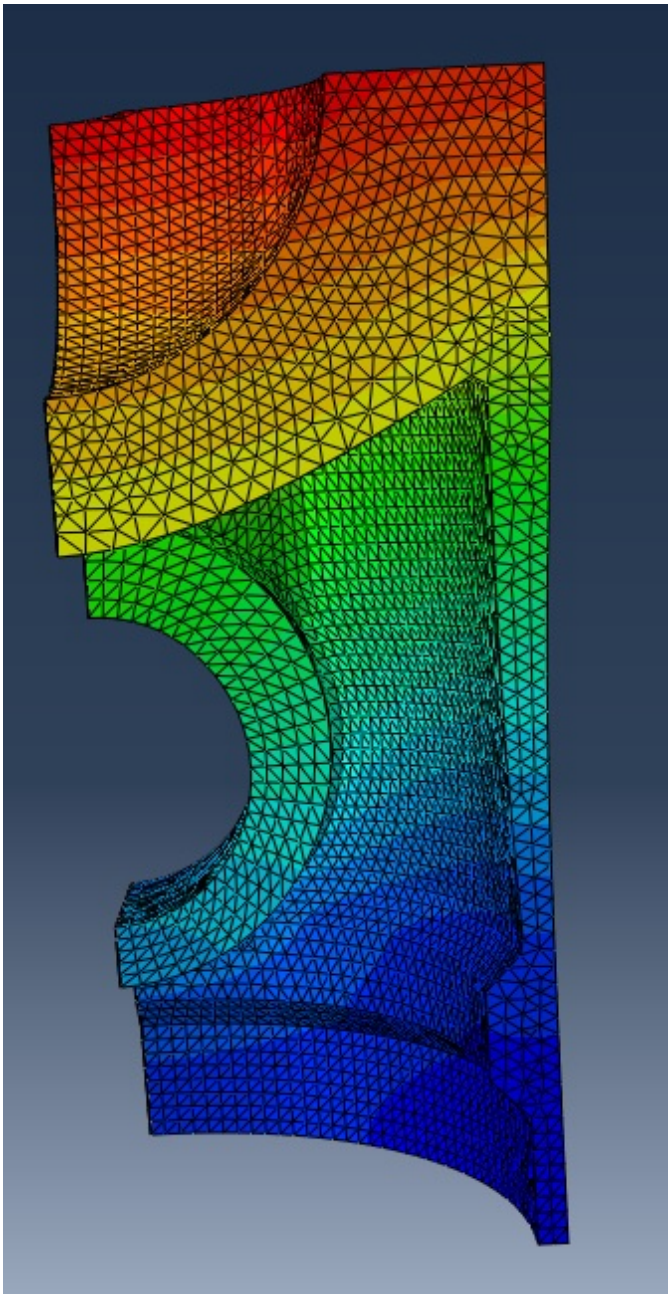

Figure 55: The temperature field of the piston.

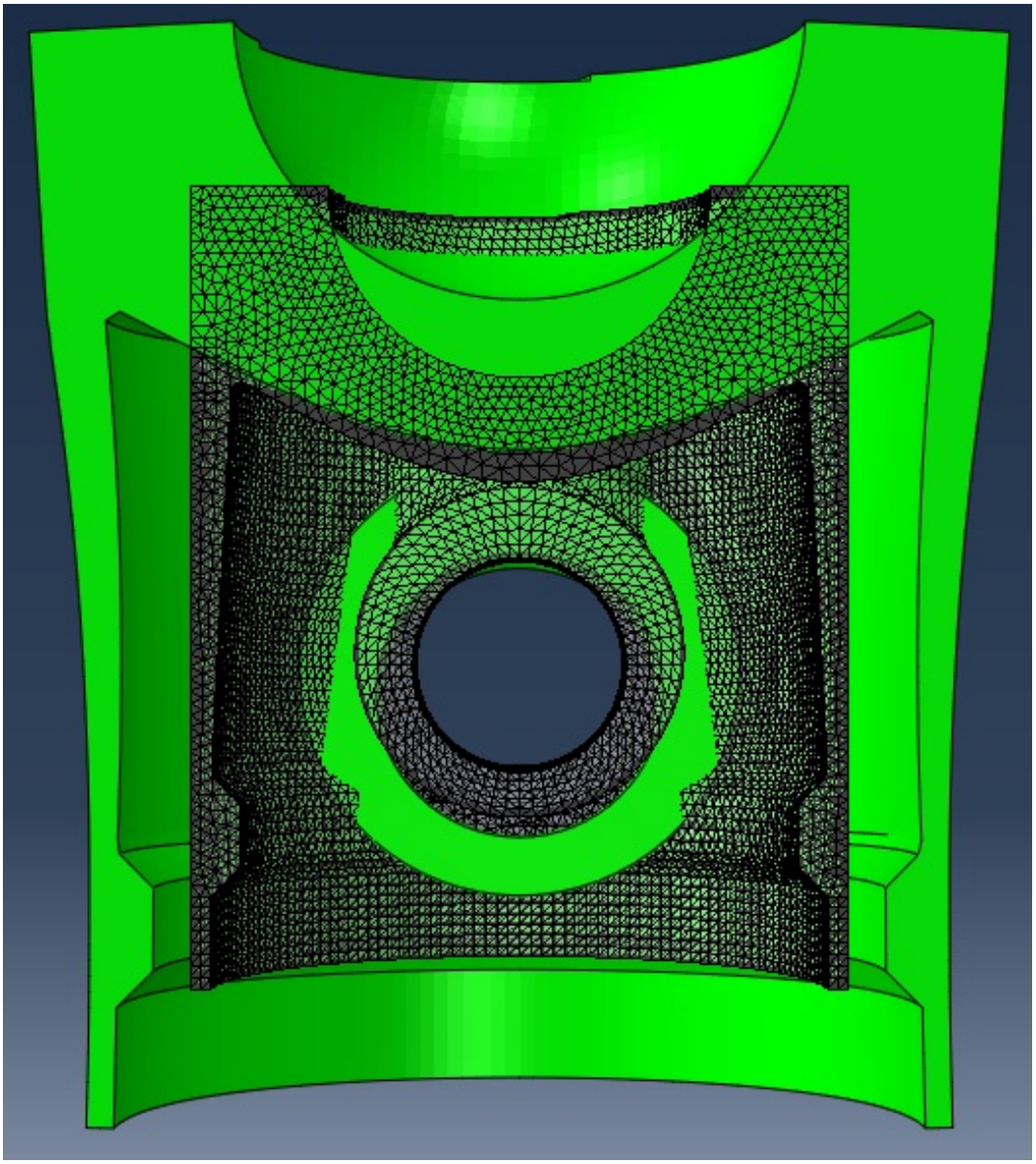

Figure 56: Deformation of the piston due to thermal loading, scaled up by a factor of 100.

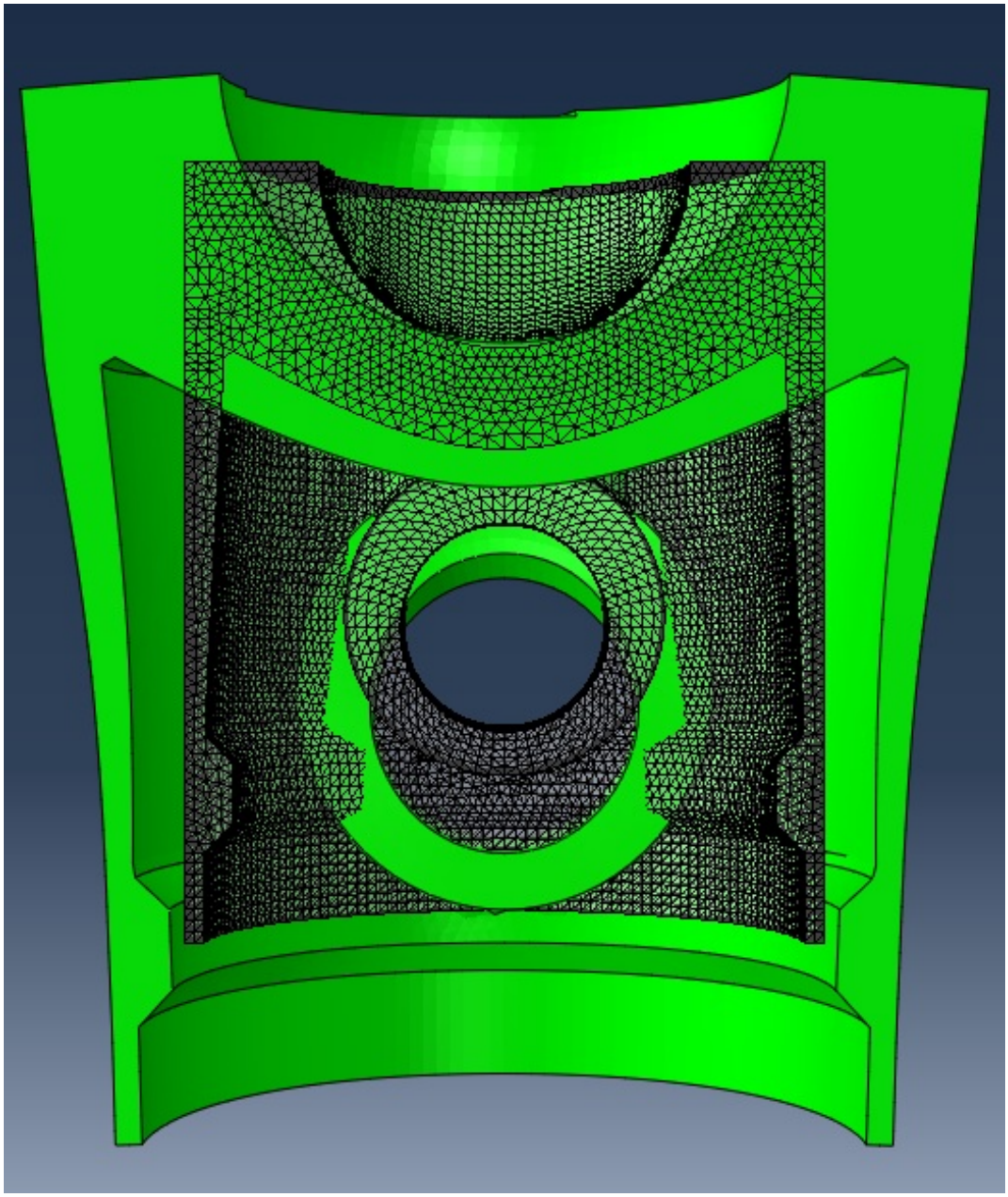

Figure 57: Deformation of the piston due to thermal and mechanical loading, scaled up by a factor of 100.

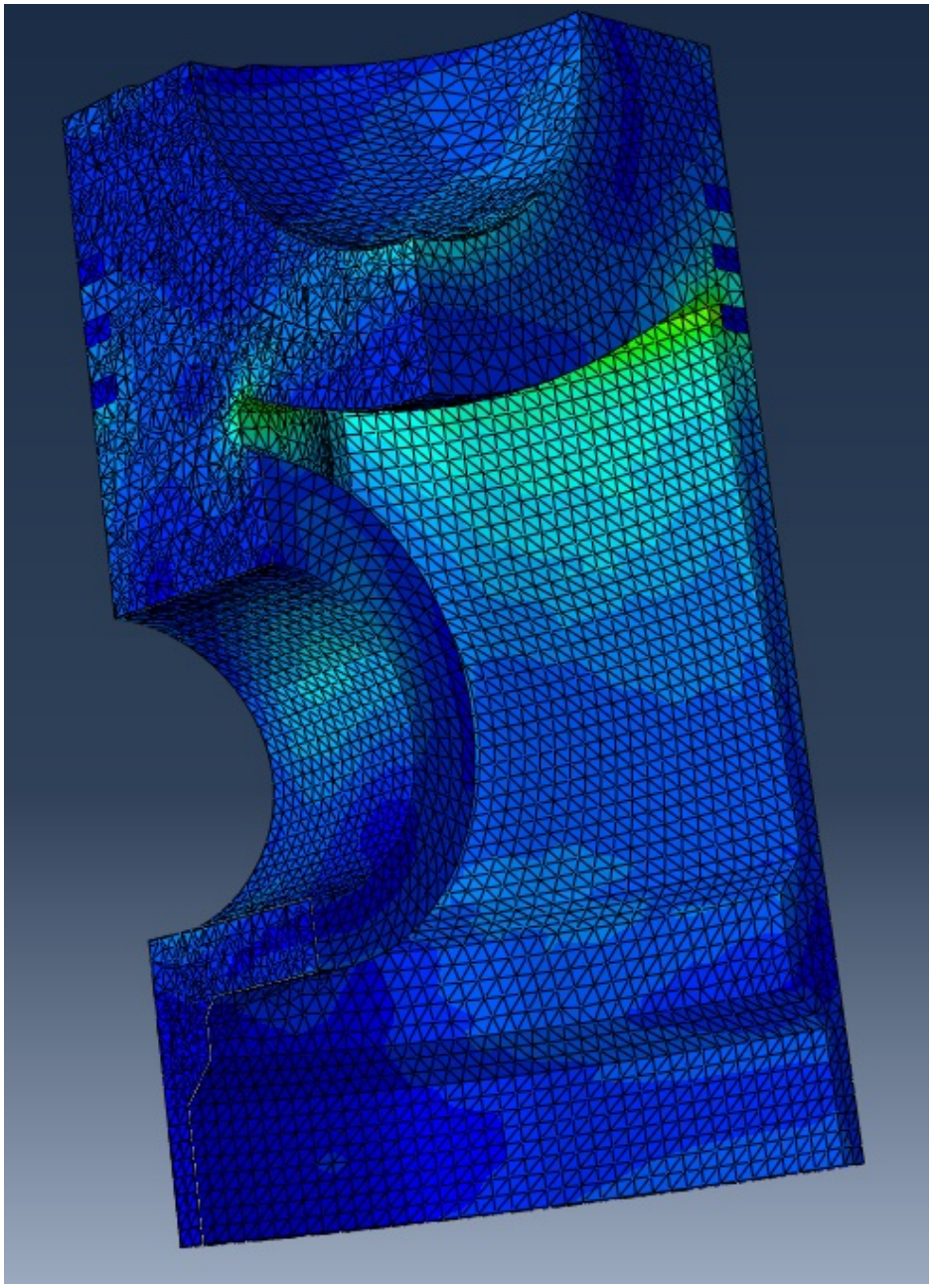

Figure 58: von Mises stress [MPa] in one quarter of the piston due to thermal loading.

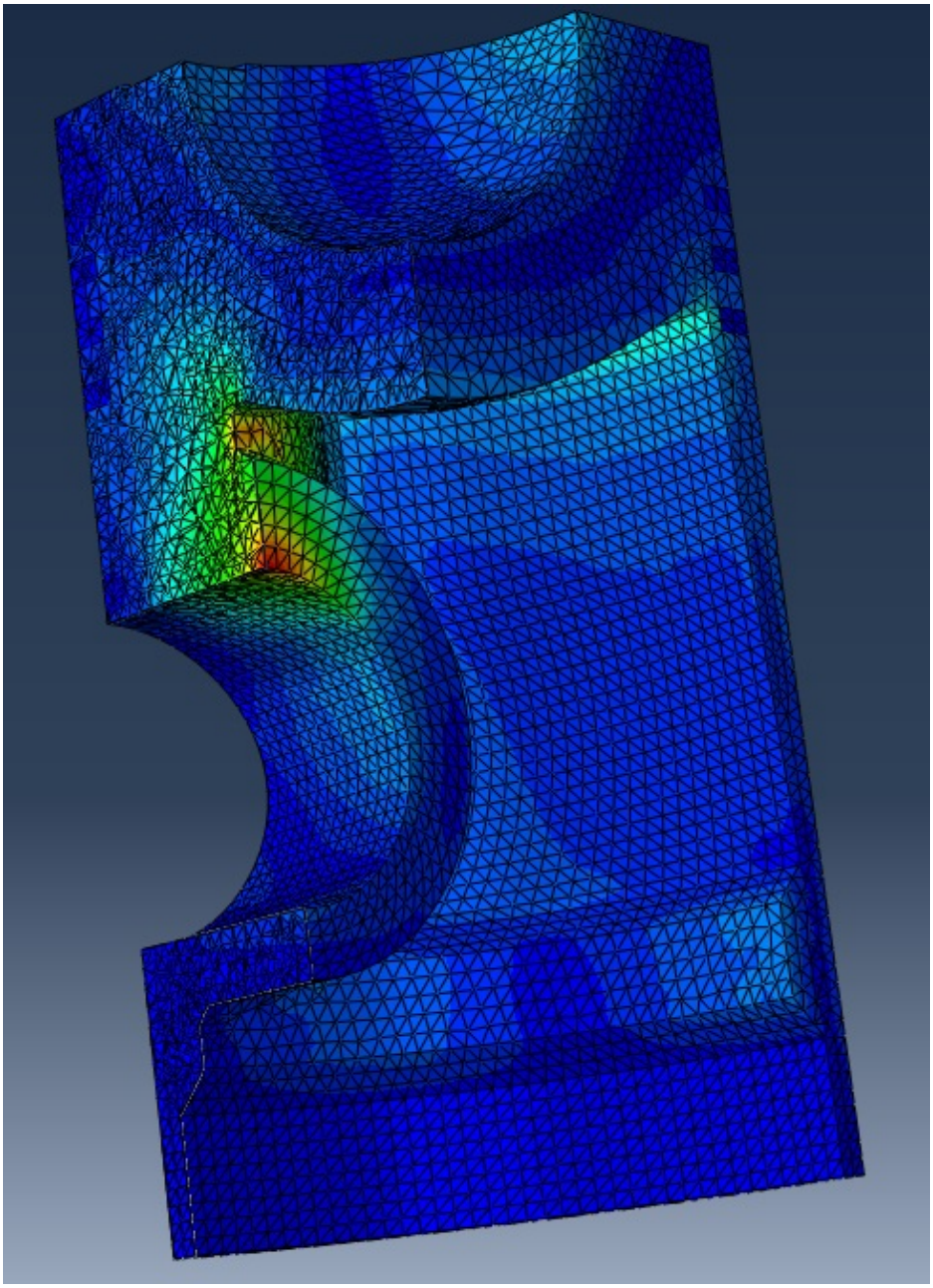

Figure 59: von Mises stress [MPa] in one quarter of the piston due to thermal and mechanical loading.

4.1.1 The pin boss

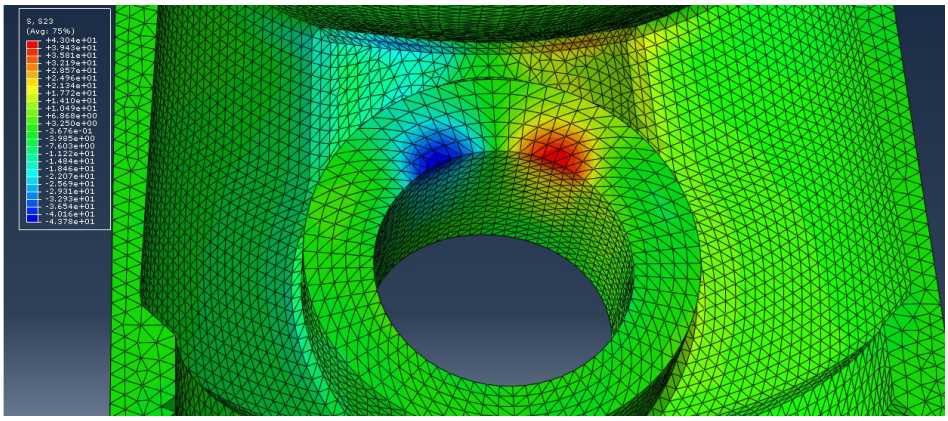

Figure 60: Shearing in the pin boss [MPa], in the plane normal to the boss centre axis.

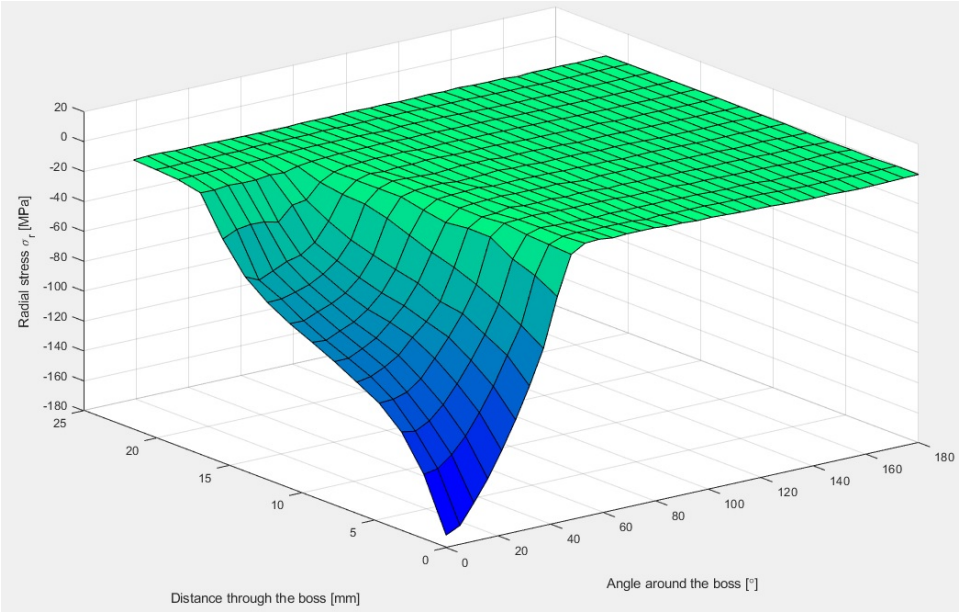

Figure 61: Radial stress distribution throughout the boss during full thermal and mechanical load. 0° is the top of the boss, and 0 mm is at the inside of the piston.

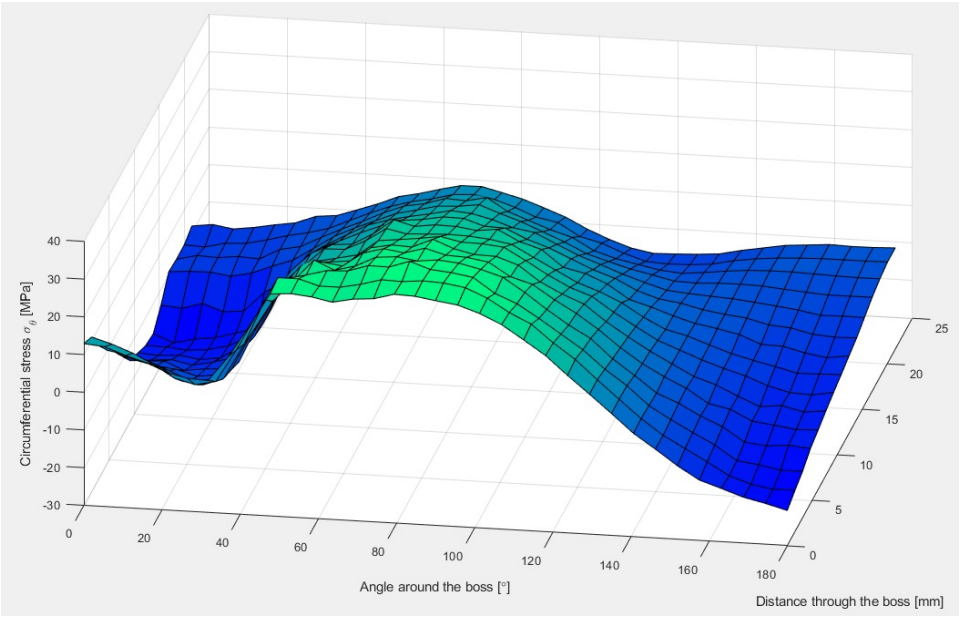

Figure 62: Circumferential stress distribution throughout the boss during full thermal and mechanical load. 0° is the top of the boss, and 0 mm is at the inside of the piston.

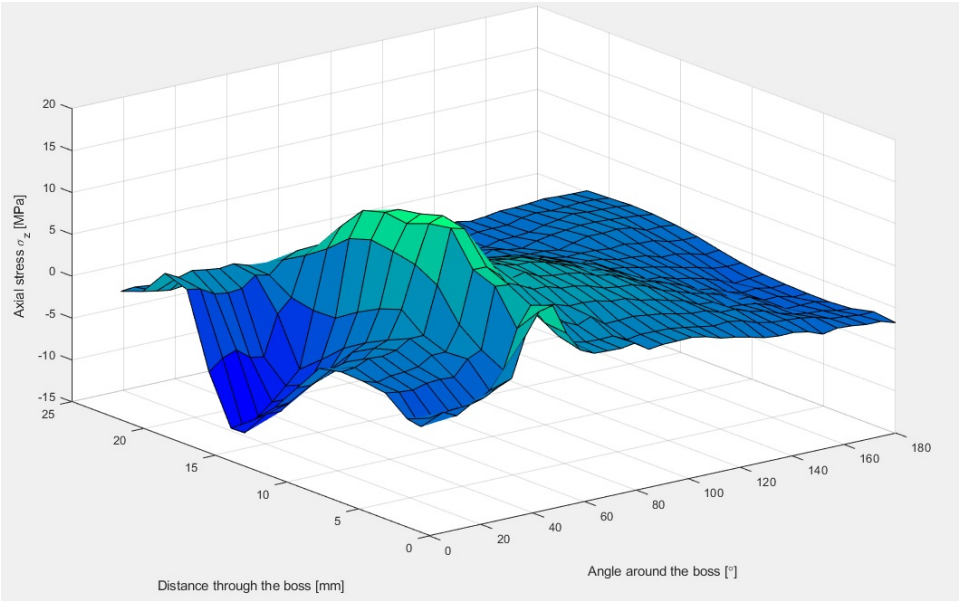

Figure 63: Axial stress distribution throughout the boss during full thermal and mechanical load. 0° is the top of the boss, and 0 mm is at the inside of the piston The positive axial direction is outwards from the centre of the piston.

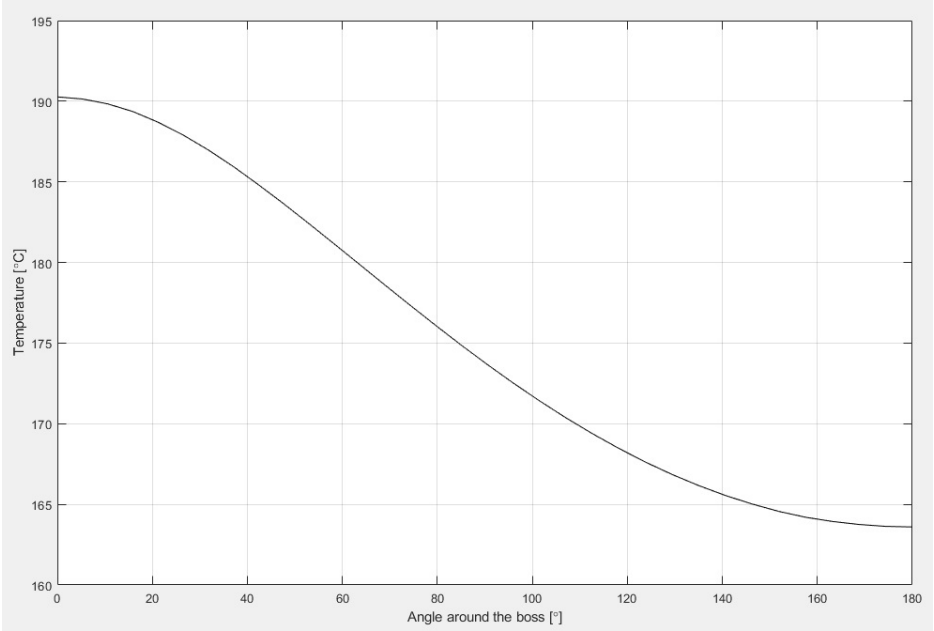

Figure 64: Temperature around the boss surface, starting from the top.

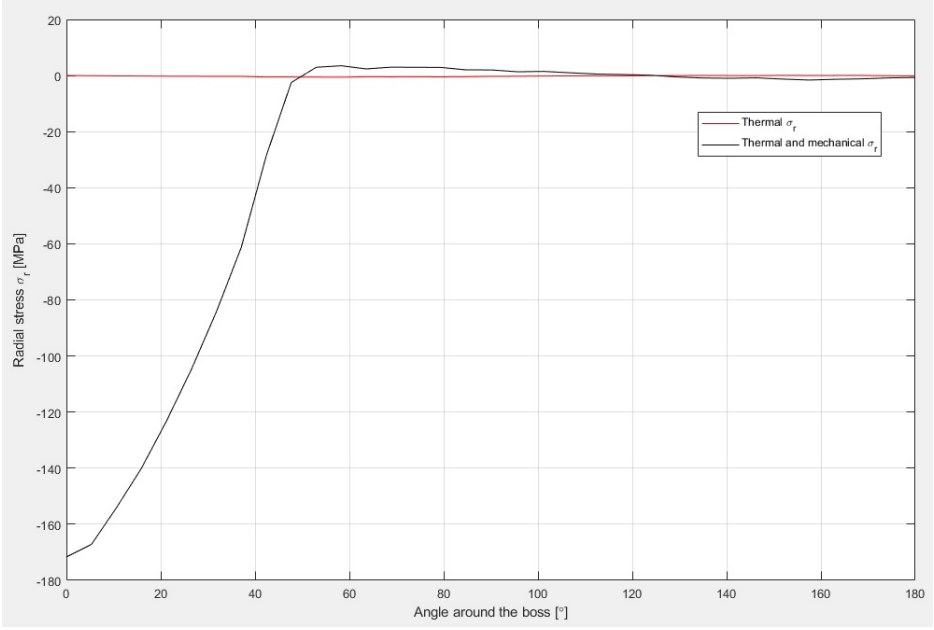

Figure 65: Radial stress around the boss surface, starting from the top.

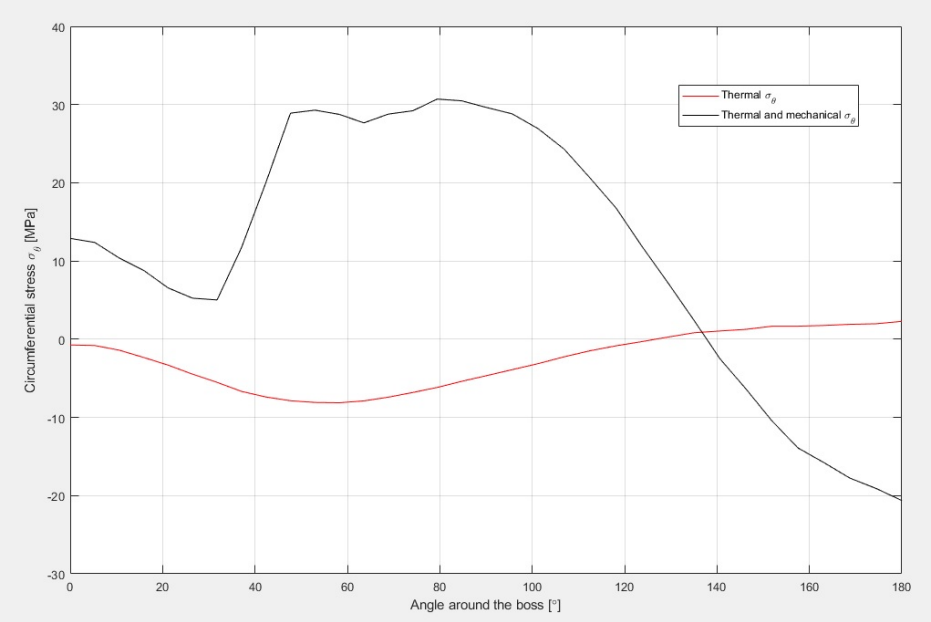

Figure 66: Circumferential stress around the boss surface, starting from the top.

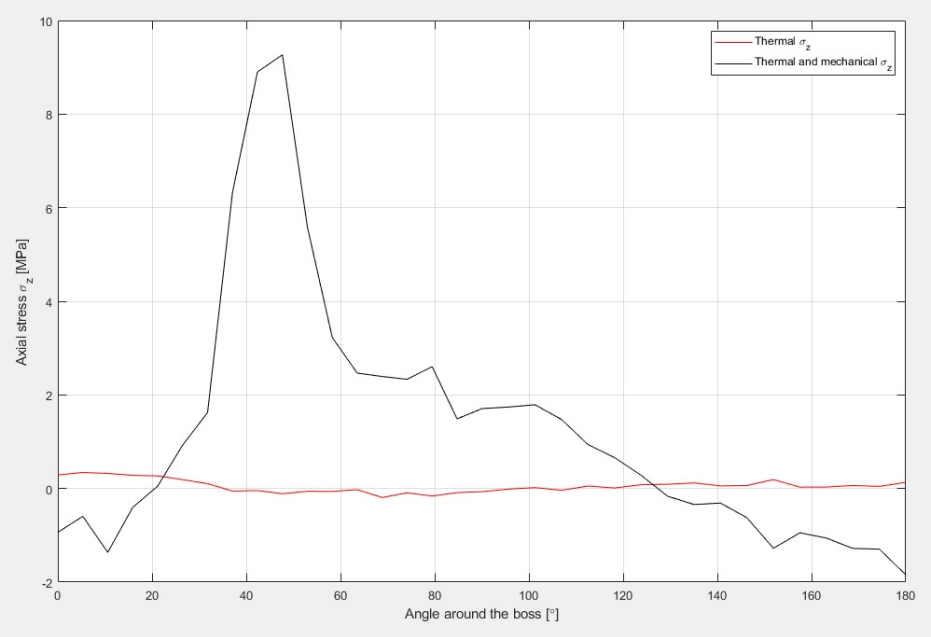

Figure 67: Axial stress around the boss, starting from the top.

4.1.2 The combustion bowl rim

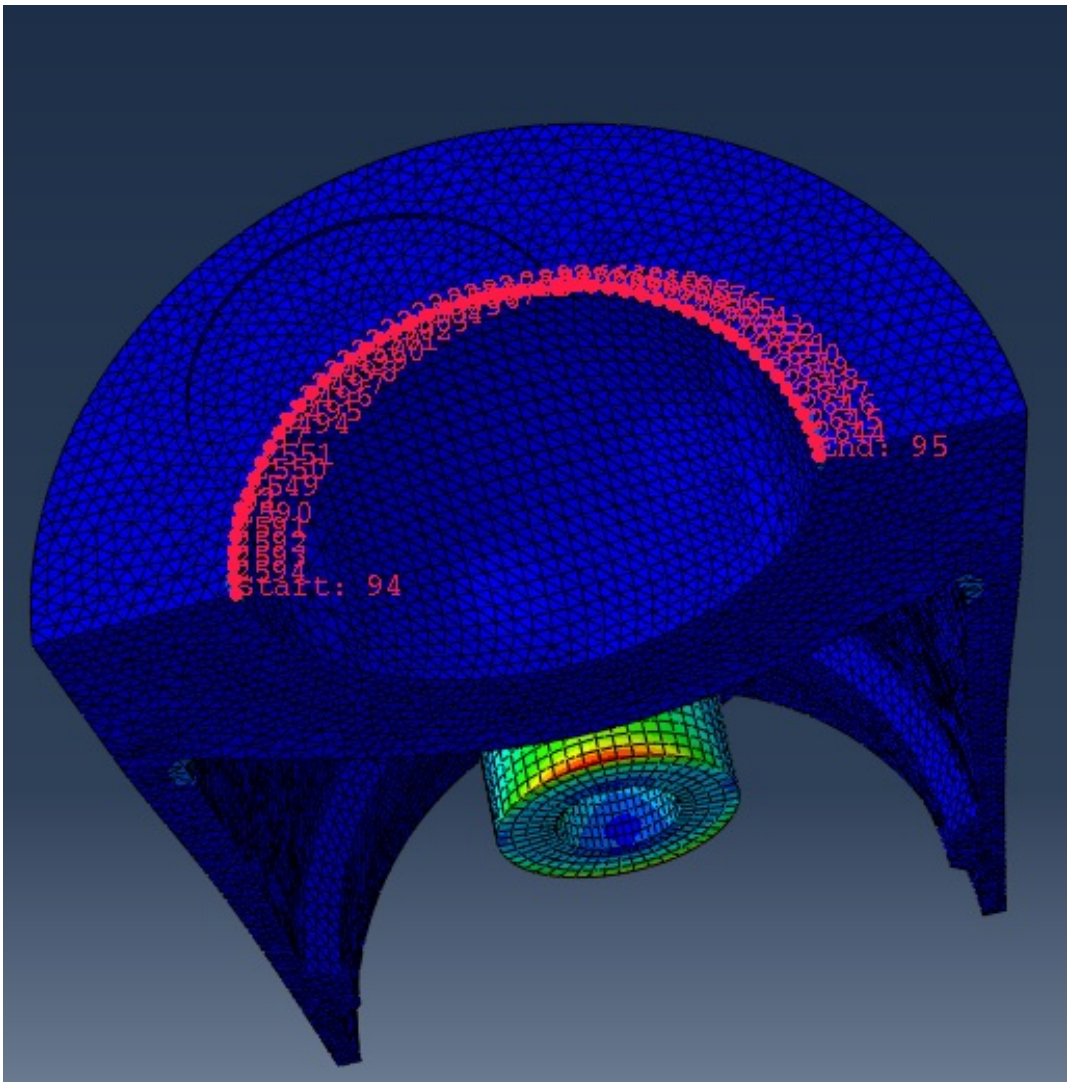

Figure 68: The path along the combustion bowl rim.

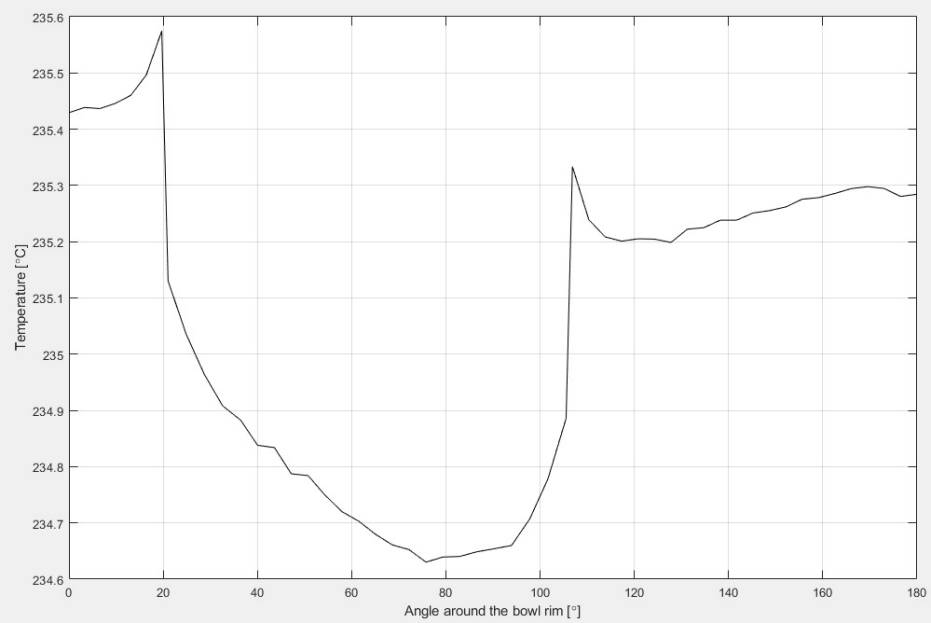

Figure 69: Temperature around the bowl rim, the pin plane is at 90°.

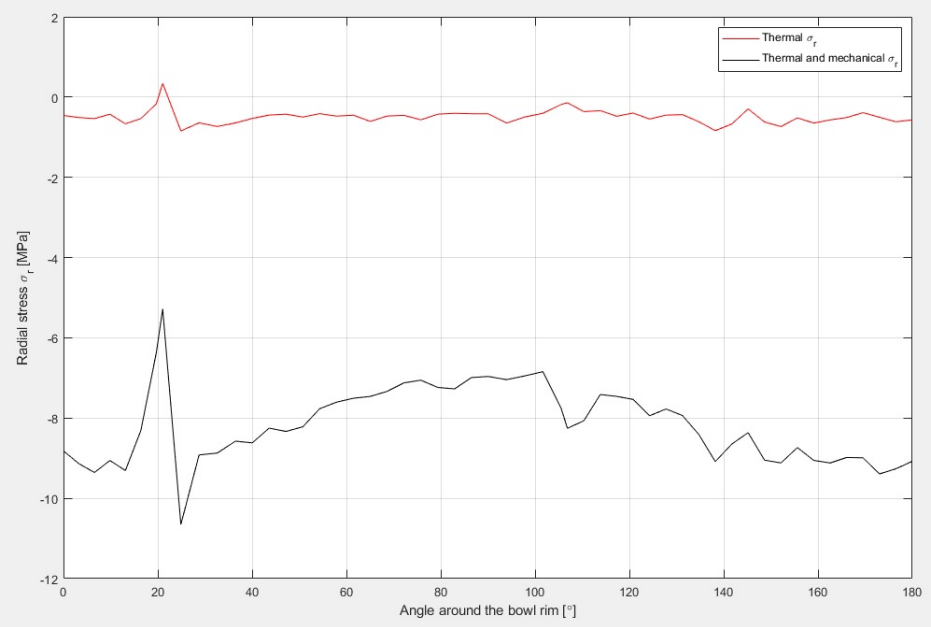

Figure 70: Radial stress around the bowl rim, the pin plane is at 90°.

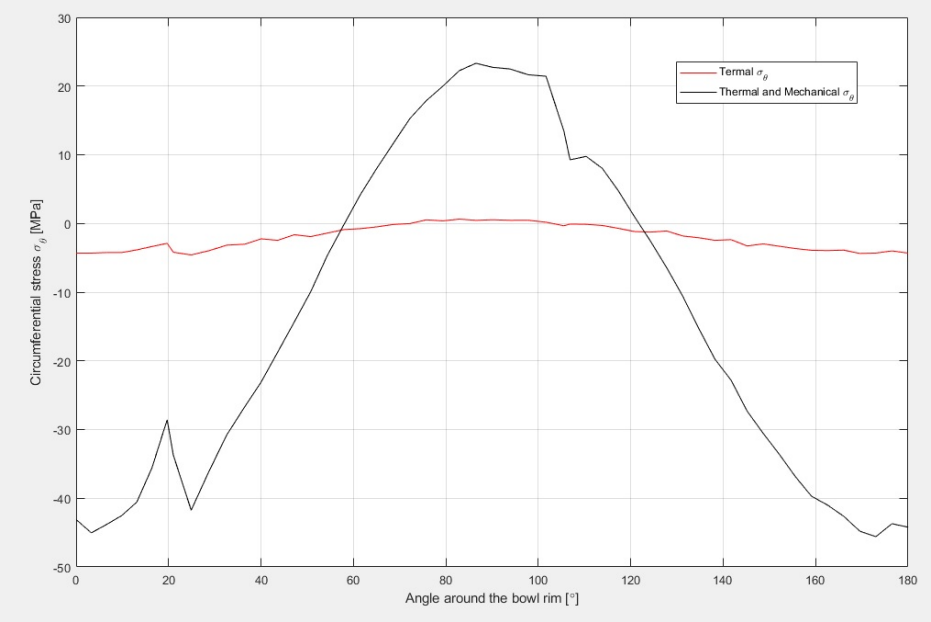

Figure 71: Circumferential stress around the bowl rim, the pin plane is at 90°.

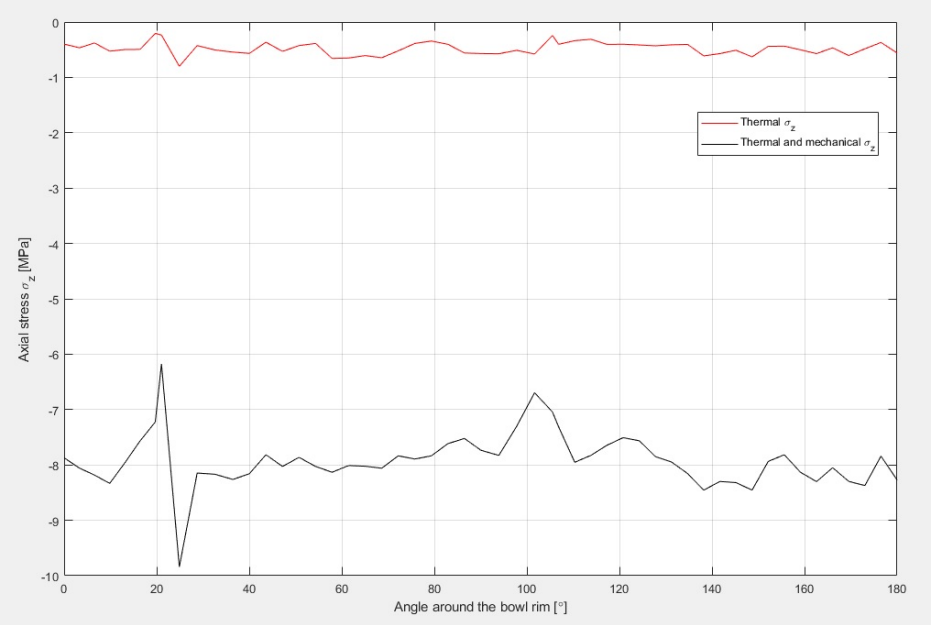

Figure 72: Axial stress around the bowl rim, the pin plane is at 90°. The positive axial direction is upwards.

4.2 Fatigue analysis

Fatigue cracks are most likely to begin at the points with the highest maximum principal stress[28, 20], which is equivalent to the points of maximum tensile circumferential stress. These points at the piston boss and bowl rim were chosen for the fatigue analysis. The local temperature was found, and the mean and alternating stress between thermal load and combined thermal and mechanical load was calculated. The results were compared in a Gerber-parabola. The fatigue strength σ_{bw} and tensile strength was found in Appendix A, and linear extrapolation was used to calculate σ_{bw} and tensile strength for the local temperatures.

$\sigma_{\theta,max}$	30.7020 MPa
$\sigma_{\theta,min}$	-6.1654 MPa
T	176.1435 °C
$\Delta\sigma$	36.8675 MPa
σ_m	12.2683 MPa
σ_a	18.4337 MPa

Figure 73: Piston pin boss fatigue calculation.

$\sigma_{\theta,max}$	23.3171 MPa
$\sigma_{\theta,min}$	0.4497 MPa
T	234.6485 °C
$\Delta\sigma$	22.867 MPa
σ_m	11.8834 MPa
σ_a	11.4337 MPa

Figure 74: Bowl rim fatigue calculation.

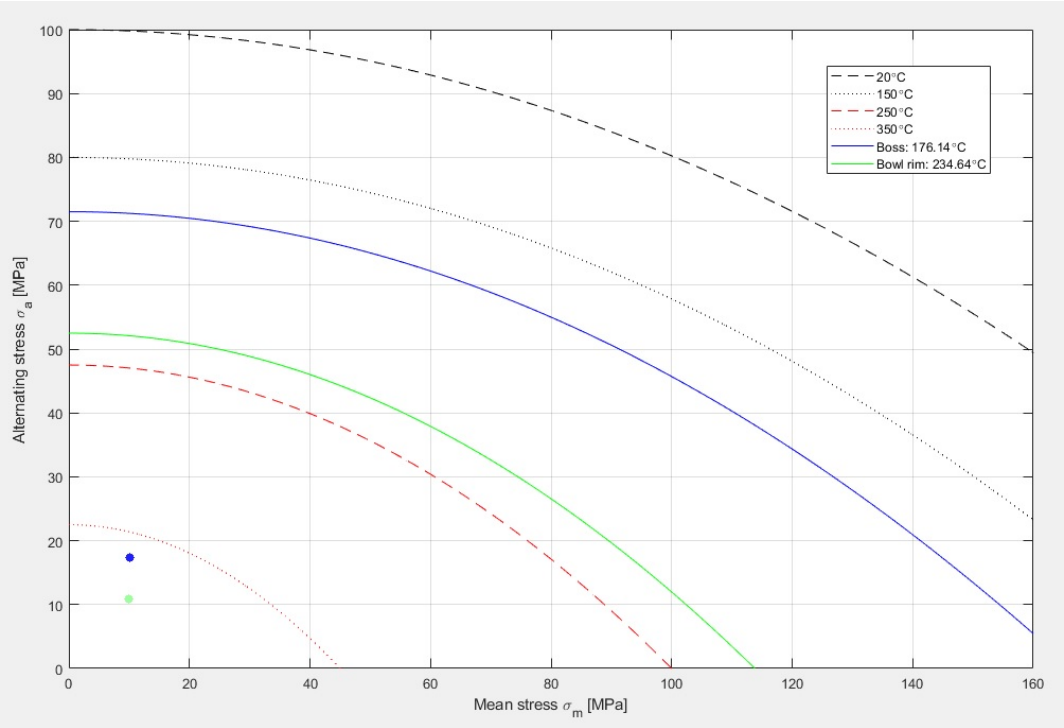

Figure 75: Comparison of stresses to fatigue strength.

5 Discussion

5.1 General behaviour of the model

While the thermal and mechanical behaviour of diesel engine pistons have been studied both experimentally and theoretically for a long time, most work seem to focus on specifics rather than the piston as a whole. Therefore the piston will be described in some detail in this chapter. This is intended to serve as a case study for future work, while also being an introduction to the fatigue analysis in this work.

Figure 55 shows the temperature field for one quarter of the piston. The piston has multiple temperature gradients, most notably a vertical gradient and a lateral gradient on each side of the bowl rim. The highest temperatures are found in the bowl rim, while the lowest are found in the lower part of the piston skirt, in the skirt plane. The boss side seem to have higher temperatures than the skirt side. Recall that the temperature field is representative for a typical piston and may not be accurate for this specific piston. This is mainly because the amount of experimental data required to calibrate the temperature field of the model was a lot higher than initially expected.

By looking at Figure 56 and 57, a general understanding of how the piston expands and deforms can be gained. Figure 56 shows the effect of the thermal loading on the piston. The expansion outwards is greater at the top, and decreases further down. Considering that the temperature is also greater towards the top, this makes sense. The piston boss expands in size, and changes the fit between the pin and boss from a snug fit to a clearance fit. When looking at the combined mechanical and thermal loading in Figure 57, we see that the piston deforms further under the stress of the gas force, and deforms itself around the piston pin. The piston boss becomes ovalised due to the piston being pushed down on the piston pin. There is also a small amount of pin bending, causing the whole piston to move downwards slightly.

Figures 58 and 59 shows the von Mises stress in one quarter of the piston. In Figure 58 we see the von Mises stress under thermal load, and it is obvious that the greatest stresses occur at the chamfers underneath the piston crown due to thermal expansion. The chamfer near the skirt side plane, right behind the third piston ring, has slightly greater thermal stress than the chamfer near the pin side plane. This is most likely due to the thin piston wall in this region.

By looking at Figure 59, where both the thermal and mechanical loading is applied, stresses have increased in the two points where the bowl rim crosses the pin side plane and the skirt side plane. This is due to the piston folding itself over the piston pin. Generally speaking this will create tensile stresses in the pin plane and compressive stresses in the skirt plane. The most stressed points are no longer the chamfers, but the edge of the piston pin boss, and to a lesser extent the reinforcement above the pin boss.

From this we see that the areas of interest are the bowl rim, the boss, the support for the boss, and the chamfers. Considering that the highest stresses occur in the boss, and the material weakening due to temperature is highest at the bowl rim, these two areas are studied closer.

It is important to remember that the bowl rim is modelled with optimistic conditions, and the pin boss with pessimistic ones. In reality the bowl rim would also be exposed to high temperature creep and pitting. As the engine turns on and off or changes load conditions, the temperature field would change and induce low-cycle thermal fatigue. These effects are not accounted for in this simulation.

The pin boss on the other hand, would be coated in an oil film, which would act as a "cushion" and help distribute the stresses between the pin boss and the piston pin. In reality the peak stresses in the piston boss could be expected to be a bit lower than the prediction of the model. According to the paper by KS, the point of maximum stress for dry contact is at the inner face, which corresponds well with the results. However the effects of lubrication tend to move this point of maximum principal stress slightly inward through the boss.

In short, the predicted strength of the bowl rim should be taken as a lower limit, while the predicted strength of the pin boss should be taken as an upper limit.

5.1.1 The pin boss

An important feature of the stress in the piston pin boss is shown in Figure 60. This is the shear stress in the YZ-plane (the plane of symmetry for the piston model). The shear stress has two peaks at the edge of the piston boss, one in the positive (right) direction and one in the negative (left) direction. This shows that the boss is subject to heavy shearing in these regions.

Figures 61, 62 and 63 shows the radial, circumferential and axial stresses throughout the boss surface for one half of the boss (as shown in Figure 53) during thermal and mechanical load. The angle of the top of the boss is 0°, while the axial direction is defined outwards from the centre of the piston, making 0 mm start at the edge of the inner face of the boss surface.

Studying the plot for the radial stress throughout the boss, we see that the compressive radial stress increases closer to 0° and closer to the inside face of the boss. Along the axis for the angle, the stress goes to zero between 40° and 60°. This corresponds well with earlier work on pin-loaded tubes and pin-loaded lugs.[27, 28] Along the axis for the distance through the boss, the stress goes to zero at just above 15 mm, which makes sense considering the piston pin is not long enough to go through the entire boss, and stops at about 15.45 mm.

Figure 62 for the circumferential stresses throughout the piston boss, shows that the peak tensile stresses occur near the inner face of the boss, at roughly 80° although it changes throughout the boss. Generally speaking, the circumferential stress around the surface of a clearance fit will be compressive near the top, due to the bore "folding" itself over the pin. Due to ovalisation, there will also be a tensile peak at the middle, and compression towards the bottom. The maximum compressive hoop stress is usually located at 180°, while the peak tensile stress is located around 39° for a clearance fit, and around 84° for a snug fit.[27, 28] The piston boss corresponds well to this behaviour at a certain distance into the bore, but close to the inside face, near the top (close to (0°, 0 mm)) is tensile, while a clearance fit would normally be in compression in this region. This anomaly will be addressed later.

Figure 63 shows the axial stress throughout the piston boss, where the positive direction is outwards; away from the centre of the piston. There is a positive peak just after 60°, indicating that the boss surface is being pushed outwards in this region. This may be due to the pin and the piston boss bending, and creating lateral forces. There is also a notable negative peak near the top (0°), roughly at the distance where the pin ends (15 mm). This might be because the edge of the pin meeting the boss surface creates an edge-effect.

The temperature as well as radial, circumferential and axial stress around one half of the piston boss at the inner face (distance = 0 mm) is shown in Figures 64, 65, 66 and 67. Stresses from both thermal and combined thermal and mechanical loading is plotted for comparison. The plot starts at the top of the boss at 0° and moves around the edge to the bottom at 180°. Looking at Figure 64 There is roughly a 25°C temperature difference from 0° to 180°.

Looking at the radial stress in Figure 65, the thermal stress is negligible, and the mechanical stress is dominating. With the mechanical stress applied, the radial stress approaches zero at roughly 45°, indicating that the pin is no longer in contact with the boss beyond this point. As expected, the maximum compressive stress occurs at the top of the boss.

Looking at the circumferential stresses in Figure 66, we see that the thermal stress is slightly compressive from 0° to about 120°. This is likely due to the various thermal gradients in the boss. The temperature difference between the top and bottom of the boss indicates that the level of thermal expansion will be different. Also, the outside of the boss is cooled by oil splash, while the inside of the boss is not. The results in the boss inside surface having a slightly higher temperature than its outside. Thus the boss inside surface tries to expand more, and becomes compressed by its surroundings.

The thermal and mechanical loading causes the characteristic tensile peak around 90°, before going into compression at about 135°. The points containing the maximum ten-

sile stresses alternate between a slightly compressive stress during thermal load and a tensile stress of about 30 MPa during the combined load. There is a smaller tensile peak going from 0° to about 25°, containing the anomaly.

The presence of edge-effects in three-dimensional simulations has been investigated earlier and it has been shown that at the edge of a pin-loaded lug, there will be a sharp raise in stress. However for a clearance fit the circumferential stress around the edge should still be compressive.[27] The edge-effect only appears for a short section of the bore, and further mesh refinement in this area may have shown its behaviour more clearly. The edge-effect it present in newer works such as the examples in the Mahle book on piston design[5], but seem absent in older studies of the pin boss.[31]

The most reasonable explanation for the tensile peak is because of the aforementioned shearing (Figure 60), where the material is being pushed away from the top of the boss. While this tensile peak is not the most critical area of the boss, it seem to be subject to fatigue failure.[30] The reason for this might be because the peak is directly below the point of maximum circumferential tension on the combustion bowl rim, and cracks tend to propagate from one to the other.

Looking at the axial stress in Figure 67, the thermal stress is roughly equal to zero. A peak of about 9 MPa occurs at about 50°, just before the point where the pin is no longer in contact with the boss surface.

5.1.2 The combustion bowl rim

The path along the bowl rim is shown in Figure 68. The temperature as well as radial, circumferential and axial stress along the combustion bowl rim is plotted in Figures 69, 70, 71 and 72. Stresses from both thermal loading and combined thermal and mechanical loading are plotted together for comparison. The plot starts at 0° at the point where the bowl rim crosses the skirt plane, and goes along one half of the piston. The point of the bowl rim that crosses the pin plane is at 90°. The change in temperature is less than 1°C, but the part of the bowl rim containing the valve pocket is shown clearly from Figure 69.

Looking at Figure 70 the radial stresses along the bowl rim are close to zero, but slightly compressive under thermal load. This appear to happen because there being negative temperature gradients on both sides of the bowl rim. The material at the bowl rim expands more than its surroundings, and is being compressed.

During combined thermal and mechanical loading, the radial stresses along the bowl rim becomes increasingly compressive. This could be explained by looking at the areas affected by the gas pressure. The top land and the combustion bowl are both affected by lateral forces from the pressure, which would push on the bowl rim from both side, compressing it.

Figure 71 shows the circumferential stresses along the bowl rim. Fatigue cracks are most likely to initiate at the points of peak tensile circumferential stress, which in this case is quite close to 90°. The valve pocket is noticeably acting as a stress-raiser but not in the vicinity of the peak tensile stress. The points containing the maximum tensile stress seem to alternate between roughly 0 MPa during the thermal stress, to just above 20 MPa during the combined load.

Figure 72 shows the axial stress on the bowl rim, the positive axial direction being upwards from the top of the piston. Its behaviour is very similar to that of the radial stress, for obvious reasons, and the same arguments can be used to explain its behaviour.

5.2 Fatigue analysis

Looking at the results in Figure 75, it is evident that the piston is in no danger of fatigue failure earlier than expected. Both the piston boss and bowl rim appear to perform well below the local fatigue strength of the material. The temperature effect on the fatigue strength is evident, and the Gerber-parabola is much stricter for the bowl rim than the pin boss. On the other hand, the alternating stress in the pin boss is noticeably higher than for the bowl rim. The mean stresses are roughly the same because the pin boss is cycling from tension to compression, which reduces the mean stress, while the cyclical stress on the bowl rim is always in tension.

The stresses appear to be very conservative, especially considering this is an upper estimate for the pin boss stress. It is important to note that while the model does converge, there is still a slight increase in stress with mesh refinement, even at this mesh density. Due to this the fully converged results may be slightly higher than the results given. It is also important to consider that this is a simple and relatively "safe" piston, intended for a long lifetime.

Looking at the numbers, the piston is subjected to one load cycle per two revolutions of the engine, when operating at a speed of 1500 rpm. The expected lifetime of a piston at the fatigue strength is then $(5\text{x}10^8)/((1500\,\text{rpm}/2)\text{x}(60\,\text{min})) = 11111.11$ hours. This is assuming the fatigue strength data is measured for $N = 5\text{x}10^8$, the typical number of cycles for aluminium. The time between service intervals for a piston for this engine is given as 2000 h. All this considered, the piston is more than safe in its current state, although Figure 75 shows that the temperature has a significant impact on the fatigue strength, and running the engine at higher rpm would also decrease the lifetime.

It is also important to mention that increasing or changing the temperatures will most likely change the behaviour of the piston somewhat, due to the temperature dependency of the material. Increasing the thermal load may also increase the maximum circumferential stresses. That being said, the local fatigue limit for the pin boss is about 70 N/mm^2 which corresponds nicely with the recommended limits of 65-69 N/mm^2.[8, 12]

In order to find an exact compromise between lifetime and thermal load, software such as nCode DesignLife can be used to estimate SN-curves for lifetime N. Unfortunately, this software is not available, nor is experimental data of temperature dependant SN-curves for the material. This is recommended for further work.

6 Conclusion

Dimensions for a diesel engine piston was measured, the thermal and mechanical boundary conditions were estimated and a FEM-model was created for thermomechanical analysis. The general behaviour of the piston was explained in some detail, and potential areas for fatigue cracks was investigated. The most critical areas was determined to be at the pin boss and the bowl rim, while the boss reinforcements and bowl underside are also vulnerable areas for fatigue cracks.

The requirements to properly estimate the thermal loading were higher than initially anticipated, and required extensive information about the engine, experimental data as well as in-depth knowledge about empirical formulas used to calculate the proper thermal boundary conditions. This is suggested for further work.

The fatigue strength is highly influenced by the local temperature, and it is very important to know the temperature field of the piston in order to accurately investigate the possibility of fatigue.

The inner face of the pin boss has an interesting edge-effect, creating a circumferential tensile stress just at the edge of the face. This is most likely an edge-effect that was not noticed in earlier work due to higher constraints on mesh densities. While this is not the point of maximum circumferential stress around the boss, it is still a potential site for crack-initiation.

Both the boss and the bowl rim was well within the fatigue strength of the material at their respective locations, and it should be possible to increase the thermal loading on the piston, while maintaining a reasonable lifetime.

7 Further work

- **Investigating the heat transfer boundary conditions experimentally.** A lot of information that is needed to obtain the thermal boundary conditions of the engine is currently unknown, and the values used in this work are very crude. Doing a more thorough investigation of the piston assembly and the heat transfer in the engine would be very beneficial. This would include getting the dimensions for the cylinder liner and the temperatures of the oil sump and cooling water. Knowledge of the instantaneous gas temperature inside the combustion chamber would be ideal. Combined with simulations and empirical formulae this could be used to get a more accurate understanding of the thermal operating conditions of the piston.
- **Verifying the strength of the piston skirt.** The interaction between the piston skirt and cylinder liner due to lateral forces is something that could be investigated using FEA. Accurate data of the piston and cylinder profile and how they change shape during thermal loading would be necessary.
- **Performing a fatigue analysis for multiple load states.** Because the engine is intended to be supercharged, its thermal loading is intended to increase. Doing FEA for multiple load states and investigating the effects on the actual piston lifetime could be useful. This would require the thermal boundary conditions, as well as some software capable of generating SN-curves such as nCode DesignLife.

8 References

[1] *Petter PH range Workshop Manual.*

[2] J. Tingstad. Tilpasning av elektronisk innsprøytningssystem, type common rail, for en én-sylindret dieseldrevet laboratoriemotor.

[3] J. Fish and T. Belytschko. *A first course in finite elements.* Wiley, 2008.

[4] Mahle. *Cylinder components.* Springer, 2nd edition, 2016.

[5] Mahle. *Pistons and engine testing.* Springer, 2nd edition, 2016.

[6] K. Mollenhauer and H. Tschöke. *Handbook of Diesel engines.* Springer, 2010.

[7] R. Stone. *Introduction to internal combustion engines.* Palgrave Macmillan, 4th edition, 2012.

[8] M. J. Neale. *The Tribology Handbook.* Butterworth-Heinemann, 2nd edition, 1995.

[9] W. J. Griffiths and F. G. Cantow. Piston and ring technology for medium speed diesel and gas engines. *T&N symposium, Paper 23*, 1995.

[10] B. Challen and R. Baranescu. *Diesel engine reference book.* Butterworth-Heinemann, 2nd edition, 1999.

[11] *Abaqus 6.14 Documentation.*

[12] Dr.-Ing. Peter Reipert and Dr.-Ing. Horst Moebus. A contribution to the calculation of piston bosses. *75 Years Kolbenschmidt*, 1985.

[13] M. T. Abbes, P. Maspeyrot, A. Bounif, and J. Frene. A thermomechanical model of a direct injection diesel engine piston. *Proceedings of the Institution of Mechanical Engineers*, 218:395–409, 2004.

[14] Xiqun Lu, Quan Li, Wenping Zhang, Yibin Guo, Tao He, and Dequan Zou. Thermal analysis on piston of marine diesel engine. *Applied Thermal Engineering*, 50:168–176.

[15] E. Buyukkaya and M. Cerit. Thermal analysis of a ceramic coating diesel engine piston using 3-d finite element method. *Surface & Coatings Technology*, 202:398–402.

[16] R. L. Norton. *Machine design: An integrated approach.* Prentice-Hall, 2nd edition edition, 2000.

[17] Y.A. Cengel and A.J. Ghajar. *Heat and mass transfer: Fundamentals and applications.* McGraw-Hill, 5th edition, 2015.

[18] A. Torregrosa, P. Olmeda, B. Degraeuwe, and M. Reyes. A concise wall temperature model for di diesel engines. *Applied Thermal Engineering*, 26:1320–1327.

[19] E. Buyukkaya. Thermal analysis of functionally graded coating alsi alloy and steel pistons. *Surface & Coatings Technology*, 202:3856–3865.

[20] W.C. Young and R.G. Budynas. *Roark's formulas for stress and strain.* McGraw-Hill, Maidenhead, 2001.

[21] R.E. Peterson. *Stress concentration factors.* John Wiley & Sons, Inc. New York, 1974.

[22] ESDU Data Sheet 89048. *Elastic stress concentration factors, geometric discontinuities in rods and tubes of isotropic materials.* Engineering Science Data Unit, London, 1989.

[23] R.J. Grant, M.Lorenzo, and J.Smart. The effect of poisson's ratio on stress concentrations. *Journal of Strain Analysis*, 42:1–10, 2007.

[24] R.C. Hibbeler. *Mechanics of materials.* Prentice-Hall, 8th edition, 2011.

[25] L. Lundby. *Forbrenningsmotorer Bind I.* Universitetsforl., 3rd edition, 1979.

[26] M. Caldera, J. M. Massone, and R. A. Martínez.

[27] R.J. Grant and B.C.D. Flipo. Parametric study of the elastic stress distribution in pin-loaded lugs modelled in two and three dimensions and loaded in tension. *Journal of Strain Analysis*, 44:473–489.

[28] R.J. Grant and J. Smart. A parametric study of the elastic stress distribution in pin-loaded tubes. *Journal of Strain Analysis*, 32(3):213–228.

[29] Jaap Schijve. *Fatigue of Structures and Materials.* Springer, 2nd edition, 2009.

[30] F.S. Silva. Fatigue on engine pistons - a compendium of case studies. *Engineering Failure Analysis*, 13:480–492, 2006.

[31] D. Fletcher-Jones, W.J. Griffiths, and Dr.R.Munro. New piston features for truck, off-highway and industrial diesel engines. *AE Group Symposium, Paper 7*, 1982.

[32] Yaohui Lu, Xing Zhang, Penglin Xiang, and Dawei Dong. Analysis of thermal temperature fields and thermal stress under steady temperature field of diesel engine piston. *Applied Thermal Engineering*, 113:796–812.

[33] F. Szmytka, M. Salem, F. Rézaï-Aria, and A. Oudin. Thermal fatigue analysis of automotive diesel piston: Experimental procedure and numerical protocol. *International Journal of Fatigue*, 73:48–57.

List of Figures

A Material properties

M124		
Hardness HB10	20°C	90-130
Tensile strength R_m [MPa]	20°C	200-250
	150°C	180-200
	250°C	90-110
	350°C	35-55
Yield strength $R_{p0.2}$ [MPa]	20°C	190-230
	150°C	170-210
	250°C	70-100
	350°C	20-30
Elongation at fracture A_5 [%]	20°C	<1
	150°C	1
	250°C	3
	350°C	10
Fatigue strength	20°C	90-110
under reverse bending stress σ_{bw} [MPa]	150°C	75-85
	250°C	45-50
	350°C	20-25
Young's modulus [MPa]	20°C	80 000
	150°C	77 000
	250°C	72 000
	350°C	65 000
Thermal conductivity [W/m K]	20°C	145
	350°C	155
Thermal expansion [10^{-6} mm/mm K]	20-100°C	19.6
	20-200°C	20.6
	20-300°C	21.4
	20-400°C	22.1
Density [10^{-6} kg/mm^3]	20°C	2.68
Relative wear rate		1

Figure 76: Piston casting AlSi alloy M124.

16MnCr5	
Young's modulus [MPa]	210 000
Thermal expansion [$10^{-6}\mathrm{K}^{-1}$] 20-200°C	13.1
Thermal conductivity [W/m K]	36
Density [10^{-6} kg/mm^3]	7.84
Poisson ratio	0.27

Figure 77: Piston pin case hardened steel 16MnCr5.

B Drawings

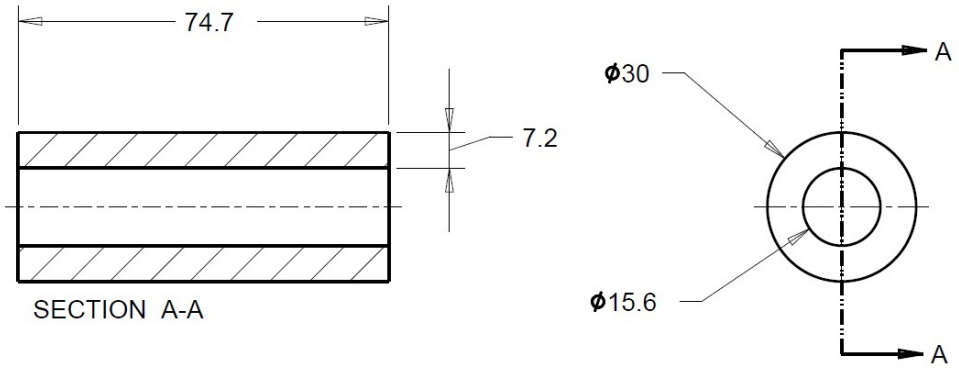

SCALE	TITLE
1.0	PETTER DIESEL PH1W PISTON PIN
YEAR	MATERIAL
2018	STEEL 16MnCr5 (ASSUMED)
DRAWING NO.	DRAWN BY
1/1	STEINAR HAUGLAND

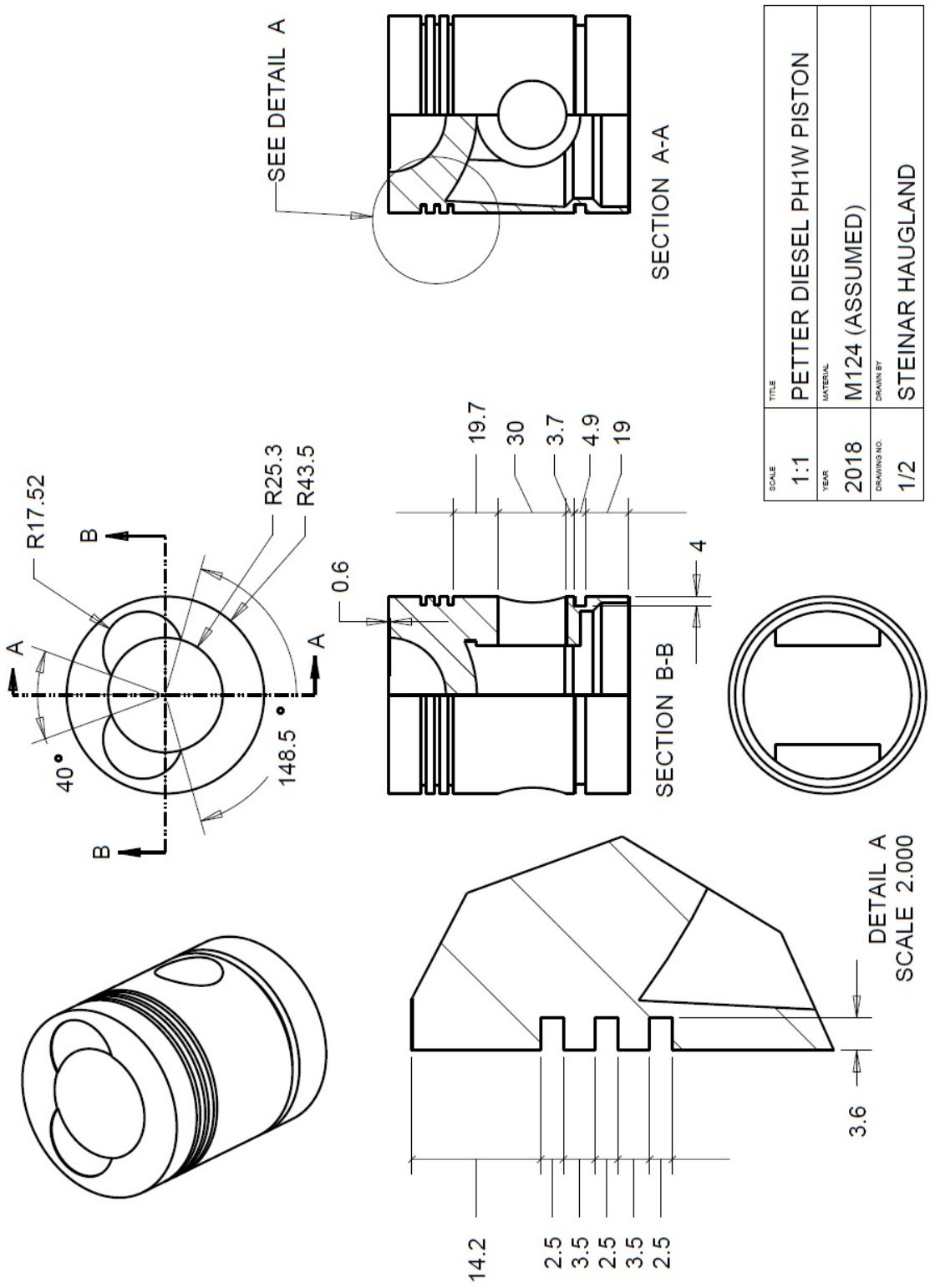
SEE DETAIL A
SECTION A-A
TITLE
PETTER DIESEL PH1W PISTON
SCALE
1:1
MATERIAL
M124 (ASSUMED)
YEAR
2018
DRAWN BY
STEINAR HAUGLAND
DRAWING NO.
1/2
R17.52
R25.3
R43.5
40°
148.5°
A
B
19.7
30
3.7
4.9
19
0.6
4
SECTION B-B
DETAIL A
SCALE 2.000
3.6
14.2
2.5
3.5
2.5
3.5
2.5

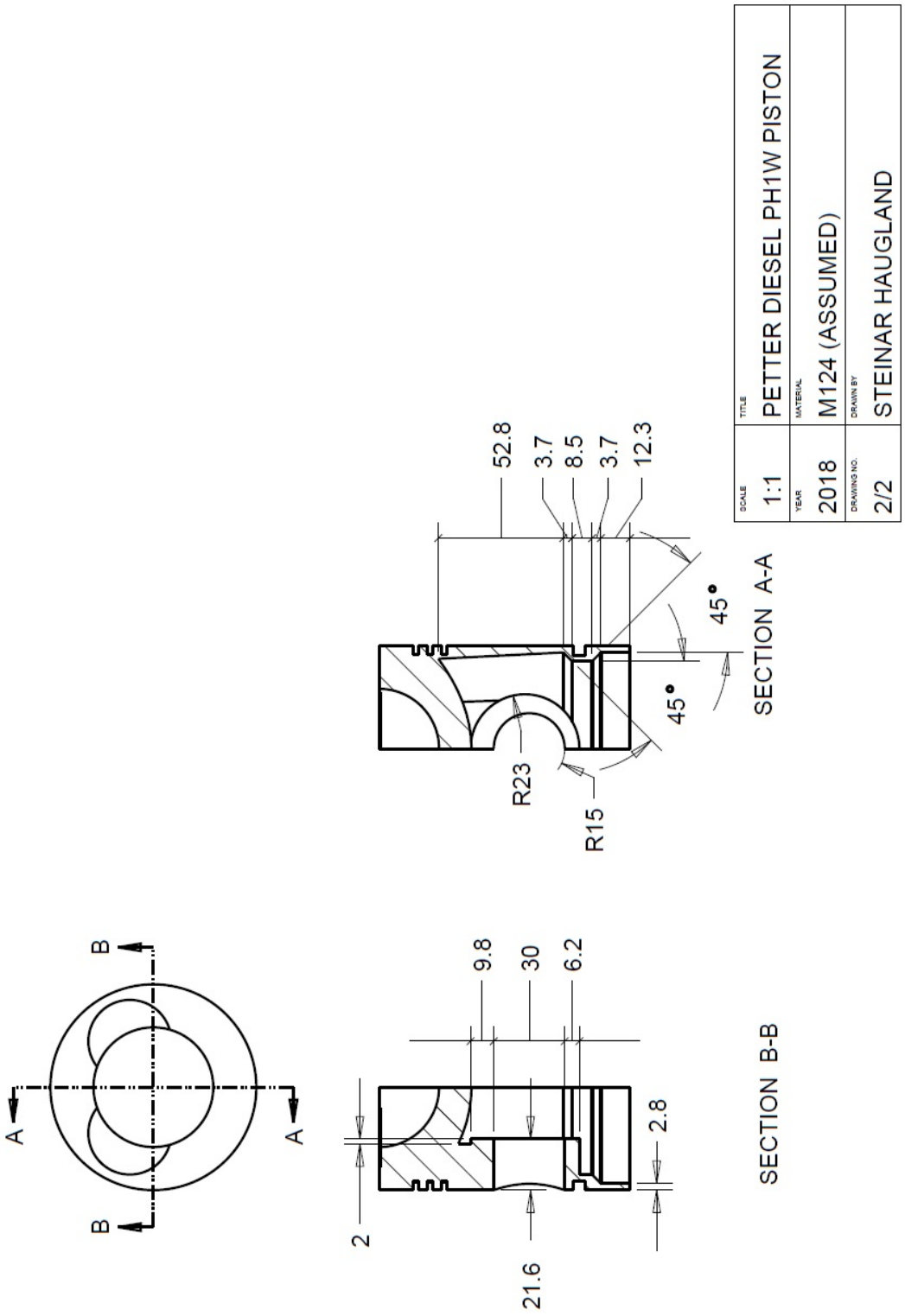
SCALE
1:1
TITLE
PETTER DIESEL PH1W PISTON
YEAR
2018
MATERIAL
M124 (ASSUMED)
DRAWING NO.
2/2
DRAWN BY
STEINAR HAUGLAND
52.8
3.7
8.5
3.7
12.3
45°
45°
R23
R15
SECTION A-A
A
A
B
B
9.8
30
6.2
2
2.8
21.6
SECTION B-B